Run-Around Energy Recovery System with a Porous Solid Desiccant

A Thesis

Submitted to the College of Graduate Studies and Research

in Partial Fulfillment of the Requirements for the Degree of

Master of Science

in the Department of Mechanical Engineering

University of Saskatchewan

Saskatoon, Saskatchewan

By

Meng Li

PERMISSION TO USE

I agree that the Libraries of the University of Saskatchewan may make this thesis freely available for inspection. I further agree that permission for copying of this thesis in any manner, in whole or in part, for scholarly purposes may be granted by my supervisors (Professor R. W. Besant and Professor C. J. Simonson) or, in their absence, by the Head of the Department of Mechanical Engineering, or the Dean of the College of Engineering. It is understood that any copying or publication or use of this thesis or parts thereof for financial gain shall not be allowed without my written permission. It is also understood that due recognition shall be given to me and to the University of Saskatchewan in any scholarly use which may be made of any material in my thesis.

Requests for permission to copy or to make other use of material in this thesis in whole or part should be addressed to:

Head of the Department of Mechanical Engineering

University of Saskatchewan

Saskatoon, Saskatchewan S7N 5A9

ABSTRACT

In this thesis, heat and moisture transfer between supply and exhaust air streams are investigated for a run-around system in which the coupling material is a desiccant coated solid that is transported between two exchangers. The finite volume method is used to solve the governing partial differential equations of the cross-flow heat exchangers in the supply and exhaust ducts. The outlet air properties are calculated for several inlet air operating conditions and desiccant properties. The accuracy of the heat transfer model is verified by comparing the simulations with well-known theoretical solutions for a single cross flow heat exchanger and a liquid coupled run-around system. The difference between the analytical predictions and the numerical model for sensible effectiveness for each exchanger and the run-around system were found to be less than 1% over a range of operating conditions. The model is also verified by modifying the boundary conditions to represent a counter flow energy wheel and comparing the calculated sensible, latent, and total effectiveness values with correlations in the literature.

Using the verified model for energy exchangers and the run-around energy recovery system, the sensible, latent and overall effectiveness are investigated in each exchanger and the run-around system during simultaneous heat and moisture transfer. The overall effectiveness of the run-around energy recovery system is dependent on the air flow rate, the solid desiccant flow rate, the desiccant properties, specific surface area, the size of each exchanger, and the inlet air operating conditions. The run-around system can achieve a high overall effectiveness when the flow rates and exchanger’s properties are

properly chosen. Comparisons between the solid desiccant and salt solution run-around system effectiveness (Fan, 2005 and Fan et al, 2006) shows they are in good agreement. In a sensitivity study, the thickness of desiccant on the fibre is investigated in the solid run-around system. It was found that good performance is obtained with very thin desiccant coatings (1 or 2 μm). During the practical use of this system, a desiccant coated fibre could be inserted into very porous balls or cages that protect the desiccant coated fiber from mechanical wear. The performance sensitivity for this kind of run-around system is demonstrated.

ACKNOWLEDGEMENTS

I extend my thanks and appreciation to Professor R.W. Besant and Professor C. J. Simonson. Thank you for your guidance and support throughout this research. I am also grateful to Dr. W. Shang for his advice during my research.

Financial assistance from NSERC and Venmar CES, Saskatoon is also acknowledged and appreciated.

DEDICATION

I dedicate this thesis to my wife, Liqun Lu. Thank you for your love and support throughout this work.

TABLE OF CONTENTS

LIST OF TABLES

LIST OF FIGURES

NOMENCLATURE

ACRONYMS

ARI	Air-conditioning and Refrigeration Institute
ASHRAE	American Society of Heating, Refrigerating and Air-Conditioning Engineers
HVAC	Heating, Ventilating and Air-Conditioning
IAQ	Indoor Air Quality
RH	Relative Humidity

ROMAN SYMBOLS

$A_1 \sim A_8$	Empirical constants
$B_1 \sim B_8$	Empirical constants
C	Heat capacity rate [W / K]
$C_8 \sim C_{13}$	Empirical constants
Cp	Specific heat capacity[$J /(kg \cdot K)$]
Cr	Heat capacity ratio
D	Diffusivity [m^2 / s]; outside diameter of the desiccant coated fibre[μm]
d	Ball diameter[mm]; diameter of glass fibre [μm]
D_h	Hydraulic diameter [m]
E	The node to the east of node P
e	The face between two control volumes expressed by node E and P
F	The strength of convection

f	Air volume fraction
G_g	Air mass flow velocity [$kg/(m^2 \cdot s)$]
h_{gsl}	Convective heat transfer coefficient [$W/(m^2 \cdot K)$]
h_m	Convective mass transfer coefficient [m/s]
h_{fg}	Heat of vaporization [J/kg]
H	Enthalpy [J/kg]
H^*	Operating condition factor
K	Thermal conductivity [$W/(m \cdot K)$]
m	The number of nodes in air flow direction
$\dot{m}$	Rate of phase change per unit volume [$kg/(m^3 \cdot s)$]
N	The numerical node above or north of node P
n	The face between two control volumes expressed by node N and P; the number of nodes in solid flow direction
Ntu	Number of transfer units
Nu	Nusselt number
p	Partial pressure [Pa]
P	Total pressure [Pa]; the numerical node which is studied
ΔP	Pressure difference across the exchanger [Pa]
Pe	Peclet number
Pr	Prandtl number
Q	Volume flow rate of air [m^3/s]
q	Heat transfer rate [W]
Re	Reynolds number
R_T	The residuals of the governing equations
S	The numerical node below or south of node P
s	The face between two control volumes expressed by node S and P
S_c	Schmidt number
S_h	Sherwood number
S_v	Volume specific surface area of the bed [m^2/m^3]

T	Temperature [K]; [$^{\circ}C$]
t	Time [s]
Δt	Time interval [s]
U	Water content per unit dry desiccant [*kg(water)/kg(dry desiccant)*]
u	Velocity [*m/s*]
V	Volume [m^3]
W	Humidity ratio [*kg(water)/kg(dry air)*]; The node to the west of node P
Wm	Empirical coefficient used in the sorption isotherm to describe the maximum moisture capacity [kg(water)/kg(dry desiccant)]
w	The face between two control volume expressed by node W and P
x	Coordinate [m]
y	Coordinate [m]
x_0	Length of the bed [m]
y_0	Width of the bed [m]
z_0	Depth of the bed [m]
X^*	Dimensionless coordinate x / x_0
Y^*	Dimensionless coordinate y / y_0
Δx	Length of the differential control volume [m]
Δy	Width of the differential control volume [m]

GREEK SYMBOLS

Γ	General diffusion coefficient
ε	Effectiveness; porosity of the bed
ε_g	Volume fraction of gas
ε_l	Volume fraction of adsorbed water; latent effectiveness
ε_s	Volume fraction of solid; sensible effectiveness
ε_t	Total effectiveness

θ	Dimensionless temperature difference
μ	Air dynamic viscosity [$kg/(m \cdot s)$]
ν	Air kinematic viscosity [m^2/s]
ρ	Density [kg/m^3]
τ	Tortuosity
Φ	Dependent variable in the numerical analysis
ϕ	Relative humidity of the gas at certain point in the bed
ϕ_{sur}	Relative humidity on the desiccant surface

SUBSCRIPTS

air	Dry air
E	Exhaust side
eff	Effective properties
f	Fibre glass
g	Gas including dry air and water vapour
i	Column number of node position; ball's position in air flow direction
in	Inlet; ball inside flow
j	Row number of node position; ball's position in solid flow direction
l	Adsorbed water
o	Overall value for the run-around system
m	Dimensionless mass flow rate for energy wheel
mt	Dimensionless moisture transfer group for energy wheel
out	Bulk mean outlet conditions; ball outside flow
S	Supply side
s	Solid including fibre and silica gel
si	Silica gel
sl	Mixture of solid and adsorbed water
sur	Solid surface
v	Water vapour

Chapter 1

INTRODUCTION

1.1 Introduction

People in air conditioned rooms will be dissatisfied if there is not enough fresh air supply or the fresh air is not conditioned to meet comfort conditions in the space. The ASHRAE standard for the outside fresh air ventilation rate in a building specifies the outdoor ventilation rates required for good indoor air quality (IAQ) in occupied rooms. Typically, the higher the ventilation rate, the better the IAQ. However, as the air ventilation rate increases, the heating and cooling loads also increase. This means that the HVAC system will need more energy to maintain comfortable conditions in the building. The capacity of the HVAC equipment including boilers, chillers, and pumps needs to be enlarged to satisfy the increased load, and at the same time, the size of the pipes and valves, and amount of insulation material needs to increase. The total investment for the HVAC system will be increased, and the operating cost will be higher than that of a low ventilation rate system.

In order to save energy and improve IAQ for building occupants, HVAC engineers have used several types of heat and moisture recovery devices in their designs. Sensible heat transfer is caused by a temperature difference, and latent heat transfer is caused by a

humidity difference. The devices for only sensible heat transfer are heat pipes, air-to-air cross-flow plate (e.g., metal or plastic) heat exchangers, and run-around heat recovery systems using a coupling fluid (ASHRAE, 2004). The devices which can recover heat and moisture are energy wheels and air-to-air cross-flow membrane (e.g., vapour permeable membranes or paper) energy exchangers. Energy wheels and cross-flow plate enthalpy exchangers can transfer heat and moisture between the supply and exhaust air streams.

All energy exchangers reduce the energy use and required capacity of the HVAC system, but they have different disadvantages. Heat pipes and air-to-air cross-flow plate heat exchangers only transfer sensible heat and do not transfer moisture. In addition, the supply and exhaust ducts must be side-by-side, and as a result, the fresh air may be contaminated by the exhaust air. Although the run-around heat recovery system does not need the supply duct and exhaust duct to be installed side-by-side, it does not usually have moisture transfer.

The energy wheel and air-to-air cross-flow membrane energy exchangers transfer moisture, but the supply and exhaust ducts must be in the same location. As a result, their use in retrofit applications is limited and the fresh air entering the building space may be contaminated by the exhaust air. Fan (2005) and Fan et al. (2006) simulated a run-around heat and moisture recovery system. An aqueous desiccant salt solution was used in this system to permit heat and moisture transfer between two cross-flow semi-permeable plate exchangers. With this system, the supply and exhaust ducts are not required to be at the same location. Although a run-around energy recovery system using

a liquid desiccant is promising, and has many practical advantages, it may be possible to also use a solid desiccant to transfer heat and moisture in a run-around system. There has been no research on a run-around system using a solid desiccant to transfer heat and moisture between separated air streams, so such a system will be the focus of the thesis.

The proposed run-around system using a porous solid desiccant ball bed provides heat and moisture transfer between the supply air stream and exhaust air stream, and the air ducts can be in different locations to reduce the possibility of cross contamination. This energy recovery system is shown in Figure 1.1 and features the flow of a bed of porous balls and air through the exchangers. Heat and moisture are exchanged between the air streams and the porous balls in each exchanger. In this closed loop system, the solid particles which exit the exhaust air exchanger are conveyed to the inlet of the supply air exchanger. Similarly the outlet particles that flow from the supply exchanger are conveyed to the inlet of the exhaust air exchanger. It is not the purpose of this research to design this conveyor system; rather, it is assumed that this conveyor system exists and is adiabatic and impervious to water vapour transfer. It is not necessary to worry about the water solution leakage as in the liquid system. The solid balls move slowly so that maintenance personnel can change damaged balls even when the system is operating.

The purpose for this research is to develop a numerical model for this new device, to validate it and verify its accuracy using information from the literature and sensitivity studies. It is especially important to validate the accuracy of the moisture transfer model, which will be done by comparing the numerical results from a liquid run-around energy

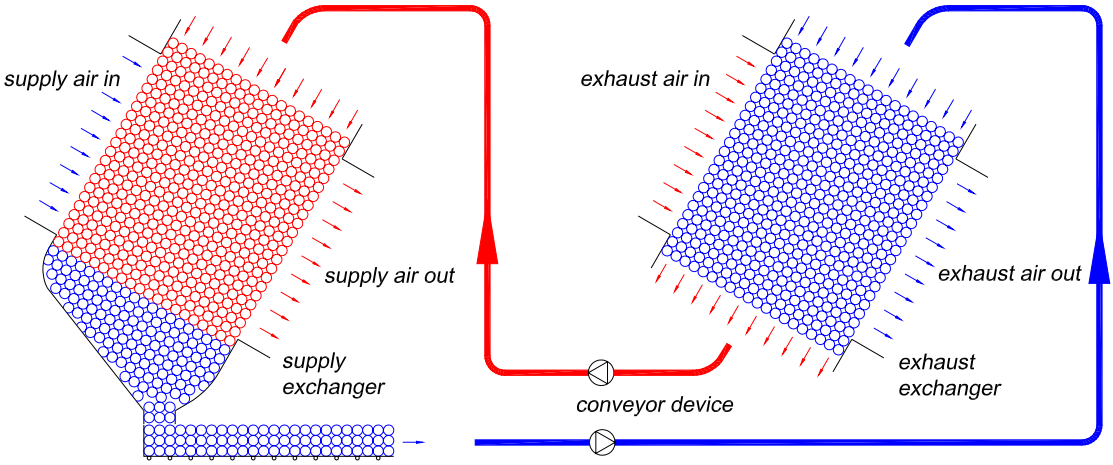

Figure 1.1 The run-around system with porous balls filled with desiccant coated fiber glass moving between supply and exhaust exchangers.

system Fan (2005) and effectiveness correlations for energy wheels (Simonson & Besant, 1999). The model can then be applied to determine the effectiveness of the run-around system for different climate conditions, air flow rates, exchanger sizes, and fractions of silica gel inside the ball.

1.2 Literature Review

Many research papers have been published on topics related to this thesis: single flat-plate heat exchangers, sensible heat transfer run-around systems, enthalpy transfer run-around systems with liquid desiccant solution, energy wheels, convection coefficients and air pressure drop through porous media. The section provides a brief review of these topics.

1.2.1 Single Flat-plate Heat Exchanger

Mason (1955) obtained the analytical solution for a cross-flow plate heat exchanger by using Laplace transforms. The effectiveness correlation for a cross-flow plate heat exchangers is presented in Kays and London (1984).

1.2.2 Single Flat-plate Heat and Moisture Exchanger

Enthalpy exchangers can transfer sensible heat and moisture between the supply and exhaust air streams through water vapor permeable membranes. Niu and Zhang (2001) developed a mathematical model for a cross-flow air-to-air enthalpy exchanger with hydrophilic membrane cores, and solved the equations by using a finite volume method. The sensible, latent, and total effectiveness were presented for different operating conditions, and different vapor permeability of the membrane.

1.2.3 Run-around Heat Exchanger

The run-around heat recovery system, using coupled liquid flowing between the supply and exhaust exchangers, is very reliable and flexible in application. Kays and London

(1951) found that the peak sensible effectiveness for the run-around system can be obtained when the heat capacity rate of air is same as that of the coupling liquid.

Forsyth and Besant (1988a, 1988b) used a numerical optimization technique to analyze the design of a run-around heat transfer system with two coils. The simulated results were very similar to the measured data. Based on the research of Forsyth and Besant, Zeng et al. (1992) found that the temperature dependent properties of aqueous glycol should be included in the system analysis when the temperature difference between the supply and exhaust inlet is large, and the Reynolds number is low.

1.2.4 Air Flow through Silica Gel Bed

Sun (2003) developed a one-dimensional theoretical/numerical model to simulate the process of heat and moisture adsorption during transient flow of humid air passing through a silica gel particle bed. The numerical results were compared with the experiment data by measuring the air outlet temperature, relative humidity and moisture accumulation inside the silica gel bed. The results showed that silica gel has a very high moisture adsorption capacity, and a large amount of heat is released during the moisture adsorption.

1.2.5 Energy Wheels

Simonson and Besant (1998) developed a numerical model for simulating the sensible, latent, and total effectivenesses of energy wheels. It was found that the effectiveness is strongly dependent on the operating temperature and relative humidity, and accurate effectiveness correlations were developed for an energy wheel operating under different operating conditions. The effectiveness correlations were based on over 600 simulation data points and have an uncertainty of less than 2.5%. It was observed that even though the wheel matrix is cooler than the air, the air temperature can increase as it flows through the wheel if the phase energy released due to moisture accumulation in the matrix is larger than the heat transferred from the air to the matrix by convection.

1.2.6 Run-around System with Liquid Desiccant Solution

Fan (2005) and Fan et al. (2006) studied a run-around heat and moisture recovery system comprised of two liquid-to-air heat and moisture exchangers. The coupling fluid was a liquid desiccant (e.g. aqueous LiBr or LiCl solutions) and can transfer heat and moisture between the supply and exhaust exchangers. The liquid circulating pump can adjust the flow rate of the salt solution to control the heat and moisture transfer rate. The numerical model for a run-around system with two sensible heat exchangers was developed, and validated by using data from the published literature. Based on this, a numerical model of the run-around heat and moisture recovery system was developed using only basic physical and chemical principles, component properties and operating conditions. The

results show that, for a specific Ntu, the maximum effectiveness occurs at a heat capacity ratio equal to 1 for the sensible run-around heat recovery system, and at heat capacity ratio of 3 ($C_{sol} / C_g = 3$) for the heat and moisture run-around system operating at ARI summer and winter operating conditions (ARI, 2005). It was also found that the peak effectiveness increases with Ntu.

1.2.7 Pressure Drop through Porous Media

Dullien (1992) showed that the pressure drop in a fibrous bed can be calculated as a function of the flow rate by using the Ergun (1952) equation, when the flow rates are outside the range of validity of Darcy's law, i.e. Re larges than 10. The Ergun equation is suitable to calculate the air pressure drop through a porous bed with relative uniform porosity, but the pressure drop through moving porous balls cannot be used due to the empty space between the balls.

1.3 Objectives

The overall goal of this research is to develop and verify a numerical model of a run-around energy recovery system using cross-flow exchangers with solid desiccant particles as the thermal energy and moisture run-around component, and then use the model to study a new device in an HVAC application. The goal is to determine the

properties of the run-around system (e.g. exchanger size and thickness of the desiccant coating) that will ensure that the system has a good performance in application.

The specific objectives are as follows:

1. Develop a numerical model to simulate a run-around heat and moisture transfer system, which includes supply air stream, exhaust air stream, and the moving porous desiccant coated solid between the two exchangers.

2. Validate the model with well-known theoretical solutions for a single cross flow heat exchanger, a run-around heat transfer system, and an energy wheel with heat and moisture transfer.

3. Find the thermal transfer properties and characteristics to achieve a high overall effectiveness for a single heat exchanger and run-around heat transfer system.

4. Find the thermal and moisture transfer properties and characteristics to achieve a high overall effectiveness for a run-around heat and moisture transfer system under ARI summer and winter operating conditions (ARI, 2005). Compare the results from the simulation with those from a salt solution run-around system (Fan, 2005) to further validate the accuracy of the model.

5. Determine the optimum operating conditions for maximum energy savings for different solid desiccant properties and investigate various desiccant thicknesses to get the coating information for future manufacturing.

1.4 Thesis Overview

A numerical model of heat and moisture transfer exchangers coupled in a run-around system is developed in Chapter 2. The governing equations are formulated based on energy and mass conservation and discretized using the finite volume method. The sensible, latent and total effectivenesses of a single exchanger and a run-around system are defined in this chapter.

The model is verified by comparing it with well-known theoretical solutions in Chapter 3. These comparisons include: a single exchanger with heat transfer only, a run-around system with heat transfer only, and an energy wheel.

The simulated results from the numerical model are presented in Chapter 4. The results for a run-around system with heat transfer only are illustrated first, then a single exchanger with heat and moisture transfer, and finally the run-around exchanger with heat and moisture transfer including a sensitivity study on the thickness of desiccant coating.

In Chapter 5, a numerical sensitivity study is performed by varying key parameters, such as Ntu, air velocity, silica gel fraction, and other variable for a moving porous ball system.

Chapter 6 provides a summary and the conclusions from this research, as well as the recommended future work.

Chapter 2

NUMERICAL MODEL

2.1 Introduction

In this chapter, the numerical model for the run-around system with two heat and moisture exchangers is developed. Governing equations, boundary conditions and operating conditions are established to describe this two-dimensional problem. The finite volume method is used to discretize the governing partial differential equations.

2.2 Flow and Exchanger Configuration

The exchangers shown in Figure 2.1 feature the flow of a porous bed across the exchangers which are arranged in cross-flow. The system has an operating configuration as shown in Figure 1.1, except the porous media is distributed uniformly inside the whole porous bed rather than only inside balls.

2.2.1 Structure of Each Exchanger

The particle bed, which is a porous material coated with a desiccant, is assumed to move

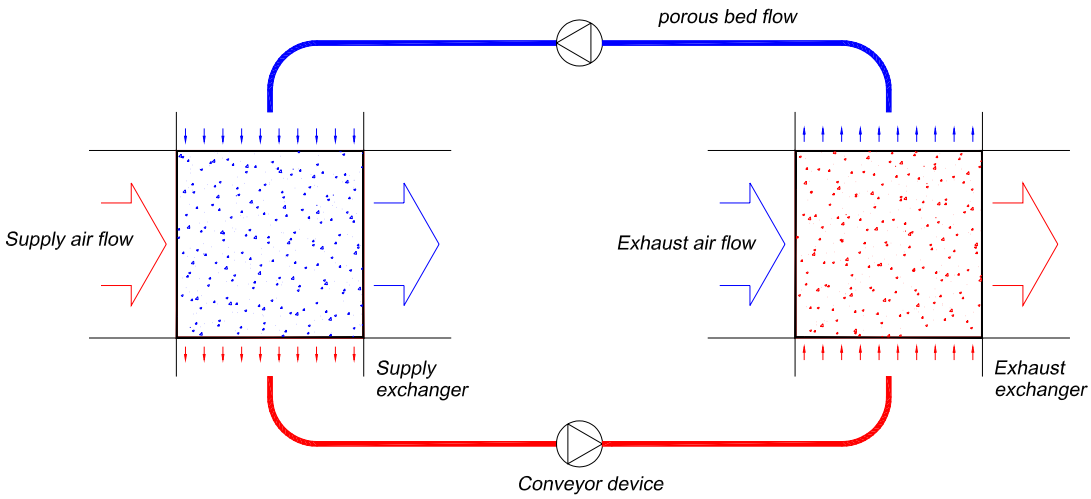

Figure 2.1 Schematic diagram of a run-around energy recovery system with solid desiccant as the coupling medium.

with a uniform and constant velocity through each exchanger. The material in the moving bed could be a very porous fibre glass coated with a desiccant coating as shown in Figure 2.2. With hot and humid supply air conditions, the desiccant coated fibres gain heat and moisture from the supply air in the supply exchanger so that the supply air is cooled and dehumidified. The porous material leaving the supply exchanger is mechanically conveyed to the exhaust exchanger where it is regenerated by the exhaust air flow.

2.2.2 Silica Gel Properties

The desiccant material could be silica gel or any material with a high affinity for water.

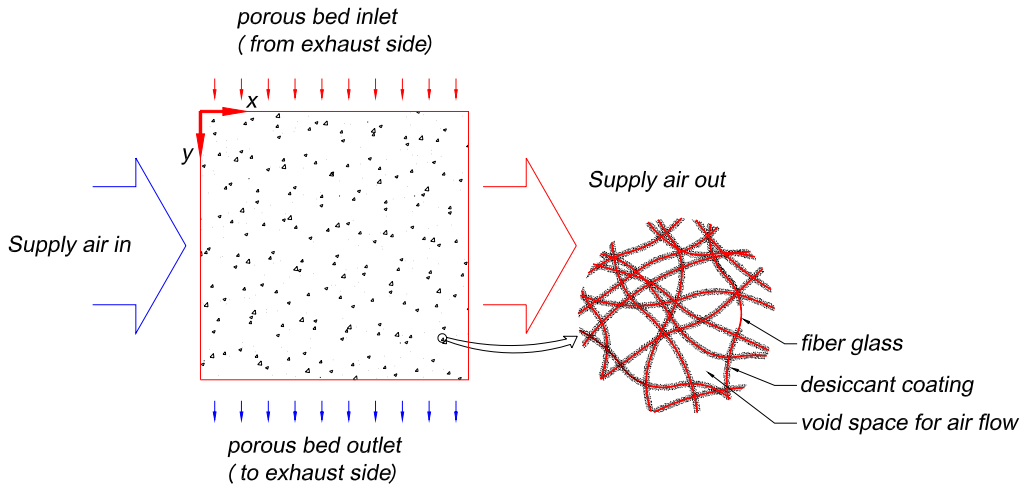

Figure 2.2 Schematic diagram of air-to-solid desiccant cross flow heat exchanger.

Silica gel has a solid structure with an average specific pore volume of about 0.82 cm^3/g (Sun, 2003). It is composed of silicon dioxide (SiO_2) and has a high internal surface area, up to 800 m^2/g, giving it a high moisture adsorption capacity. However, the internal surface area may not be available for sorption processes in exchangers that rapidly switch the desiccant between the supply side and exhaust side because the water vapour diffuses very slowly inside particle. During the moisture adsorption process, latent heat is released; and during the desorption process, energy is required to desorb the adsorbed water.

Sun et al. (2005) measured the equilibrium sorption isotherm of silica gel. A correlation for equilibrium relative humidity (ϕ) based on the moisture content of the dry desiccant (U) was developed as follows:

$$\phi = A_1 + A_2 U + A_3 U^2 + A_4 U^3 + A_5 U^4 + A_6 U^5 + A_7 U^6 + A_8 U^7 \quad (2.1)$$

where, A_1=-0.0040791013

A_2=5.7635539

A_3=-12.934021

A_4=66.765676

A_5=-512.87559

A_6=815.04053

A_7=842.23156

A_8=495.99532

In the latent effectiveness calculations, another correlation for equilibrium moisture content based on relative humidity is obtained by inverting equation (2.1):

$$U = B_1 + B_2 \phi + B_3 \phi^2 + B_4 \phi^3 + B_5 \phi^4 + B_6 \phi^5 + B_7 \phi^6 + B_8 \phi^7 \quad (2.2)$$

where, B_1=5.0984329e-5

B_2=0.24823428

B_3=-1.2483947

B_4=11.414806

B_5=-48.148515

B_6=97.758549

B_7=-90.571667

B_8=30.869368

2.3 Governing Equations

In the moving bed exchanger, there is heat and moisture transfer between the solid and air and it is assumed that the adsorbed water has the same temperature as the solid (local thermal equilibrium). The local volume averaging technique is used to establish the basic governing equation for conservation of energy and mass. For the differential control volume, there are two energy conservation equations: one for the air component, and another for the solid and adsorbed water component. There are also two mass conservation equations: one for vapour transfer, and another for water continuity on the surface of the desiccant. The resulting governing equations for heat and moisture transfer are based on the assumption that the porous bed is homogeneous and isotropic (Kaviany, 1991). The major assumptions are:

1. the energy released during adsorption is delivered to the solid phase and the energy required for desorption comes from the solid phase;
2. thermal and mass dispersion in the porous medium are negligible;
3. hysteresis in the sorption isotherm and the heats of sorption for the desiccant coating are assumed negligible;
4. the transport of the moisture within the desiccant due to capillary motion is negligible;
5. the desiccant coated fibre forms a rigid porous medium with constant porosity and specific surface area for heat and moisture transfer between the air and the moving porous bed;

6. the porous media is homogeneous with properties that may be assumed to be constant for individual phases (except for gaseous densities);
7. the gas phase is assumed to be an ideal gas mixture;
8. the pressure drop across the exchanger does not result in a significant change in the absolute pressure or air density; and
9. the inlet conditions of the air and the porous bed are uniform unless otherwise specified.

2.3.1 Equations

For air flow in the x direction and particle flow in the y direction, the energy equation for air flow is:

$$\frac{\partial}{\partial t}\left(\varepsilon_g \rho_g Cp_g T_g\right)+\frac{\partial}{\partial x}\left(\rho_g u_g Cp_g T_g\right)=\frac{\partial}{\partial x}\left(\varepsilon_g K_g \frac{\partial T_g}{\partial x}\right) + \frac{\partial}{\partial y}\left(\varepsilon_g K_g \frac{\partial T_g}{\partial y}\right)-h_{gsl} S_v\left(T_g - T_{sl}\right) \tag{2.3}$$

where subscript g refers to the gas phase properties and subscript sl refers to the properties of the solid + absorbed phase. The symbols for this equation and those that follow are defined in the nomenclature.

For solid particle and liquid (adsorbed phase of water), the energy equation is:

$$\frac{\partial}{\partial t}\left(\left(1-\varepsilon_g\right)\rho_{sl}Cp_{sl}T_{sl}\right)+\frac{\partial}{\partial y}\left(\left(1-\varepsilon_g\right)\rho_{sl}u_{sl}Cp_{sl}T_{sl}\right)=$$
$$\frac{\partial}{\partial x}\left(\left(1-\varepsilon_g\right)K_{sl,eff}\frac{\partial T_{sl}}{\partial x}\right)+\frac{\partial}{\partial y}\left(\left(1-\varepsilon_g\right)K_{sl,eff}\frac{\partial T_{sl}}{\partial y}\right) \tag{2.4}$$
$$+h_{gsl}S_v\left(T_g-T_{sl}\right)-\dot{m}h_{fg}-\dot{m}Cp_v\left(T_g-T_{sl}\right)$$

where it is assumed that the phase change energy is delivered to or obtained from the solid phase rather than the gas phase (Simonson and Besant, 1997).

The mass transfer equation for the water vapour flow is:

$$\frac{\partial\left(\varepsilon_g\rho_v\right)}{\partial t}+\frac{\partial}{\partial x}\left(\rho_v u_g\right)=\frac{\partial}{\partial x}\left(D_{v,eff}\frac{\partial\rho_v}{\partial x}\right)+\frac{\partial}{\partial y}\left(D_{v,eff}\frac{\partial\rho_v}{\partial y}\right)+\dot{m} \tag{2.5}$$

where,

$$D_{v,eff}=\frac{\varepsilon_g D_v}{\tau} \tag{2.6}$$

The liquid phase continuity equation for adsorbed water on the desiccant coating is:

$$\rho_l\frac{\partial\varepsilon_l}{\partial t}+\rho_l u_{sl}\frac{\partial\varepsilon_l}{\partial y}+\dot{m}=0 \tag{2.7}$$

The volumetric continuity equation is:

$$\varepsilon_s+\varepsilon_l+\varepsilon_g=1 \tag{2.8}$$

2.3.2 Convective Heat Transfer Coefficient

The convective heat transfer coefficient (h_{gsl}) between the flowing air and the fibre surface is an important parameter that must be known to calculate the effectiveness of the exchanger. Travkin et al. (2001) compared the dimensionless heat transfer coefficients (Nusselt Number (Nu)) for flow in porous media from different research studies and found that there was reasonable agreement between the correlations by Kays and London (1984), Achenbach (1995), and Kokorev et al. (1987). The result from Gortyshov et al. (1987) shows that Nu for flow through a high porosity medium is about half of that from Kays and London (1984). In this simulation, the correlation for Nu from Gortyshov et al. (1987) is used, because it gives a more conservative estimate. The relationship of Gortyshov et al. (1987) is:

$$Nu = 0.7\,\mathrm{Re}^{0.55}\,\mathrm{Pr}^{1/3} \tag{2.9}$$

$$h_{gsl} = \frac{NuK_{air}}{D_h} \tag{2.10}$$

$$\mathrm{Re} = \frac{D_h G_g}{\mu} \tag{2.11}$$

$$D_h = \frac{4\varepsilon_g}{S_v} \tag{2.12}$$

$$\mathrm{Pr} = \frac{\mu Cp_g}{k_g} \tag{2.13}$$

$$G_g = \frac{\rho_g u_g}{\varepsilon_g} \tag{2.14}$$

where, h_{gsl} is convection coefficient between the air and the solid; G_g is the mass velocity; Re is the Reynolds number for air in the bed; and D_h is the hydraulic diameter of the bed. Other symbols are defined in the nomenclature.

2.3.3 Phase Change Rate

The phase change rate, $\dot{m}$, is the key parameter that gives the moisture transfer flux of the exchangers. It is defined as:

$$\dot{m} = -h_m S_v \left(\rho_v - \rho_{v,sur}\right) \tag{2.15}$$

where h_m is the mass transfer coefficient between the air and the surface of the desiccant coating; S_v is specific surface area; ρ_v is water vapour density in the air flow; and $\rho_{v,sur}$ is the water vapour density on the desiccant surface.

The convection mass transfer coefficients are obtained using the analogy between the heat and mass transfer, so that

$$\frac{Sh}{Sc^n} = \frac{Nu}{\mathrm{Pr}^n} \tag{2.16}$$

where n = 1/3 from equation (2.9). The mass transfer coefficient is calculated using

$$h_m = \frac{ShD_v}{D_h} \tag{2.17}$$

and the Schmidt number is defined as

$$Sc = \frac{\mu}{\rho_g D_v} \tag{2.18}$$

2.3.4 Thermodynamic and Material Properties

The other equations needed in the model to describe the thermodynamic and material properties are listed below. The relative humidity is defined by:

$$\phi = \frac{P_v}{P_{sat}} = \frac{\rho_v R_v T}{f(T)} \tag{2.19}$$

where the saturation pressure of air is a function of temperature (ASHRAE 2005).

$$P_{sat} = \exp(C_8 / T + C_9 + C_{10}T + C_{11}T^2 + C_{12}T^3 + C_{13}\ln T) \tag{2.20}$$

where: P_v = partial pressure of water vapour (Pa)

P_{sat} = saturation pressure of water vapour (Pa)

T = absolute temperature (K)

C_8 = -5.8002006e+03

C_9 = 1.3914993

C_{10} = -4.8640239e-02

C_{11} = 401764768e-05

C_{12} = -1.4452093e-08

C_{13} = 6.5459673

The total air pressure is the sum of the partial pressures.

$$P = P_v + P_a \tag{2.21}$$

where,

$$P_v = \rho_v R_v T \tag{2.22}$$

$$P_a = \rho_a R_a T \tag{2.23}$$

The thermal conductivity of moist air is given by

$$K_g = \frac{\rho_v K_v + \rho_a K_a}{\rho_v + \rho_a} \tag{2.24}$$

The density of the solid components are evaluated using the volume fraction of the dry solid (ε_s) and the adsorbed water (ε_l). Similarly, the specific heat and thermal conductivity of the solid components, including the adsorbed water, are evaluated as follows:

$$\rho_{sl} = \frac{\varepsilon_s \rho_s + \varepsilon_l \rho_l}{\varepsilon_s + \varepsilon_l} \tag{2.25}$$

$$Cp_{sl} = \frac{\varepsilon_s Cp_s \rho_s + \varepsilon_l Cp_l \rho_l}{\rho_{sl}(\varepsilon_s + \varepsilon_l)} \tag{2.26}$$

$$K_{sl,eff} = \frac{\varepsilon_s K_s + \varepsilon_l K_l}{\varepsilon_s + \varepsilon_l} \tag{2.27}$$

2.3.5 Boundary Conditions

The boundary conditions are given for the temperature and humidity of the air and porous material at the entrance of the supply (S) and exhaust (E) exchangers in Figure 2.1 at x = 0 and y = 0 respectively as in Figure 2.2. The boundary conditions correspond to ARI standard 1060 summer testing condition (ARI, 2005):

At x = 0, $T_{air,inS} = 308\,\text{K}$ (34.85 °C)

$T_{air,inE} = 297\,\text{K}$ (23.85 °C)

$\phi_{air,inS} = 47.4\%$

$\phi_{air,inE} = 51.2\%$

When the two exchangers are coupled with a moving desiccant in a run-around system, it is assumed that bulk temperature and moisture content of the desiccant coated fibres entering one exchanger (y = 0) are uniform and equal to the bulk temperature and moisture content at the outlet of the other exchanger. Therefore, it is assumed that the temperature and moisture content in the porous material becomes uniform due to conduction, diffusion and mechanical mixing prior to entering another exchanger. The

boundary condition equations for the solid components used in the run-around system between the supply and exhaust air exchangers are:

$$T_{sl,inS} = T_{sl,outE}$$

$$T_{sl,inE} = T_{sl,outS}$$

$$U_{sl,inS} = U_{sl,outE}$$

$$U_{sl,inE} = U_{sl,outS}$$

where the subscript out refers to the bulk mean outlet conditions as defined later in this thesis (see equation (2.44) and (2.45)).

2.3.6 Discretization of the Equations

The finite volume method (Patankar, 1980) is used to discretize the coupled partial differential equations for each exchanger. A numerical grid is used to discretize the bed inside each exchanger into a set of differential control volumes. The node distribution for the key nodes in one exchanger is shown in Figure 2.3. A FORTRAN code was developed to solve the discretizated governing equations for heat and moisture transfer in a single exchanger and the run-around system.

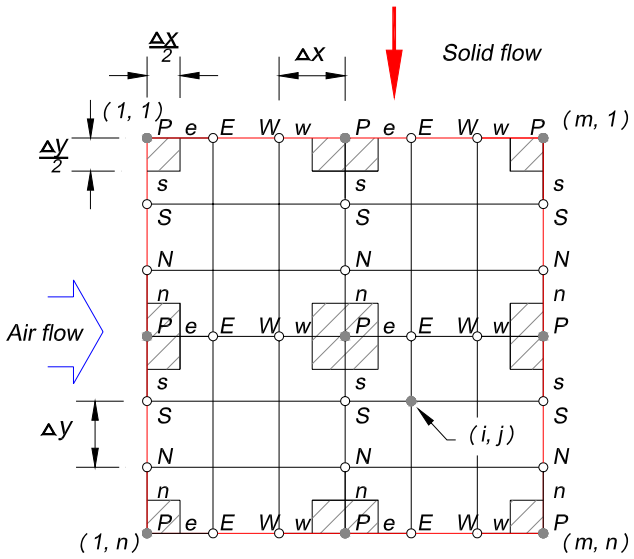

Figure 2.3 Node distribution showing the typical nodes at "P" inside a porous bed and on the boundary of a porous bed exchanger.

The Peclet number, Pe, is used to determine if an upwind or central difference method should be used to discretize the advection terms in the governing equations, where Pe is the ratio of heat (or moisture) advection to heat (or moisture) diffusion.

$$Pe = \frac{F}{D} = \frac{\rho \cdot u_g \cdot L}{\Gamma} \tag{2.28}$$

where:

F = the strength of convection

D = the diffusion conductance

Γ = the general diffusion coefficient

Since the Peclet numbers for both heat and moisture transfer are greater than 2, the upwind method is used. The grid size within the porous bed is $\Delta x = \Delta y = 6\,\text{mm}$, and the grid size in the four corners is $\Delta x/2$ and $\Delta y/2$. This gives a total number of nodes in air

flow direction of m = 51, and in solid flow direction of n = 51. Numerical simulations were performed to ensure that the results are not grid sensitive. The numerical solution is time accurate and thus each dependent variable, Φ, is required to satisfy equation (2.29) in the numerical analysis before time is advanced.

$$\frac{\sum_{(1,1)}^{(m,n)}\left|\Phi_{(i,j)}^{k}-\Phi_{(i,j)}^{k-1}\right|}{mn\left(\Phi_{\max}-\Phi_{\min}\right)}\le\varepsilon_c=\text{1e-4} \tag{2.29}$$

The residuals of the governing equations are required to satisfy

$$R_T=\left(\frac{1}{mn}\sum_{(1,1)}^{(m,n)}\left(R_{(i,j)}\right)^2\right)^{\frac{1}{2}}\le\varepsilon_R=\text{1e-4} \tag{2.30}$$

When the system reaches steady state, the heat and moisture transfer rates in the supply exchanger will equal the heat and moisture transfer rates in the exhaust exchanger. The energy and mass transfer rates satisfy

$$\frac{q_S-q_E}{\left(q_S+q_E\right)/2}\le 0.01 \tag{2.31}$$

$$\frac{\dot{m}_S-\dot{m}_E}{\left(\dot{m}_S+\dot{m}_E\right)/2}\le 0.01 \tag{2.32}$$

2.4 Exchanger Effectiveness

The effectiveness of a heat exchanger, including a run-around system, is expressed as (Kays and London, 1984):

$$\varepsilon = \frac{Actual\ heat\ transfer\ rate}{Maximum\ possible\ heat\ transfer\ rate\ of\ an\ exchanger\ with\ an\ in finite\ heat\ transfer\ area\ and\ the\ same\ operating\ conditions} \quad (2.33)$$

The effectiveness is a function of the number of transfer units (Ntu) and heat capacity ratio (Cr).

2.4.1 Sensible Effectiveness

Using the definition in equation (2.33), the sensible effectiveness for the single exchanger is defined as:

$$\varepsilon_s = \frac{C_{g,in}T_{g,in} - C_{g,out}T_{g,out}}{C_{\min}(T_{g,in} - T_{sl,in})} \quad (2.34)$$

where the heat capacity rate of the gas phase is

$$C_g = \dot{m}_{air}(Cp_{air} + W_g Cp_v) \quad (2.35)$$

where, $\dot{m}_{air}$ is mass flow rate of dry air, Cp_{air} is the specific heat capacity of dry air, W_g is the humidity ratio of the air, and Cp_v is the specific heat capacity of the water vapor.

Similarly, the heat capacity rate for the desiccant coated fibre material used in the exchangers is

$$C_{sl} = \dot{m}_{sl} Cp_{sl} \tag{2.36}$$

where $\dot{m}_{sl}$ is mass flow rate of solid and liquid mixture (i.e., the solid fibre, plus desiccant and adsorbed water), and Cp_{sl} is the specific heat capacity of the solid component including adsorbed water vapour.

The minimum heat capacity rate is the minimum of the air or solid porous media.

$$C_{\min} = \min\left\{C_g, C_{sl}\right\} \tag{2.37}$$

The number of transfer units (Ntu) and heat capacity ratio (Cr) are important dimensionless groups. They are defined below:

$$Ntu = \frac{h_{gsl} A}{C_{\min}} = \frac{h_{gsl} V S_v}{\min\left\{C_g, C_{sl}\right\}} \tag{2.38}$$

$$Ntu_g = \frac{h_{gsl} A}{C_g} = \frac{h_{gsl} V S_v}{C_g} \tag{2.39}$$

$$Ntu_{sl} = \frac{h_{gsl} A}{C_{sl}} = \frac{h_{gsl} V S_v}{C_{sl}} \tag{2.40}$$

$$C_r = \frac{C_{\min}}{C_{\max}} = \frac{\min\{C_g, C_{sl}\}}{\max\{C_g, C_{sl}\}} \tag{2.41}$$

The bulk air temperature and humidity ratio at the outlet of the exchangers are calculated using the following equations:

$$T_{g,out} = \frac{\int_0^{y_0} Cp_g \rho_{air} u_g T_{g,out} dy}{\int_0^{y_0} Cp_g \rho_{air} u_g dy} \tag{2.42}$$

$$W_{g,out} = \frac{\int_0^{y_0} \rho_{air} u_g W_{g,out} dy}{\int_0^{y_0} \rho_{air} u_g dy} = \frac{\int_0^{y_0} \rho_{air} u_g W_{g,out} dy}{\rho_{air} u_g y_0} \tag{2.43}$$

The bulk solid temperature and moisture content at the outlet of the exchangers are calculated with the following equations:

$$T_{sl,out} = \frac{\int_0^{x_0} (1-\varepsilon_g) Cp_{sl} \rho_{sl} u_{sl} T_{sl,out} dx}{\int_0^{x_0} (1-\varepsilon_g) Cp_{sl} \rho_{sl} u_{sl} dx} \tag{2.44}$$

$$U_{sl,out} = \frac{\int_0^{x_0} \varepsilon_l \rho_l u_{sl} dx}{\int_0^{x_0} \varepsilon_{si} \rho_{si} u_{sl} dx} = \frac{\int_0^{x_0} \varepsilon_l \rho_l u_{sl} dx}{\varepsilon_{si} \rho_{si} u_{sl} x_0} \tag{2.45}$$

2.4.2 Latent Effectiveness

The latent effectiveness is the ratio of actual moisture transfer to the maximum possible moisture transfer which would occur in an ideal exchanger that had an infinite moisture transfer surface area (Fan, 2005).

$$\varepsilon_l = \frac{\dot{m}_{air}\left(W_{g,in} - W_{g,out}\right)}{\min\left\{\dot{m}_{air}\left(W_{g,in} - W_{sl,in}\right), \dot{m}_{si}\left(U_{g,in} - U_{sl,in}\right)\right\}} \tag{2.46}$$

where, $W_{sl,in}$ is the humidity ratio that air would reach when in equilibrium with the desiccant at a moisture content of $U_{sl,in}$; $\dot{m}_{si}$ is mass flow rate of silica gel; $U_{g,in}$ is moisture content that the desiccant would attain when it is in equilibrium with air at a relative humidity of $\phi_{g,in}$.

2.4.3 Total Effectiveness

With the sensible effectiveness and the latent effectiveness of a single exchanger, the total effectiveness of a single exchanger is defined by the following equation (Simonson and Besant, 1999a):

$$\varepsilon_t = \frac{\varepsilon_s + \varepsilon_l H^*}{1 + H^*} \tag{2.47}$$

$$H^* = 2500\frac{\Delta W}{\Delta T} \tag{2.48}$$

$$\Delta W = W_{g,in} - W_{sl,in} \tag{2.49}$$

$$\Delta T = T_{g,in} - T_{sl,in} \tag{2.50}$$

where H^* is the operating condition factor, ΔW is the inlet humidity ratio difference between the air and the solid surface (kg/kg), and ΔT is the inlet temperature difference between the air and solid or liquid ($^\circ C$, K).

2.4.4 Run-around System's Effectiveness

When the run-around system reaches steady state, the overall effectiveness values of the system are expressed as follows, which utilize the air properties in the supply and exhaust air streams only.

Sensible effectiveness

$$\varepsilon_{o,s} = \frac{C_{gS}T_{g,inS} - C_{gS}T_{g,outS}}{C_{g,\min}(T_{g,inS} - T_{g,inE})} = \frac{C_{gE}T_{g,outE} - C_{gE}T_{g,inE}}{C_{g,\min}(T_{g,inS} - T_{g,inE})} \tag{2.51}$$

where $C_{g,\min}$ is the minimum of C_{gS} and C_{gE}.

Latent effectiveness

$$\varepsilon_{o,l} = \frac{\dot{m}_{air,S}\left(W_{g,inS} - W_{g,outS}\right)}{\dot{m}_{\min}\left(W_{g,inS} - W_{g,inE}\right)} = \frac{\dot{m}_{air,E}\left(W_{g,outE} - W_{g,inE}\right)}{\dot{m}_{\min}\left(W_{g,inS} - W_{g,inE}\right)} \tag{2.52}$$

where, $\dot{m}_{\min}$ is the minimum of $\dot{m}_{air,S}$ and $\dot{m}_{air,E}$.

Total effectiveness

$$\varepsilon_{o,t} = \frac{\dot{m}_{air,S}\left(H_{g,inS} - H_{g,outS}\right)}{\dot{m}_{\min}\left(H_{g,inS} - H_{g,inE}\right)} = \frac{\dot{m}_{air,E}\left(H_{g,outE} - H_{g,inE}\right)}{\dot{m}_{\min}\left(H_{g,inS} - H_{g,inE}\right)} \tag{2.53}$$

Chapter 3

MODEL VERIFICATION

3.1 Introduction

In this chapter, the accuracy of the model for sensible and latent heat transfer within a single exchanger is verified by comparing the simulations with well-known theoretical solutions for a single cross flow heat exchanger. The model is also verified for sensible and latent heat transfer in a run-around system by comparing the simulations with correlations for a run-around heat recovery system and an energy wheel.

3.2 A single Exchanger with Heat Transfer only

The results from the model are compared with heat transfer solutions and correlations from the literature. The inlet temperatures are $T_{air,in}$ = 308K (34.85 °C) for the air stream, and $T_{sl,in}$ = 297K (23.85 °C) for the desiccant coated fibre. There is no moisture transfer between the two streams, so $C_s = C_{sl}$. The volume fraction of the fibre glass is 0.1%, and the volume fraction of the silica gel is 0.5%.

The effectiveness for two unmixed fluids flowing through a cross-flow heat exchanger is expressed by the correlation (Incropera and Dewitt, 1996):

$$\varepsilon_s = 1 - \exp\left[\left(\frac{1}{Cr}\right)(Ntu)^{0.22}\left\{\exp\left[-Cr(Ntu)^{0.78}\right]-1\right\}\right] \tag{3.1}$$

A comparison of the effectiveness values obtained from the correlation and numerical model are shown in Figure 3.1. The numerical results agree with the correlation results. For example, when the capacity ratio (Cr) is 0.5 (Cs>Cg), the difference between the numerical and analytical is less than 1.6% for $0.25 \le Ntu \le 4$, and less than 1% for $4 < Ntu \le 18$. For the same Ntu, the effectiveness is the smallest when Cr = 1, and the effectiveness increases as Cr decreases. The effectiveness increases significantly as Ntu increases from 0 to 6 for different Cr values, and only increases slightly as Ntu increases above 6. For the same Cr and Ntu, the numerical effectiveness is almost the same for both Cs>Cg and Cs<Cg.

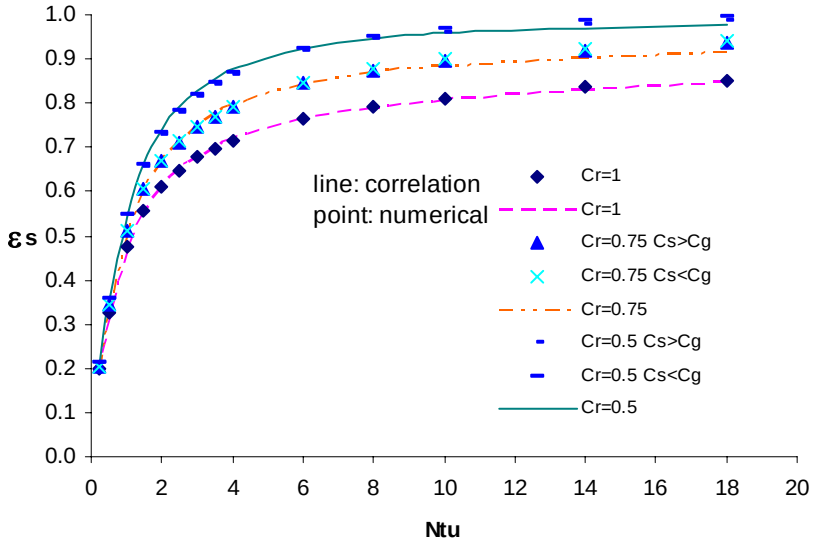

Figure 3.1 Comparison between the sensible energy effectiveness of a single exchanger calculated with the numerical model and the correlation from the literature.

The numerical model can be further verified using the analytical solution of Mason (1955). Mason (1955) obtained the analytical solution for the dimensionless temperature profile in a cross-flow flat-plate heat exchanger with both fluids unmixed, $C_s = C_g$ and constant properties. The equation is:

$$\theta\left(X^*, Y^*\right) = e^{-(Ntu_g)Y^* - (Ntu_s)X^*} \sum_{n=0}^{\infty} \left[\frac{(Ntu_g)(Ntu_s)X^*Y^*}{(n!)^2} \right]^n \tag{3.2}$$

$$\text{where, } \theta\left(X^*, Y^*\right) = \frac{T_{air}\left(X^*, Y^*\right) - T_s\left(X^*, Y^*\right)}{T_{air,in} - T_{s,in}} \tag{3.3}$$

Although the model in this research is a solid-liquid exchanger, the analytical solution (3.2) can be used to verify the numerical results. For Ntu = 1, shown in Figure 3.2 (a), the numerical results are in very good agreement with analytical results in the whole bed. In the area with large temperature differences and heat flux, the difference between the numerical and analytical solutions is less than 1%. For Ntu = 2, shown in Figure 3.2(b), the analytical and numerical results are in close agreement in the region $X^* < 0.6$ and $Y^* < 0.6$ where the heat flux is large. In most of this area, the difference between the analytical and numerical solutions is less than 5%. There are some larger differences for $X^* > 0.6$ and $Y^* > 0.6$, but the actual temperature differences and the heat fluxes are small in this region, and as a result, the simulated effectiveness of the heat exchanger is very close to the effectiveness from the correlation equation (3.1).

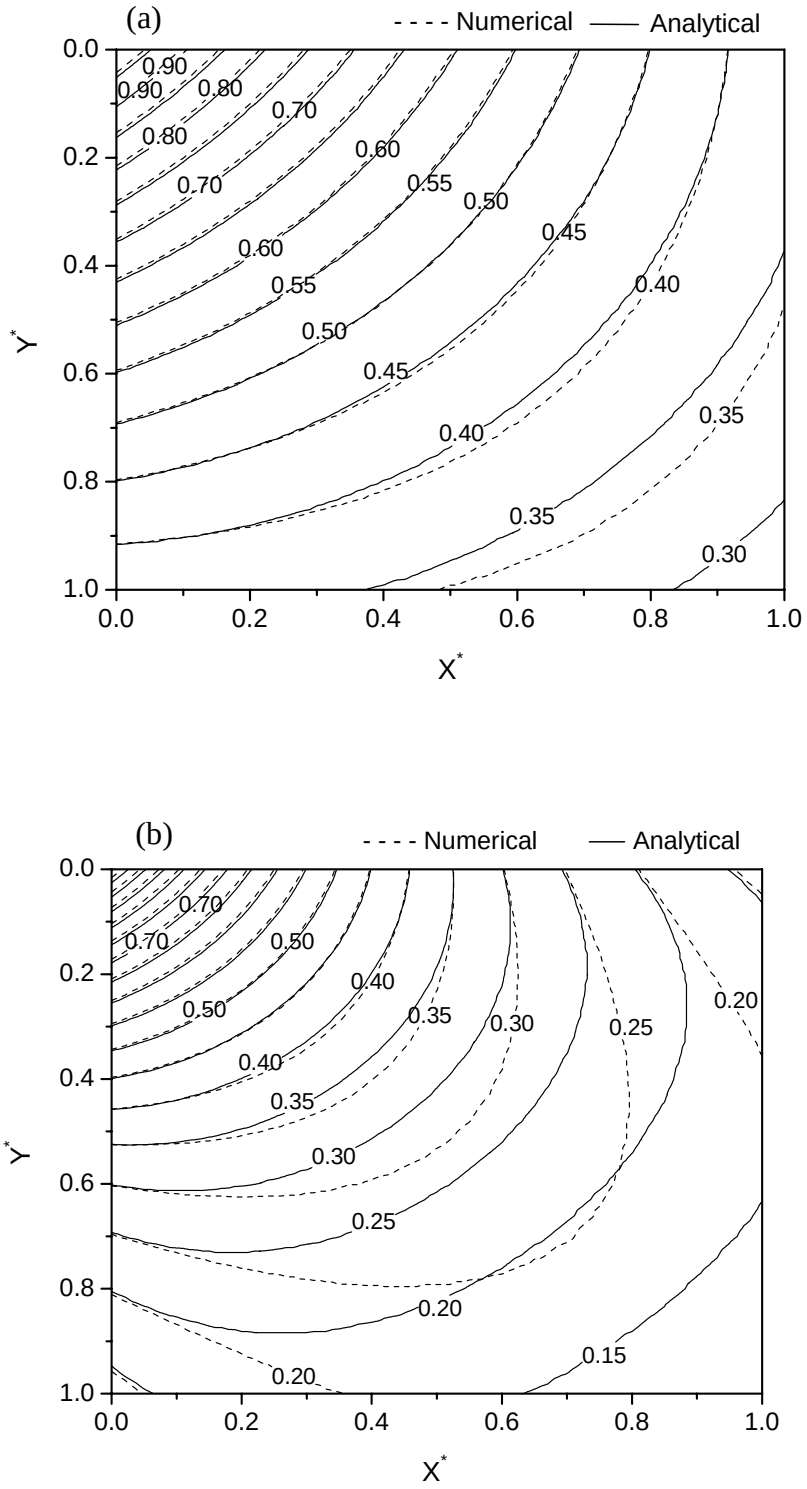

Figure 3.2 Comparison of dimensionless temperature difference, θ, for the analytical and numerical results, with $C_s = C_g$ and (a) Ntu = 1 and (b) Ntu = 2.

Figure 3.3 and Figure 3.4 show the temperature distribution within the dry air and the solid with the same Ntu, but different heat capacity ratios, Cr. In these two operating conditions, the air velocity is the same, but the solid heat capacity rate is $C_s = 2C_g$ (Figure 3.4) and is $C_s = C_g$ (Figure 3.3). The bulk mean outlet temperature is obviously different for these two heat capacity ratios. The bulk outlet air temperature is lower and the bulk outlet solid temperature is higher with $C_s = 2C_g$ (Figure 3.4) than with $C_s = C_g$ (Figure 3.3).

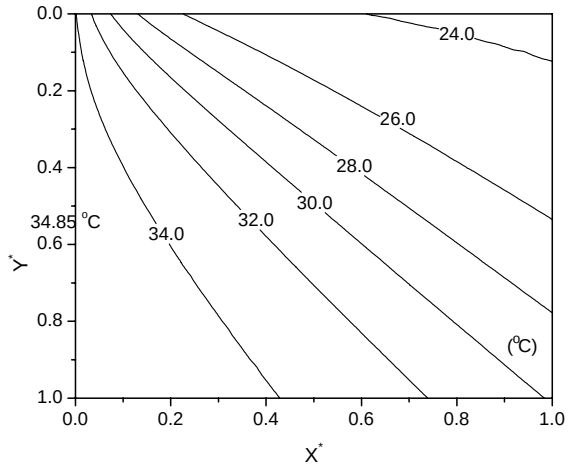

$T_g\left(X^*, Y^*\right)\ \left(^oC\right)$ distribution for air.

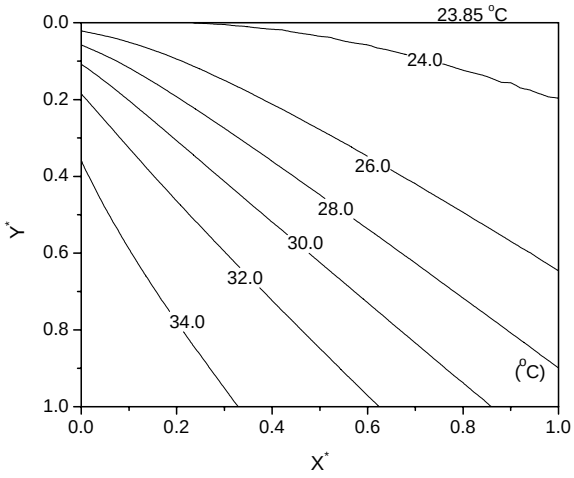

$T_s\left(X^*, Y^*\right)\left(^oC\right)$ distribution for solid.

Figure 3.3 Temperature distributions for Ntu = 8, and $C_s = C_g$ ($T_{air,in}$ = 308K (34.85 °C), $T_{s,in}$ = 297K (23.85 °C)).

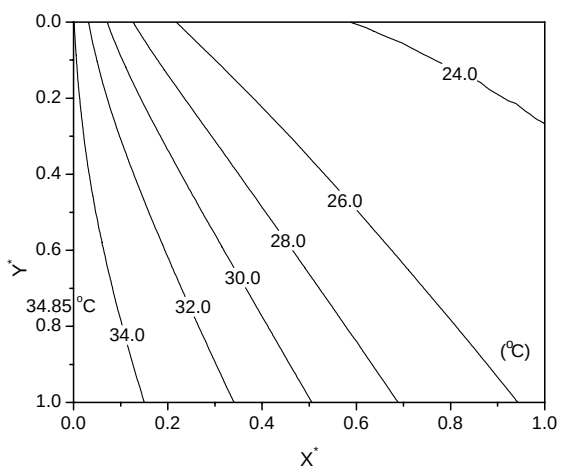

$T_g\left(X^*, Y^*\right)\left(^oC\right)$ distribution for air.

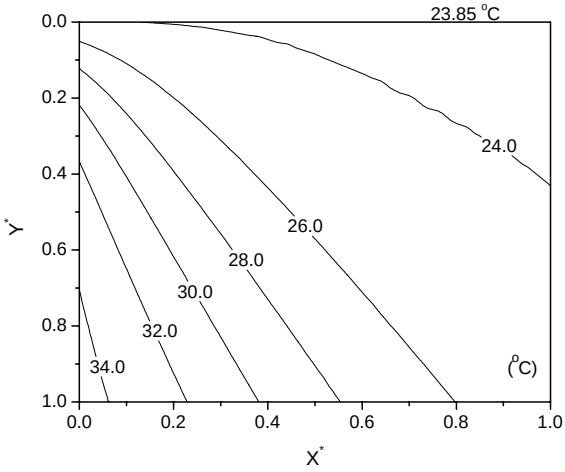

$T_s\left(X^*, Y^*\right)\left(^oC\right)$ distribution for solid.

Figure 3.4 Temperature distributions for Ntu = 8, and $C_s = 2C_g$ ($T_{air,in}$ = 308K (34.85 °C), $T_{s,in}$ = 297K (23.85 °C)).

3.3 Run-around System with Heat Transfer only

In this section, the results and equations for a run-around system from the literature are used to verify the numerical model. The inlet properties for dry air are as follows:

Supply air side: $T_{air,inS}$ = 308K (34.85 °C)

Exhaust air side: $T_{air,inE}$ = 297K (23.85 °C)

Zeng et al. (1992) showed that the overall effectiveness of the run-around heat recovery system, ε_0, is a function of the Ntu and Cr of each exchanger. For the air-to-solid run-around system, this relationship can be written in the form:

$$\frac{1}{\varepsilon_o} = \frac{C_{\min,g}}{\varepsilon_E \cdot C_{\min,E}} + \frac{C_{\min,g}}{\varepsilon_S \cdot C_{\min,S}} - \frac{C_{\min,g}}{C_s}. \tag{3.4}$$

If the heat capacity ratios in both the supply and exhaust sides are equal, $Cr_S = Cr_E$, and with the same heat transfer units, $Ntu_S = Ntu_E$, equation (3.4) can be simplified to, for $C_g \le C_s$:

$$\frac{1}{\varepsilon_o} = \frac{1}{\varepsilon_E} + \frac{1}{\varepsilon_S} - Cr, \tag{3.5}$$

where $Cr = C_g / C_s$,

and, for $C_g > C_s$:

$$\frac{1}{\varepsilon_o} = \frac{1}{Cr}\left(\frac{1}{\varepsilon_E} + \frac{1}{\varepsilon_S} - 1\right) \tag{3.6}$$

where $Cr = C_s / C_g$.

The analytical and numerical results are shown in Figure 3.5. For the same Ntu, the effectiveness is the largest when Cr = 1, and effectiveness decreases as Cr decreases. For the same Cr and Ntu, the effectiveness is larger when Cs>Cg than when Cs<Cg. The numerical results match very well with the analytical results. The largest difference is 2.7% when $1 \le Ntu \le 18$.

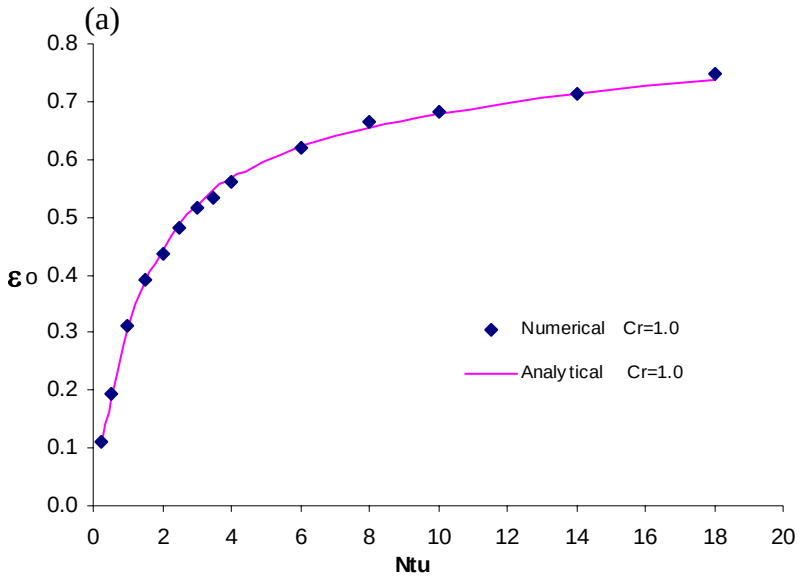
(a)
0.8
0.7
0.6
0.5
εo 0.4
0.3
0.2
0.1
0.0
0
2
4
6
8
10
12
14
16
18
20
Ntu
Numerical Cr=1.0
Analytical Cr=1.0

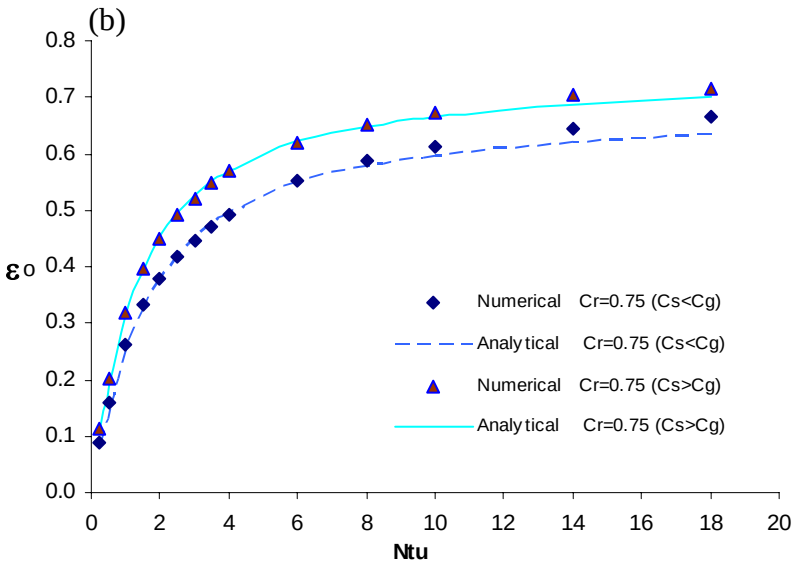
(b)
0.8
0.7
0.6
0.5
εo 0.4
0.3
0.2
0.1
0.0
0
2
4
6
8
10
12
14
16
18
20
Ntu
Numerical Cr=0.75 (Cs<Cg)
Analytical Cr=0.75 (Cs<Cg)
Numerical Cr=0.75 (Cs>Cg)
Analytical Cr=0.75 (Cs>Cg)

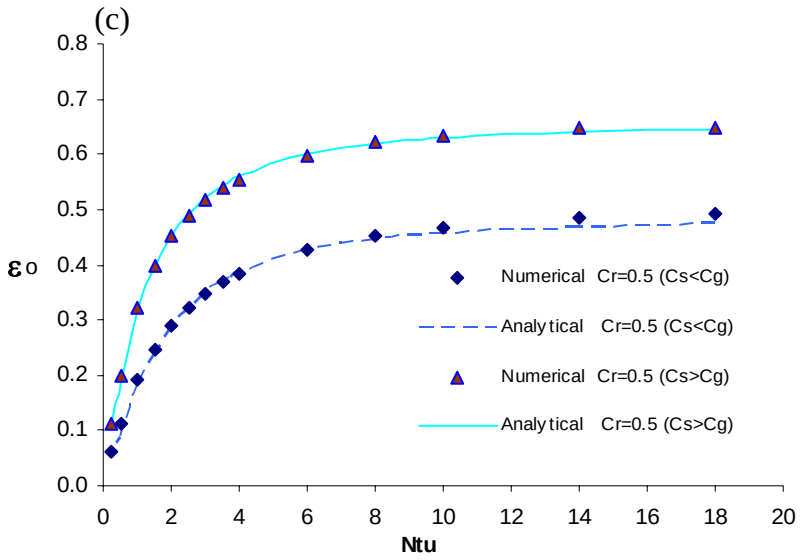

Figure 3.5 The analytical and numerical effectiveness results for (a) Cr = 1, (b) Cr = 0.75 and (c) Cr = 0.5

3.4 Counter Flow Heat and Moisture Regenerator (Energy Wheel)

In order to further verify the numerical model developed in this thesis, the numerical results will be compared to results in the literature for energy wheels, which exchange heat and moisture using the desiccant coated surface of the wheel matrix as it rotates. To pursue this comparison, the well-mixed bulk temperature and moisture content for the solid moving bed at the exit of each exchanger, as used previously and described in Section 2.3.5, will be altered so that the temperature and moisture content distributions will be retained before the solid particles enter the supply (S) and exhaust (E) exchangers. With this change, the desiccant coated solid behaviour is similar to that for rotary energy wheels. A counter-flow arrangement is achieved by interchanging the solid material flow as shown in Figure 3.6, where the solid material that exits the supply exchanger near the air inlet is transported to the exhaust exchanger near the air outlet.

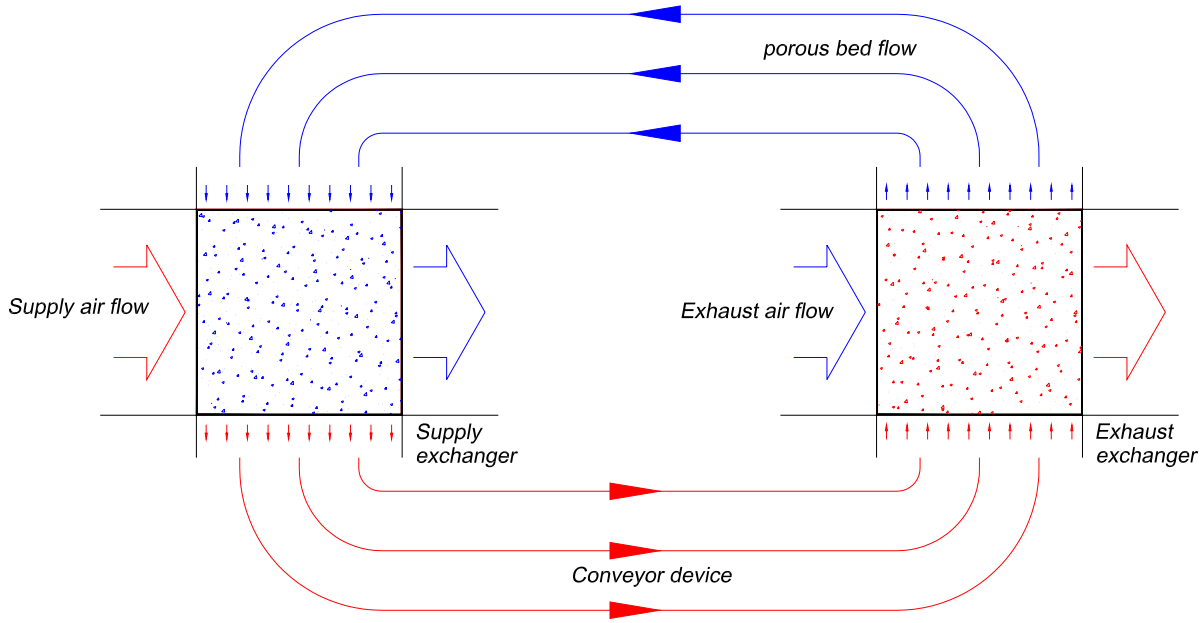

Figure 3.6 Schematic diagram of a run-around energy recovery system with a counter-flow arrangement.

The boundary condition equations at y = 0 to create this interchange in the model are:

$$T_{sl(i,1)S} = T_{sl(m-i+1,n)E} \tag{3.7}$$

$$T_{sl(i,1)E} = T_{sl(m-i+1,n)S} \tag{3.8}$$

$$U_{sl(i,1)S} = U_{sl(m-i+1,n)E} \tag{3.9}$$

$$U_{sl(i,1)E} = U_{sl(m-i+1,n)S} \tag{3.10}$$

Figure 3.7 shows the effectiveness of a counter-flow run-around system for the ARI summer test condition $T_{g,in} = 35\ ^{\circ}C$, $\phi_{g,in} = 47.4\%$, $T_{sl,in} = 23.9\ ^{\circ}C$, $\phi_{sl,in} = 51.2\%$ with

Ntu = 10. The sensible, latent and total effectiveness increases with the increase of C_{sl}/C_g.

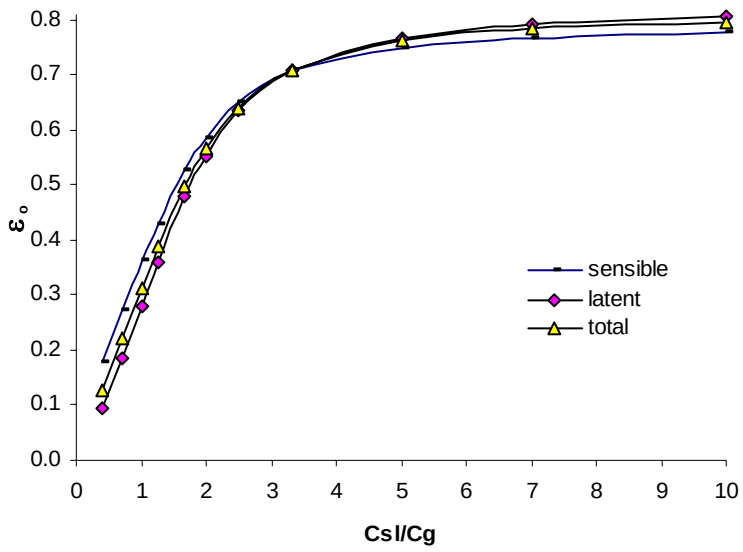

Figure 3.7 The overall system effectiveness in counter-flow run-around system for ARI summer test conditions and Ntu = 10.

Simonson and Besant (1999b) developed the following correlations for the effectivenesses of energy wheels:

$$\varepsilon_s = \frac{Ntu_o}{1+Ntu_o}\left(1-\frac{1}{7.5Cr_{sg}}\right)-\left(\frac{0.26\left(\frac{Cr_{sg}}{Wm^2Cr_{m,sg}}\right)^{0.28}}{7.2Cr_{sg}^{\ 1.53}+\frac{210}{Ntu_o^{\ 2.9}}-5.2}+\frac{0.31\eta}{Ntu_o^{\ 0.68}}\right)H^* \qquad (3.11)$$

$$\varepsilon_l = \frac{Ntu_o}{1+Ntu_o}\left(1-\frac{1}{0.54Cr_{mt}^{\ 0.86}}\right)\left(1-\frac{1}{Ntu_o^{\ 0.51}Cr_{mt}^{\ 0.54}H^*}\right) \qquad (3.12)$$

$$\varepsilon_t = \frac{\varepsilon_s + \varepsilon_l H^*}{1 + H^*} \tag{3.13}$$

where,

$$Cr_{sg} = \frac{C_s}{C_g} \tag{3.14}$$

$$Cr_{m,sg} = \frac{\dot{m}_s}{\dot{m}_g} \tag{3.15}$$

$$Cr_{mt} = Cr_{m,sg}{}^{0.58} Wm^{0.33} \left(\left. \frac{\partial U}{\partial \phi} \right|_{\phi ave} \right)^{0.2} Cr_{sg}{}^{1.13} \left(\frac{e^{\left(\frac{1482}{T_{ave}} \right)}}{47.9} - 1.26 \phi_{ave}{}^{0.5} \right)^{4.66} \tag{3.16}$$

η is the fraction of the phase change energy that is delivered directly to the air which is assume to be $\eta = 0$ in this thesis. Cr_{mt} is the moisture transfer group ratio for an energy wheel. T_{ave} (K) and ϕ_{ave} are the average temperature and relative humidity between the supply air and exhaust air inlet conditions.

It should be noted that in run-around system correlations, Ntu_0 is defined for a single exchanger ($Ntu_o = Ntu$), but in the energy wheel correlations it is based on the whole exchanger ($Ntu_o = Ntu/2$), which means the Ntu in the run-around system is twice that of the energy wheel in this comparison.

Figure 3.8 shows the comparison between the energy wheel and counter-flow run-around system in summer ARI conditions with $C_{sl}/C_g = 10$. Although there are some differences for the sensible effectiveness, the latent and total effectiveness are in very good agreement. When $2 \le Ntu \le 10$, the sensible effectiveness relative difference is less than 15%, and is 4.1% when $Ntu = 10$; the latent effectiveness relative difference is less than 6%, and is 0.7% when $Ntu = 10$; but the total effectiveness relative difference is less than 2%. The differences between the sensible effectiveness value calculated from the energy correlations and those calculated by the numerical model are likely due to heat conduction in the porous bed, which is included in the numerical model but assumed negligible in the correlation of equations (3.11) to (3.16).

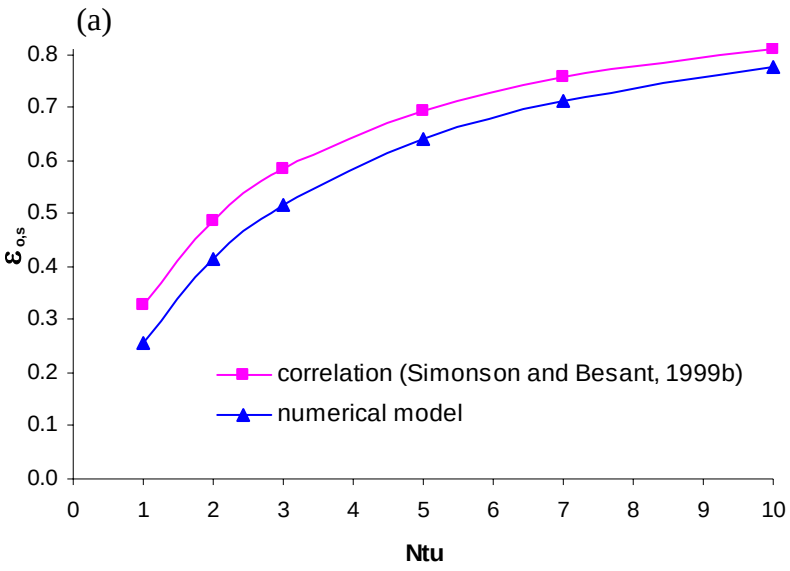

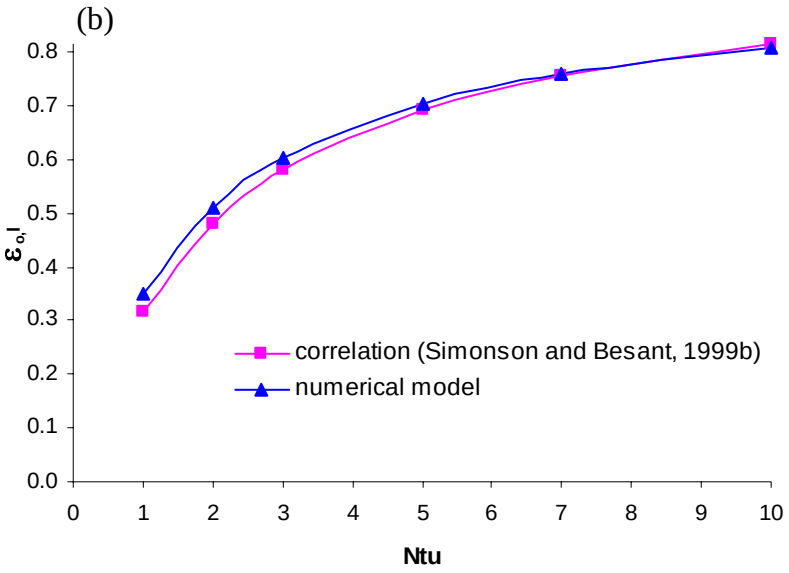

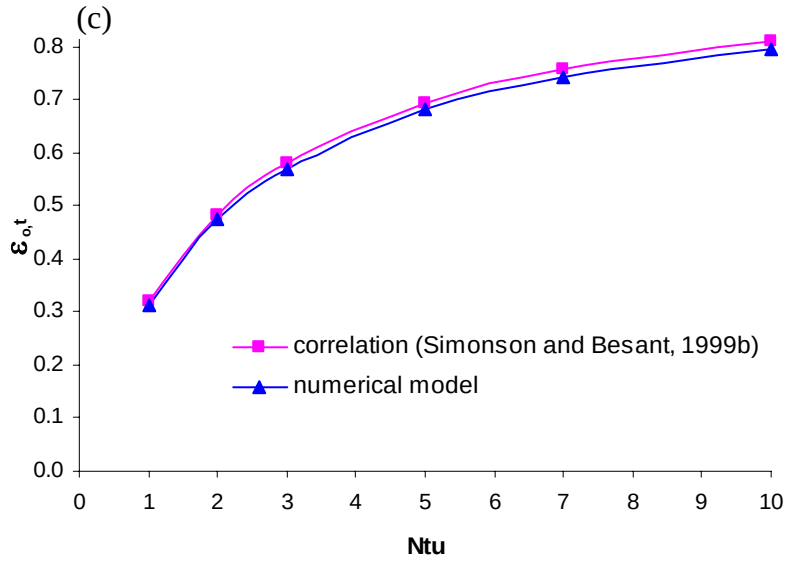

Figure 3.8 Comparison between energy wheel and counter-flow run-around system (a) sensible, (b) latent, and (c) total effectivenesses for summer ARI conditions and $C_{sl} / C_g = 10$.

Figure 3.9 shows the comparison between the energy wheel and counter-flow run-around system in winter ARI conditions with $C_{sl} / C_g = 10$. The sensible, latent and total effectiveness are in very good agreement.

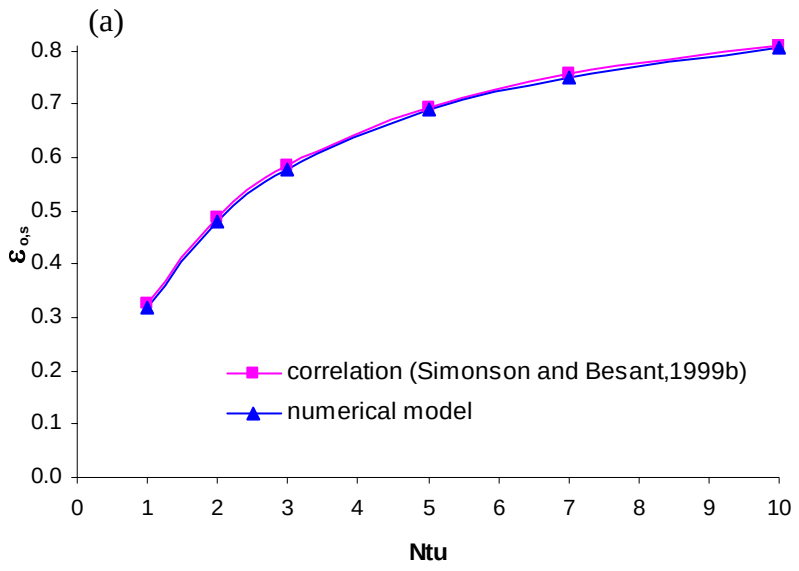
(a)
0.8
0.7
0.6
0.5
0.4
0.3
0.2
0.1
0.0
$\varepsilon_{o,s}$
correlation (Simonson and Besant,1999b)
numerical model
0
1
2
3
4
5
6
7
8
9
10
Ntu

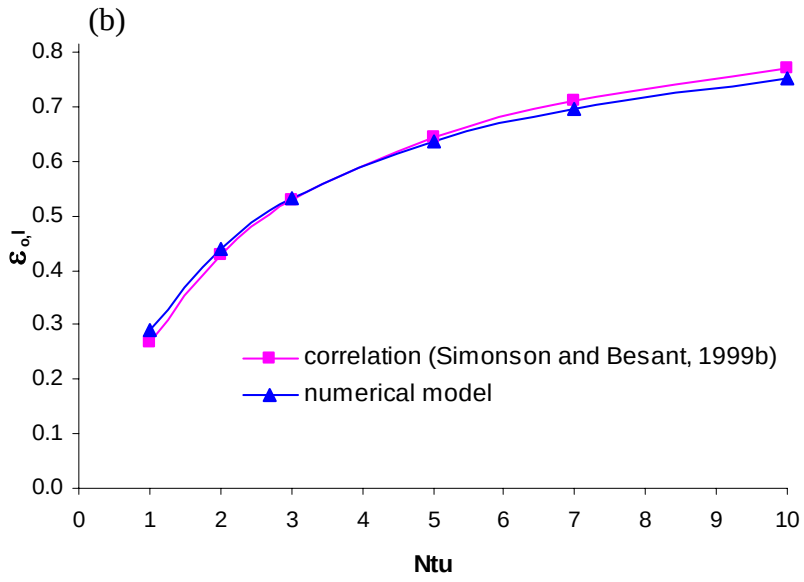
(b)
0.8
0.7
0.6
0.5
0.4
0.3
0.2
0.1
0.0
$\varepsilon_{o,l}$
correlation (Simonson and Besant, 1999b)
numerical model
0
1
2
3
4
5
6
7
8
9
10
Ntu

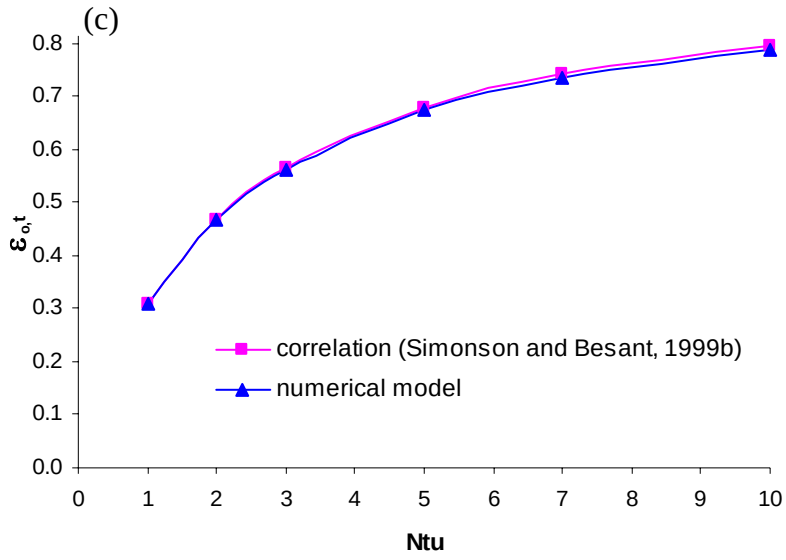

Figure 3.9 Comparison between energy wheel and counter-flow run-around system (a) sensible, (b) latent, and (c) total effectivenesses for winter ARI conditions and $C_{sl} / C_g = 10$.

Figure 3.8 and Figure 3.9 show that the results of the numerical model are in agreement with energy wheel correlations from the literature after changing the flow pattern from a cross-flow run-around to a counter-flow run-around configuration, and verifies the accuracy of the heat and moisture transfer model presented in Chapter 2.

In summary, the model has been verified for heat transfer in a single exchanger, heat transfer in a run-around system, and heat and moisture transfer in a run-around counter-flow system (comparable to an energy wheel).

Chapter 4

THE SIMULATED RESULTS

4.1 Introduction

The governing equations for heat and moisture transfer in the novel run-around system that uses a solid material to transport heat and moisture between remote air streams are listed in Chapter 2. In Chapter 3, the accuracy of the model was verified for the heat and moisture transfer in the run-around system by comparing to effectiveness correlations in the literature. In this chapter, heat transfer only and heat transfer coupled with moisture transfer in the run-around system are investigated to demonstrate the performance and operation characteristics of the run-around system.

4.2 The Results for a Run-around System with Heat Transfer only

For the run-around system with heat transfer only, Figure 4.1 shows the sensitivity of the overall effectiveness to changes in Cr ($Cr = C_{\min} / C_{\max}$) and Ntu. For $C_s < C_g$ and a constant Ntu, the effectiveness decreases as Cr decreases. For $C_s > C_g$, constant Ntu (i.e., a constant air velocity) and Ntu < 3, the overall effectiveness remains almost constant and independent of the velocity of the porous bed. When Ntu > 3, the effectiveness decreases as Cr decreases which means that the effectiveness decreases as

the velocity of the porous bed increases. At a constant Ntu and Ntu > 1, the maximum effectiveness occurs at $\mathrm{Cr} \approx 1$.

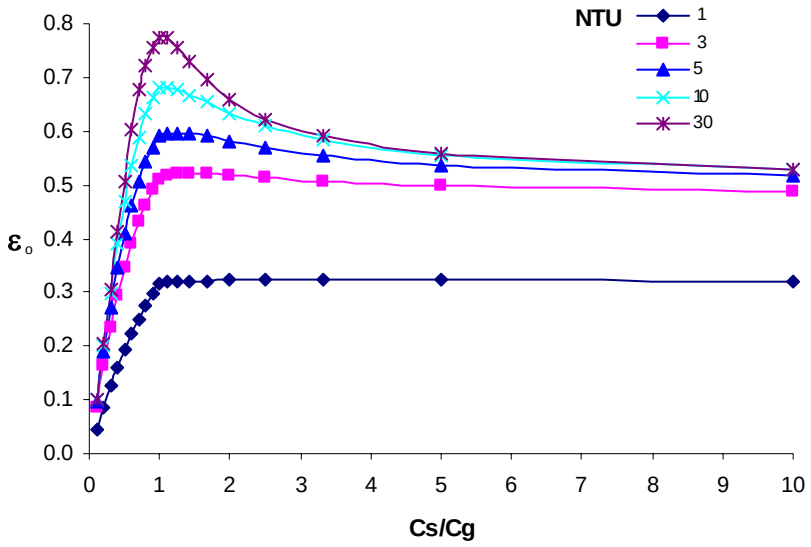

Figure 4.1 Overall effectiveness versus C_s / C_g for the run-around system with heat transfer only and with Ntu as a parameter.

In order to obtain the maximum effectiveness during peak load conditions, C_s / C_g should be kept in the range from 0.9 to 1.2. For example, with $0.9 \le C_s / C_g \le 1.2$, and Ntu = 5, the overall sensible effectiveness of the run-around system will be almost 60%. With the same C_s / C_g and Ntu = 10, the overall sensible effectiveness can be almost 70%. During part load conditions, the overall effectiveness can be reduced to match the load by reducing C_s (i.e., by reducing the velocity of the porous bed).

4.3 Single Exchanger with Heat and Moisture Transfer

In each exchanger, the porous bed's properties are shown in Table 4.1. These are the same as in Chapter 3. The operating conditions for the exchanger are chosen as in Table 4.2. These inlet properties will be used to illustrate the behaviour of a single exchanger during two somewhat extreme operating conditions in the summer when the solid desiccant is warm and moist or warm and dry.

Table 4.1 Parameters and properties of each heat and moisture exchanger

Size of the exchanger	$x_0 \times y_0 \times z_0$	$0.3\,m \times 0.3\,m \times 0.3\,m$
Fibre glass volume fraction	ε_f	0.1%
Silica gel volume fraction	ε_{si}	0.5%

Table 4.2 Selected operating conditions of one heat and moisture exchanger

	Moist desiccant	Dry desiccant
Inlet temperature of the air stream	$35\ ^{\circ}C$	$35\ ^{\circ}C$
Inlet relative humidity of the air stream	47.4%	47.4%
Inlet humidity ratio of the air stream	$16.90\,g/kg$	$16.90\,g/kg$
Inlet temperature of the solid stream	$23.9\ ^{\circ}C$	$23.9\ ^{\circ}C$
Inlet equilibrium relative humidity of the solid stream	51.2%	25%
Inlet equilibrium humidity ratio of the solid stream	$9.51\,g/kg$	$4.61\,g/kg$

The temperature and humidity ratio distributions for moist desiccant operating conditions ($T_{g,in} = 35\ ^{\circ}C$, $\phi_{g,in} = 47.4\%$, $T_{sl,in} = 23.9\ ^{\circ}C$, $\phi_{sl,in} = 51.2\%$) with Ntu = 6, and Cr = 1 are presented in Figure 4.2. Inside the exchanger, the air temperature is higher than that of solid, and heat is transferred from air to the solid. As the air flows through the exchanger, moisture is adsorbed by the desiccant, and adsorption heat is delivered to the solid. The air humidity ratio is lower at the outlet of the exchanger than at the inlet, and solid equilibrium humidity ratio is higher at the outlet than at the inlet. The moisture is transferred from the air to the solid for most of the exchanger, but in the bottom-left corner (X^* full range, Y^* large), moisture is transferred from the solid to air because the humidity ratio (vapour density) of the solid is higher than that of the adjacent moist air.

In Figure 4.3, the temperature and humidity ratio distributions for the case where the solid entering the exchanger is dry ($T_{g,in} = 35\ ^{\circ}C$, $\phi_{g,in} = 47.4\%$, $T_{sl,in} = 23.9\ ^{\circ}C$, $\phi_{sl,in} = 25\%$ with Ntu = 6, and Cr = 1) are presented. Here only $\phi_{sl,in}$ is different compared with the operating conditions in Figure 4.2. During this operating condition, the temperature distribution in Figure 4.3(a) shows that in part of the exchanger the air temperature increases and then decreases as it flows through the exchanger. The air temperature in the bottom-left region of Figure 4.3(a) (X^* full range, Y^* large) is higher than the temperature of the air entering the exchanger. In this region, the solid temperature is higher than that of air. The bulk temperature of the air at the outlet is higher than that of the air at the inlet, even though the temperature of the solid at the

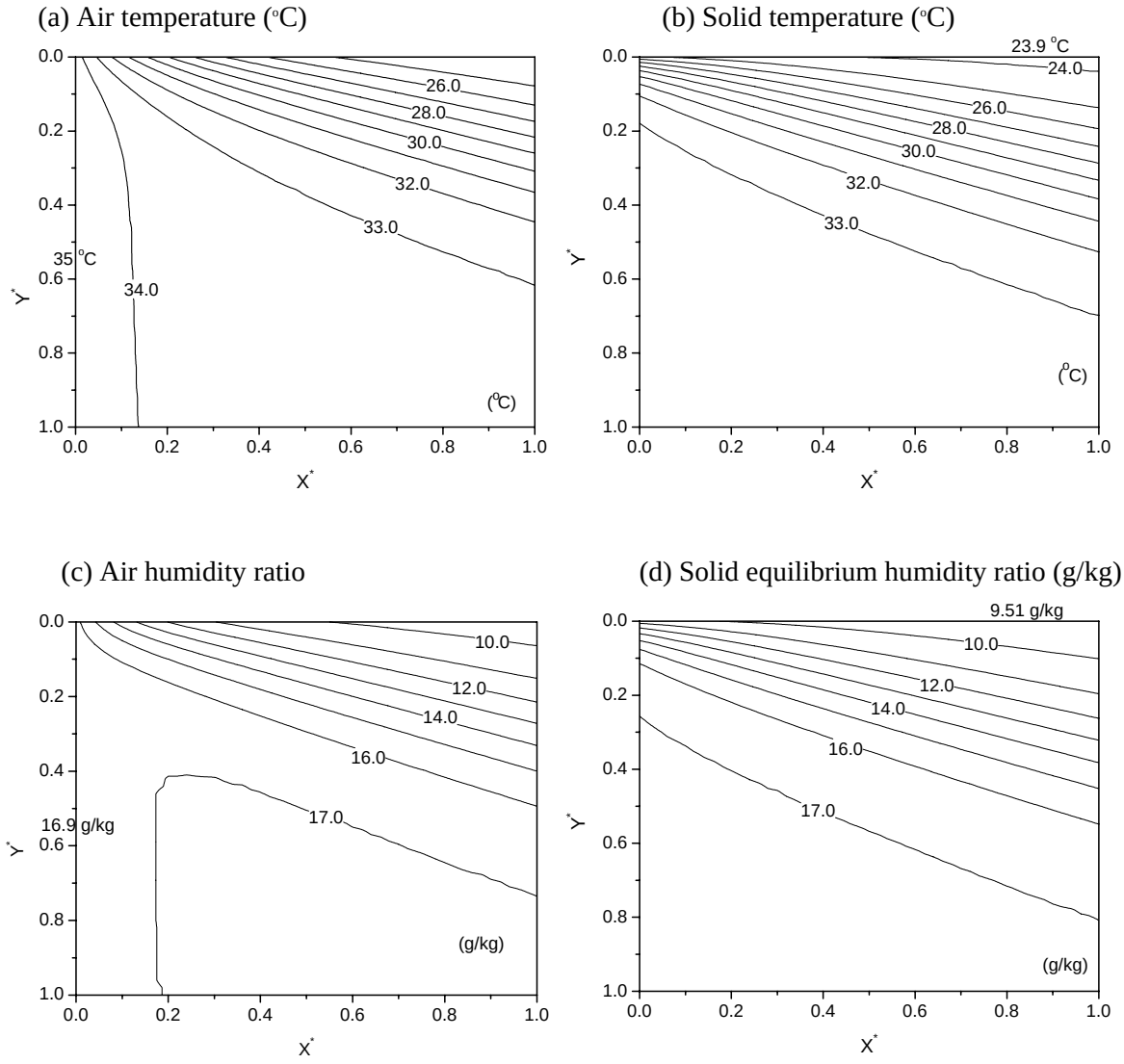

Figure 4.2 Distributions of (a) air temperature, (b) solid temperature, (c) air humidity ratio, and (d) solid equilibrium humidity ratio for the operating conditions of $T_{g,in} = 35\ ^{\circ}C$, $\phi_{g,in} = 47.4\%$, $T_{sl,in} = 23.9\ ^{\circ}C$, $\phi_{sl,in} = 51.2\%$ with Ntu = 6 and Cr = 1.

inlet is lower than the temperature of the air at the inlet. This occurs because a large amount of adsorbed water accumulates on the desiccant surface due to the large relative humidity (vapour density) difference between the air and the solid. As water is adsorbed,

the heat of sorption is delivered to the solid and this sorption heat release is large enough to make the solid temperature higher than that of the adjacent air.

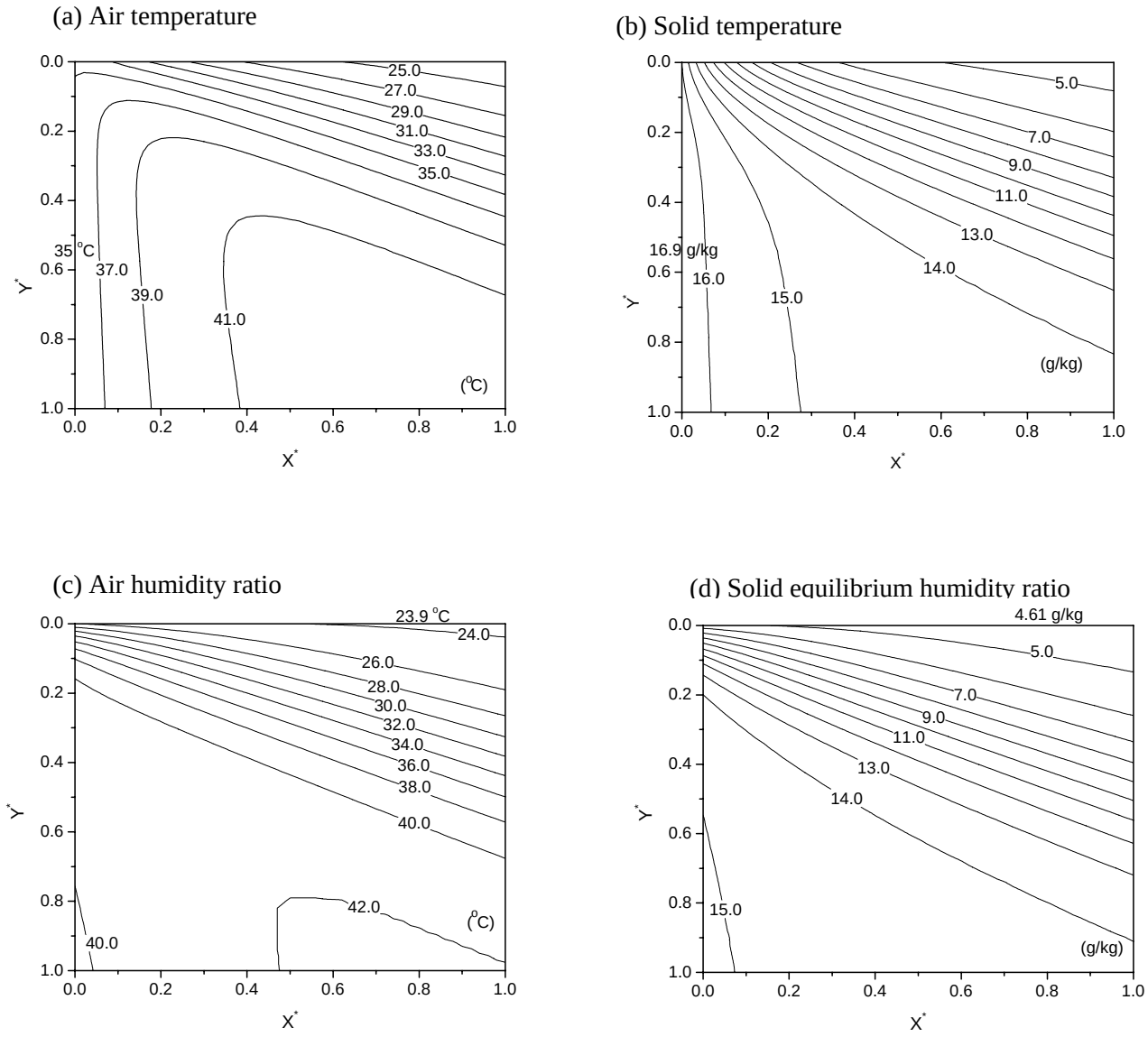

Figure 4.3 Distributions of (a) air temperature, (b) solid temperature, (c) air humidity ratio, and (d) solid equilibrium humidity ratio for the operating conditions: $T_{g,in} = 35\ ^{\circ}C$, $\phi_{g,in} = 47.4\%$, $T_{sl,in} = 23.9\ ^{\circ}C$, $\phi_{sl,in} = 25\%$ with Ntu = 6 and Cr = 1.

Figure 4.4 and Figure 4.5 are used to illustrate the effect of changing the capacity ratio Cr. In Figures 4.4 and 4.5, the temperature and humidity ratio distribution are presented

for the moist operating condition in Table 4.2 with Ntu = 6, and Cr = 0.3. The results in Figure 4.4 are for $C_{sl} < C_g$ and the results in Figure 4.5 are for $C_{sl} > C_g$. Figure 4.4 shows that there are only small temperature and humidity ratio differences between the

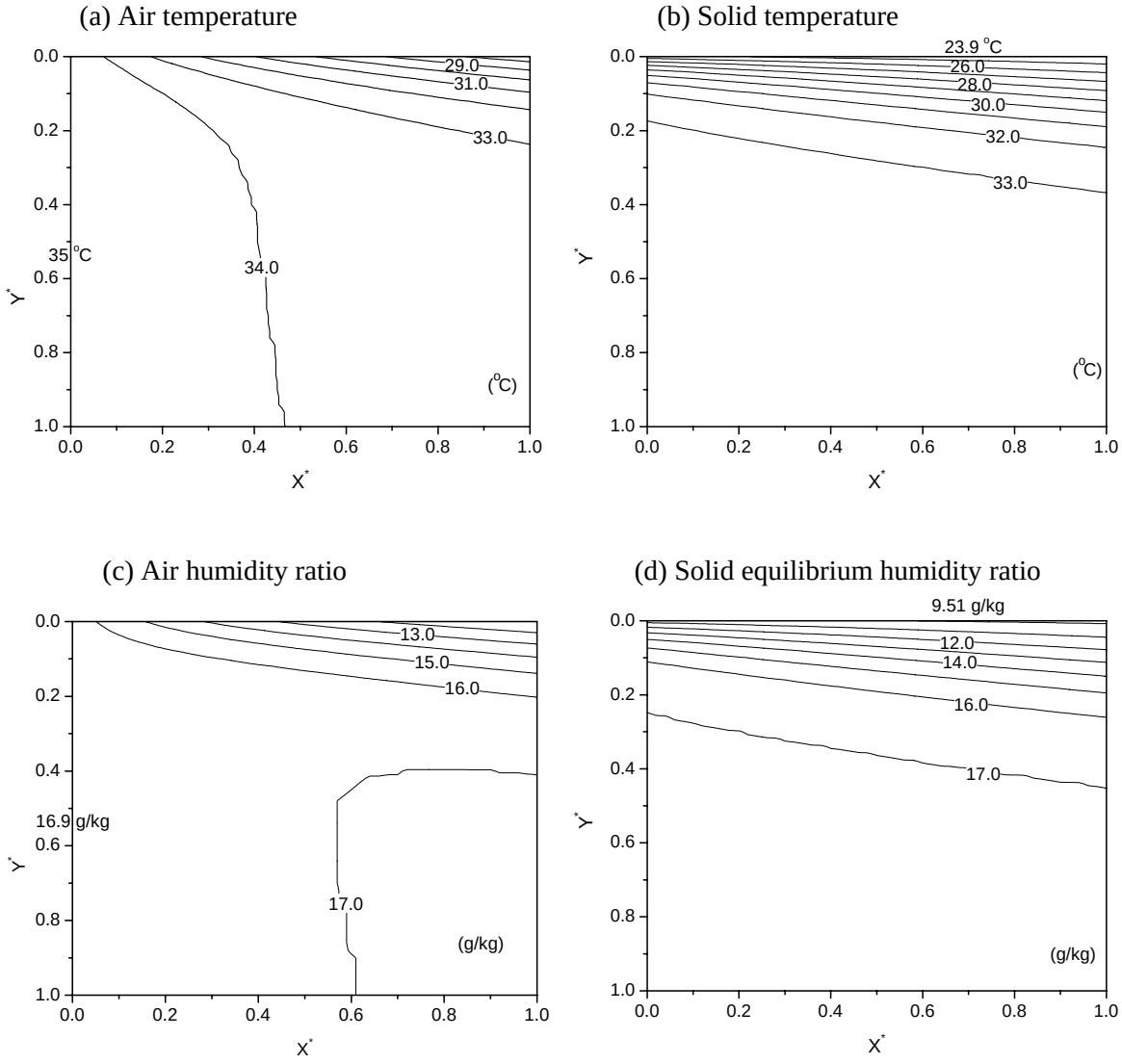

Figure 4.4 Distributions of (a) air temperature, (b) solid temperature, (c) air humidity ratio, and (d) solid equilibrium humidity ratio for operating condition $T_{g,in} = 35\ ^{\circ}C$, $\phi_{g,in} = 47.4\%$, $T_{sl,in} = 23.9\ ^{\circ}C$, $\phi_{sl,in} = 51.2\%$ with Ntu = 6 and Cr = 0.3 ($C_{sl} < C_g$).

inlet and outlet of the exchanger on the air side, but there are large temperature and humidity ratio differences between inlet and outlet on the solid side. This is expected because the capacity rate of the solid is much lower than that of the air.

Figure 4.5 shows that there are large temperature and humidity ratio differences between the inlet and outlet of the exchanger on both the air and solid sides. The temperature and humidity ratio distributions in Figure 4.5 have a similar shape to those presented in Figure 3.3 for sensible heat transfer only with $C_{sl} = C_g$ (Cr = 1). Since Cr = 1 is the optimal capacity ratio for sensible exchangers, this may indicate that the optimal capacity ratio for a run-around moisture exchanger is Cr = 0.3 with $C_{sl} > C_g$. This is consistent with the results of Fan et al. (2006). The temperature and humidity ratio contours in Figure 4.5 are quite different than those in Figure 4.4, even though they have the same heat capacity ratio.

Although the temperature and humidity distributions with the heat and moisture exchanger are useful, the performance of a single heat and moisture exchanger is better quantified by effectivenesses. The sensible and latent effectivenesses under ARI summer operating conditions (ARI (2005) $T_{g,in} = 35\ ^{\circ}C$, $\phi_{g,in} = 47.4\%$, $T_{sl,in} = 23.9\ ^{\circ}C$, $\phi_{sl,in} = 51.2\%$) are presented in Figure 4.6. For a single exchanger with the same Ntu and Cr, the sensible and latent effectivenesses for $C_{sl} > C_g$ are larger than that for $C_{sl} < C_g$.

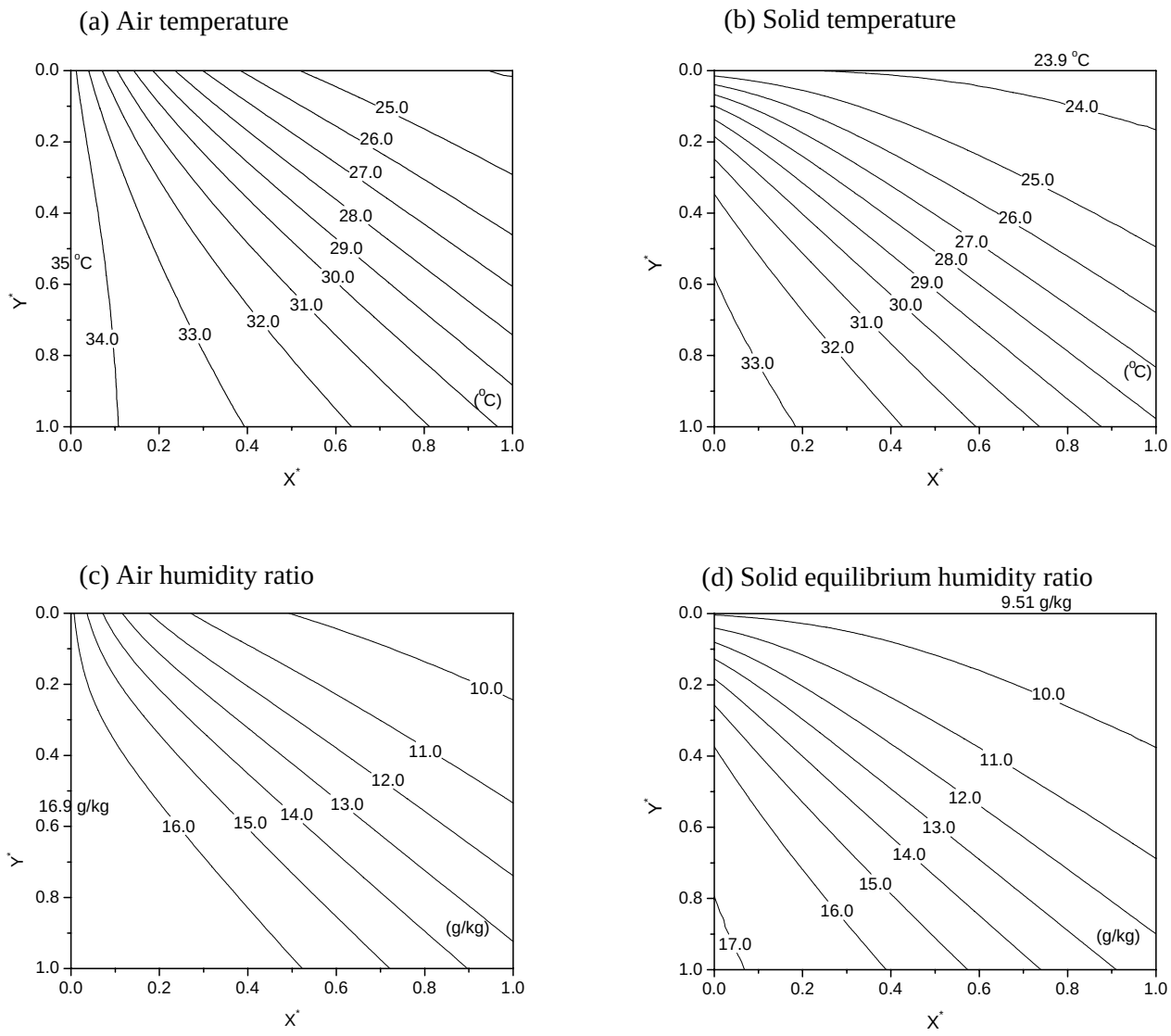

Figure 4.5 Distributions of (a) air temperature, (b) solid temperature, (c) air humidity ratio, and (d) solid equilibrium humidity ratio for operating condition $T_{g,in} = 35\ ^{\circ}C$, $\phi_{g,in} = 47.4\%$, $T_{sl,in} = 23.9\ ^{\circ}C$, $\phi_{sl,in} = 51.2\%$ with Ntu = 6 and Cr = 0.3 ($C_{sl} > C_g$).

In Figure 4.6(a), the sensible effectiveness ε_s is minimum when the heat capacity ratio Cr = 1. As Cr decreases (i.e., C_{sl}/C_g increases for C_{sl}/C_g >1 and C_{sl}/C_g decreases for C_{sl}/C_g <1), ε_s increases. This result is similar to that for sensible heat exchangers

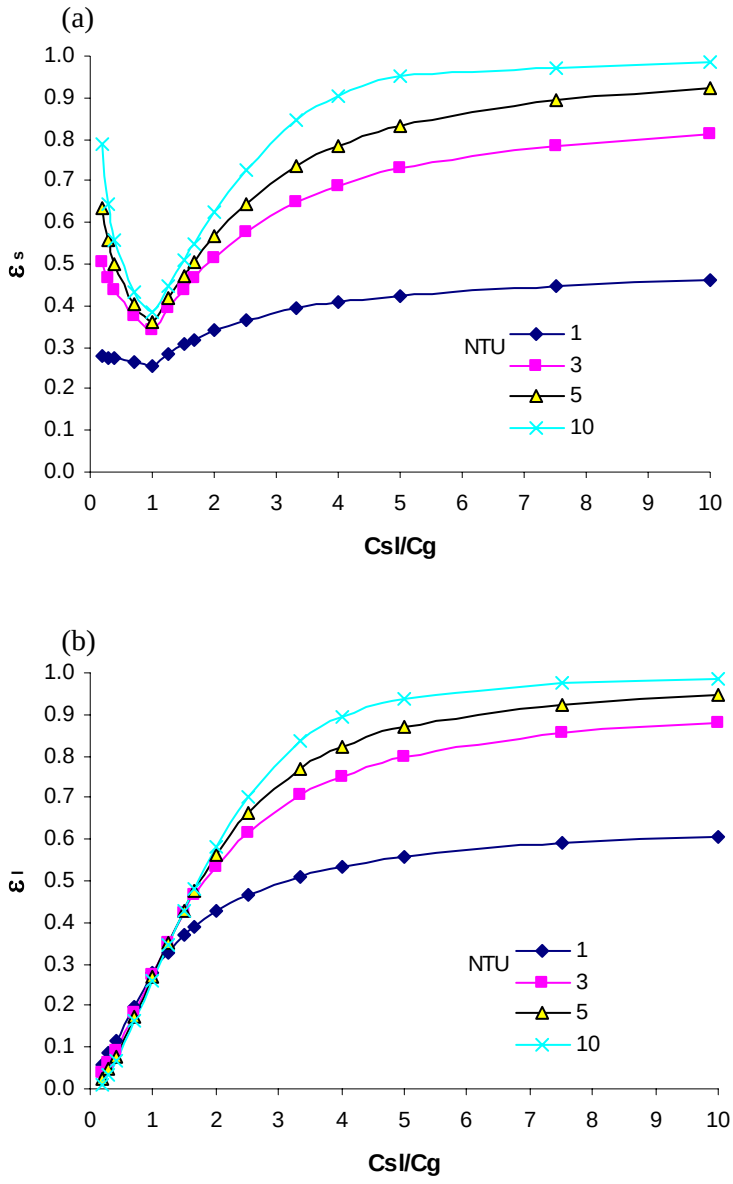

Figure 4.6 Effectiveness of (a) sensible and (b) latent energy transfer versus solid/gas capacity ratio for a single exchanger with ARI summer operating conditions.

(Figure 3.1). In Figure 4.6(b), the latent effectiveness increases with the increase of C_{sl}/C_g from zero because the moisture transfer goes to zero as $C_{sl} \to 0$. These effectiveness graphs will be different for different operating conditions, when the heat and moisture transfer direction and magnitude change significantly. These results are very similar with those of Fan et al. (2006) for a liquid desiccant and air exchanger.

4.4 Run-around System with Heat Transfer and Moisture Transfer

The run-around heat and moisture recovery system has separate exchangers in the supply and exhaust air streams. The scheme for the run-around system is shown in Figure 2.1. ARI summer and winter test conditions (ARI, 2005) shown in Table 4.3 are used for the simulation where each exchanger has the properties listed in Table 4.1.

Table 4.3 ARI 1060 (2005) test inlet air conditions for certifying energy exchangers

Summer	Inlet temperature of the supply air stream	35 $^{\circ}C$
	Inlet relative humidity of the supply air stream	47.4%
	Inlet temperature of the exhaust air stream	23.9 $^{\circ}C$
	Inlet relative humidity of the exhaust air stream	51.2%
Winter	Inlet temperature of the supply air stream	1.7 $^{\circ}C$
	Inlet relative humidity of the supply air stream	82.5%
	Inlet temperature of the exhaust air stream	21.1 $^{\circ}C$
	Inlet relative humidity of the exhaust air stream	49.2%

Figure 4.7 shows the sensible, latent, and total effectivenesses of the run-around system with Ntu as a parameter during ARI summer operating conditions. For $Ntu \geq 5.0$, the peak sensible, latent, and total effectivenesses occur when the heat capacity ratio Cr = 0.3 ($C_{sl} / C_g = 3.3$). That is, the heat capacity rate of the solid is about 3.3 times larger than the moist air. For $Ntu < 5.0$, these effectivenesses are somewhat insensitive to C_{sl} / C_g for $C_{sl} / C_g > 3.0$. These results are very close to Fan et al. (2006), and the sensible effectiveness is almost the same especially. This comparison can further verify the model with moisture and heat transfer.

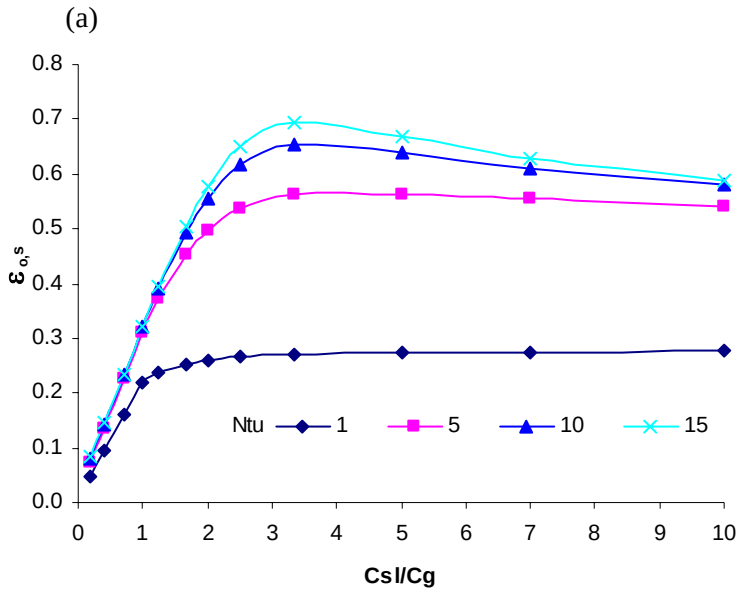

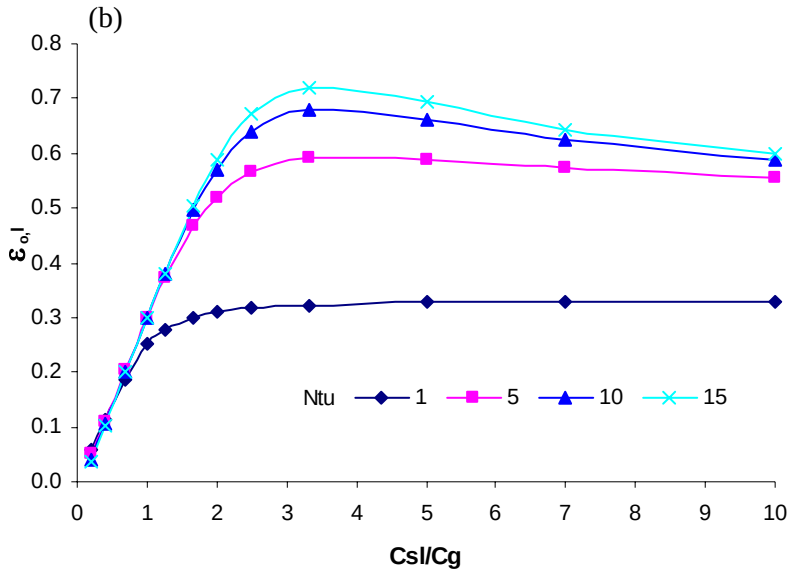

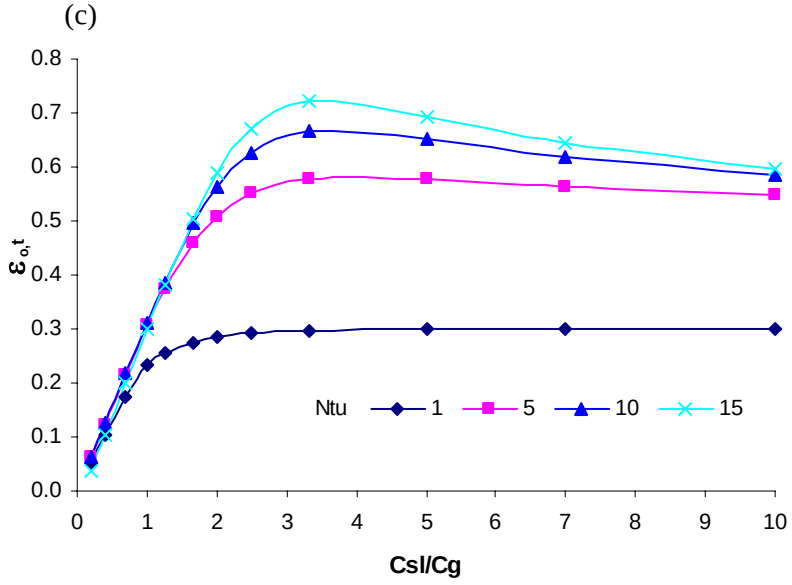

Figure 4.7 The (a) sensible, (b) latent, and (c) total effectivenesses of the run-around system for different values of Ntu using ARI summer test conditions.

Figure 4.8 shows the sensible, latent, and total effectivenesses of the run-around system with Ntu as a parameter during ARI winter operating condition. For this winter

condition and $Ntu \geq 5.0$, the peak sensible, latent, and total effectiveness occur when the heat capacity ratio Cr = 0.5 ($C_{sl} / C_g = 2$); i.e., the heat capacity rate of the solid is about twice that of the moist air.

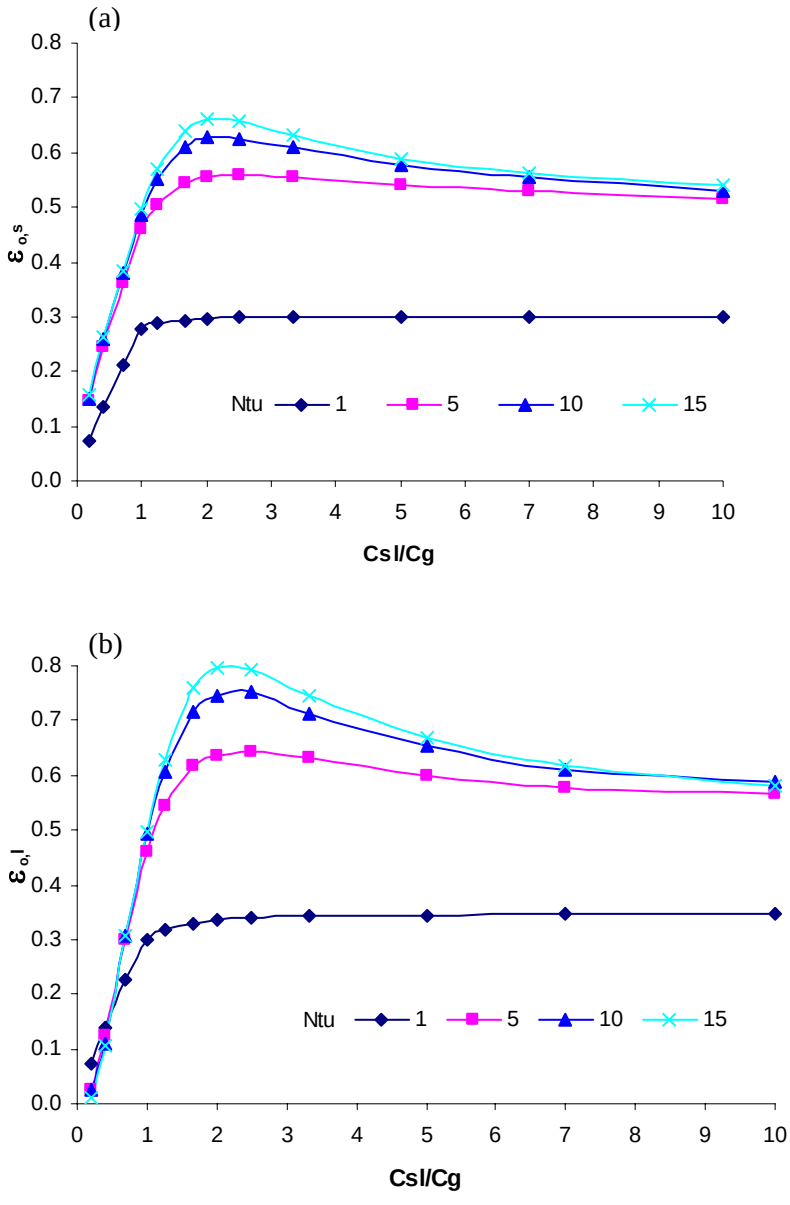

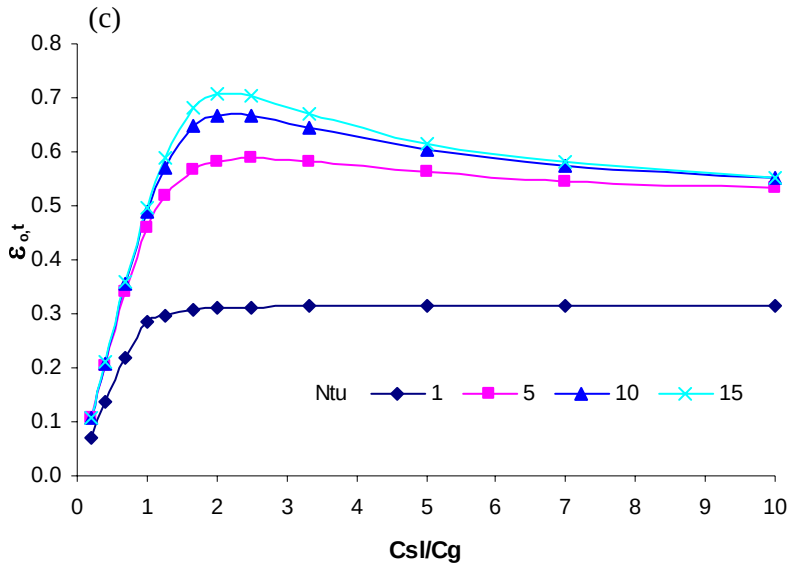

Figure 4.8 The (a) sensible, (b) latent, and (c) total effectivenesses of the run-around system for different values of Ntu using ARI winter test conditions.

For the run-around system with only heat transfer, and using dry air with the same operating temperature as in summer ARI operating condition, the results were illustrated in Figure 4.1. The peak values occur when Cr = 1.0 ($C_s / C_g = 1$); i.e., the heat capacity rate of the solid is equal to the heat capacity rate of the dry air. These results show that for $Ntu \geq 5.0$, the maximum effectivenesses in the run-around system will occur at a heat capacity ratio, which depends on the operating condition.

Figure 4.9 compares the sensible, latent and total effectiveness of the run-around system versus C_{sl} / C_g for Ntu = 10 during ARI summer and winter operating conditions. This figure shows that the sensible, latent, and total effectiveness are nearly the same during the ARI summer test condition, but are significantly different during the ARI winter condition. For all cases, the total effectiveness lies between the sensible and latent effectiveness.

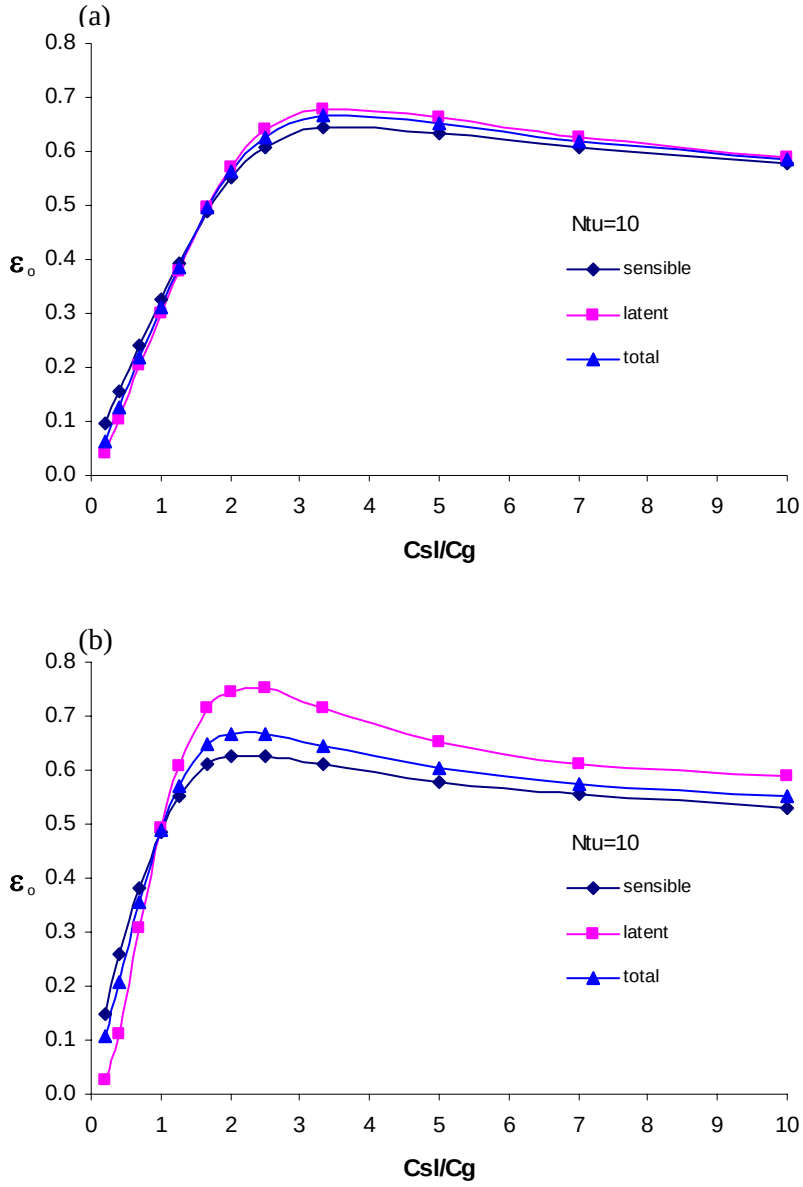

Figure 4.9 The effectivenesses of the run-around system versus C_{sl}/C_g for Ntu = 10 during ARI (a) summer and (b) winter operating conditions.

Figure 4.10 shows the air inlet and bulk outlet conditions for the supply air and exhaust air exchangers on a psychrometric chart for ARI summer and winter conditions at the optimal Cr value. It is found that there are more moisture transfer and less sensible heat

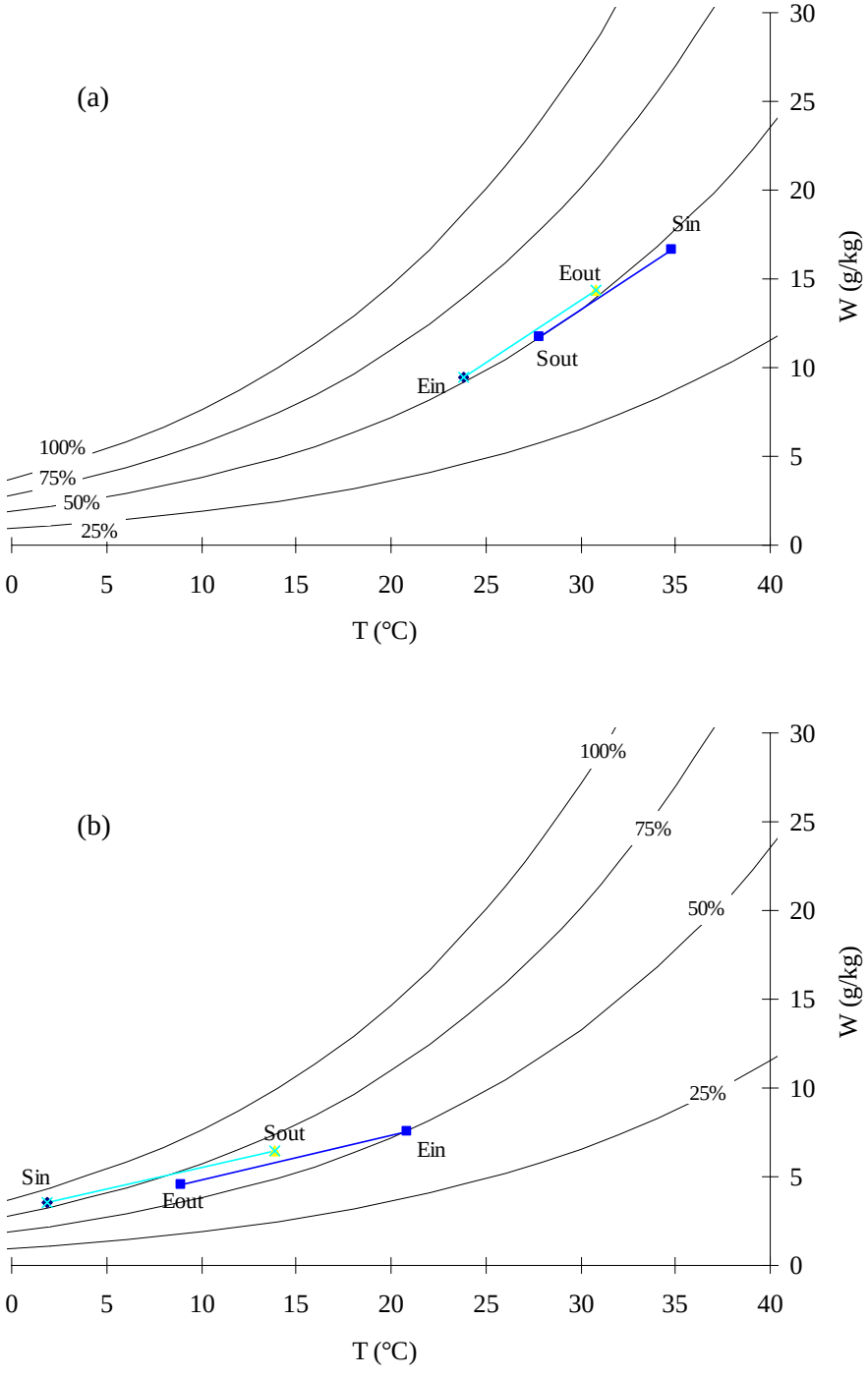

Figure 4.10 Supply air and exhaust air exchanger processes superimposed on a psychrometric chart when Ntu = 10 and (a) Cr = 0.3 ($C_{sl} / C_g = 3.3$) during ARI summer test conditions, and (b) Cr = 0.5 ($C_{sl} / C_g = 2$) during ARI winter test conditions.

transfer inside each exchanger in summer condition, and there are less moisture transfer and more sensible heat transfer inside each exchanger in winter condition.

4.5 The Thickness of Coating

In order to investigate the influence of the desiccant coating thickness on the effectiveness of the run-around system, the outside diameter of the desiccant coating (D) is 30.6 μm based on the solid volume fraction listed in Table 1. It is held constant to keep the specific surface area of the porous solid constant. Meanwhile, the diameter of the fibre glass (d) is allowed to change from 10 μm to 30.6 μm. This range of d gives a range of desiccant coating thickness from 10.3 μm to nearly 0 μm.

Figure 4.11 shows the moisture transfer rate, moisture content of the desiccant in the supply side inlet and outlet, and effectivenesses versus fibre diameter with Ntu=10 and Cr=0.3 ($C_{sl} / C_g = 3.3$) for ARI summer test conditions. Figure 4.12 presents the same variables for ARI winter test conditions with Ntu = 10 and Cr = 0.5 ($C_{sl} / C_g = 2$).

These simulations show that the moisture transfer rate between air and solid desiccant is almost constant as the fibre diameter increases from 10 μm to about 28 μm (or as the desiccant coating thickness decreases from 10.3 μm to 1.3 μm). As d increases above about 28 μm, the moisture transfer rate decreases rapidly as d approaches D = 30.6 μm.

(a)

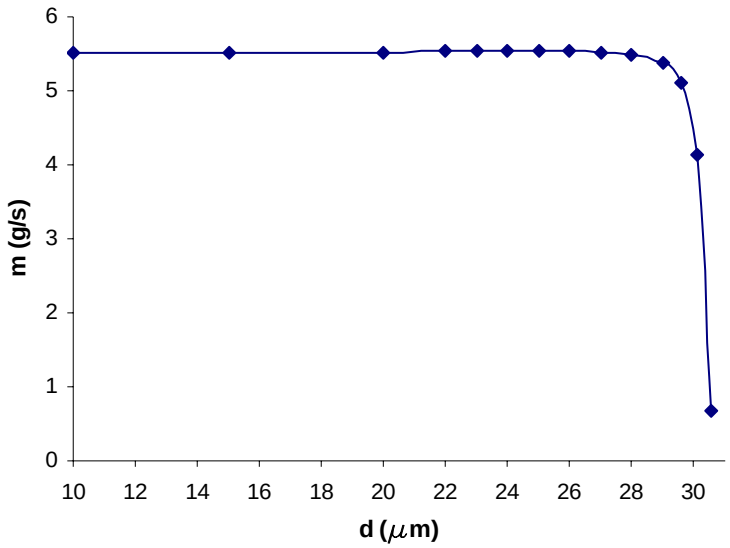
m (g/s)
0
1
2
3
4
5
6
10
12
14
16
18
20
22
24
26
28
30
d (μm)

(b)

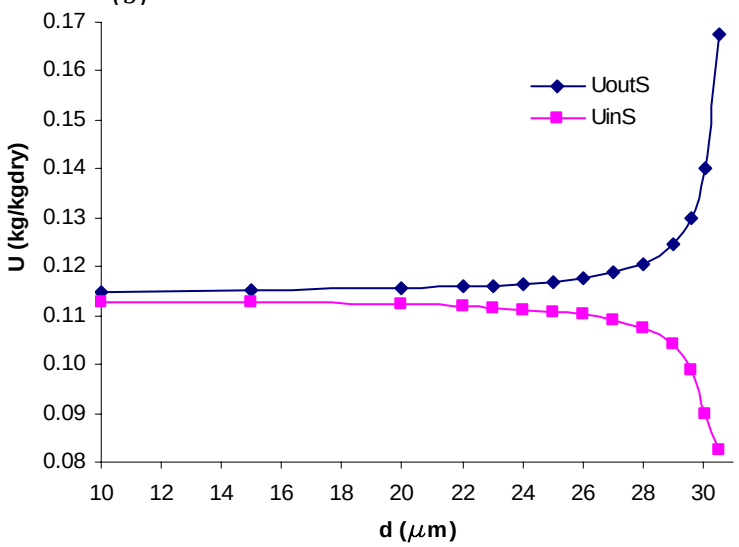
U (kg/kgdry)
0.08
0.09
0.10
0.11
0.12
0.13
0.14
0.15
0.16
0.17
10
12
14
16
18
20
22
24
26
28
30
d (μm)
UoutS
UinS

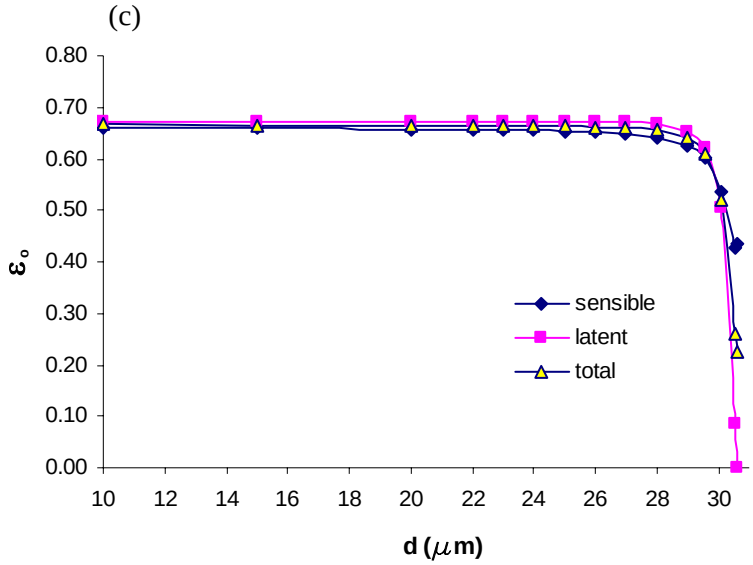

Figure 4.11 The (a) moisture transfer rate, (b) moisture content in supply side inlet and outlet, and (c) effectivenesses versus fibre diameter with Ntu = 10 and Cr = 0.3 ($C_{sl}/C_g = 3.3$) at ARI summer operating conditions.

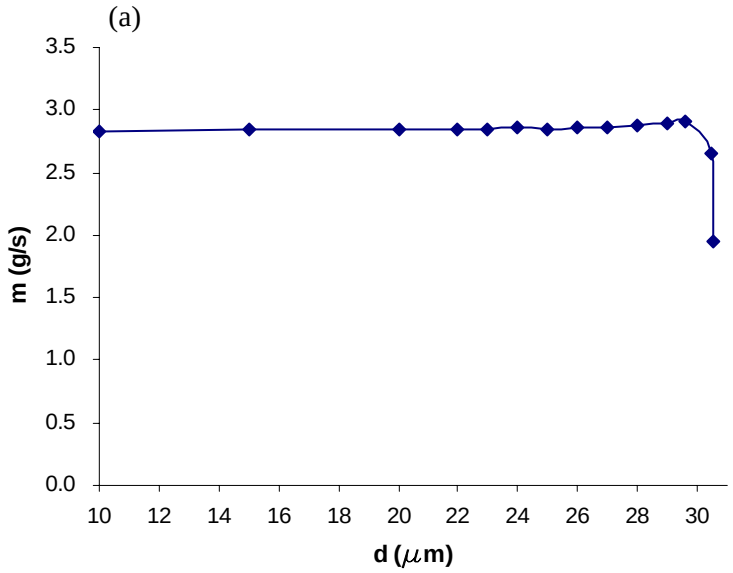

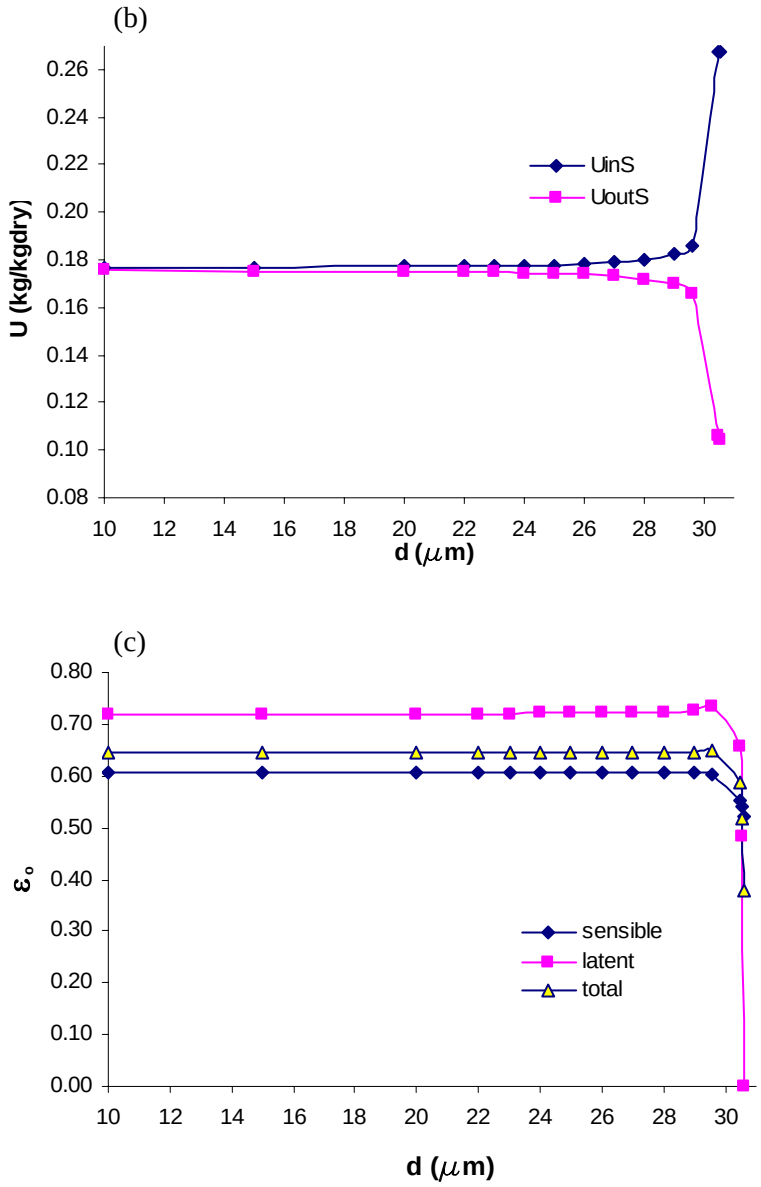

Figure 4.12 The (a) moisture transfer rate, (b) moisture content of the desiccant in supply side inlet and outlet, and (c) effectivenesses versus fibre diameter with Ntu = 10 and Cr = 0.5 ($C_{sl}/C_g = 2$) at ARI winter operating conditions.

Figure 4.11(b) shows that the difference between the solid moisture content in supply side inlet and outlet increases as d increases (or the thickness of the desiccant coating decreases). This is logical because there is less desiccant to store the moisture as d increases and therefore the moisture content of the desiccant changes more as it flows

through the energy exchanger. Here the increased difference between the moisture content of the desiccant in the inlet and outlet can keep the moisture transfer rate nearly constant as d increases, but when d is larger than about 28 μm, the desiccant is too thin to maintain the constant moisture transfer rate, and the moisture transfer rate decreases to a very small value (Figure 4.11(a)). Figure 4.11(c) shows that the sensible, latent, and total effectivenesses are almost constant from d = 10 μm to about d = 28 μm, and decrease rapidly after d = 28 μm. In this case, if the coating thickness of the desiccant is larger than 1 or 2 μm, the run-around system has almost the same performance no matter how thick the desiccant coating is.

Similar results were obtained for the ARI winter test condition, and the only major difference between the summer and winter test conditions is that the critical thickness of the desiccant coating is smaller during winter operating conditions because the moisture transfer rate is smaller due to the dryer air conditions. For silica gel particles with a diameter of about 0.5 to 5 μm, if the fibre glass is covered by this desiccant completely, the thickness of coating should be thick enough for the moisture transfer in the run-around system.

Chapter 5

SENSITIVITY STUDIES

5.1 Introduction

The purpose of the sensitivity study is to investigate how the effectiveness will change with changes in Ntu, air velocity, silica gel fraction, and porous moving balls. These results can demonstrate how the performance of this solid desiccant run-around system will change during its practical use.

5.2 Ntu

It was shown previously that for each specific Ntu value, the effectiveness will be close to a maximum when Cr = 0.3 ($C_{sl}/C_g = 3.3$) during ARI summer conditions, and when Cr = 0.5 ($C_{sl}/C_g = 2$) during ARI winter conditions. Figure 5.1 shows the peak effectivenesses of the run-around system versus Ntu with heat capacity ratio Cr = 0.3 ($C_{sl}/C_g = 3.3$) for the ARI summer test condition, and heat capacity ratio Cr = 0.5 ($C_{sl}/C_g = 2$) for the ARI winter test condition. Although the sensible and latent effectiveness are different during the summer and winter ARI operating conditions (for the same Ntu), the total effectiveness is almost the same in both the summer and winter conditions when the Ntu is the same.

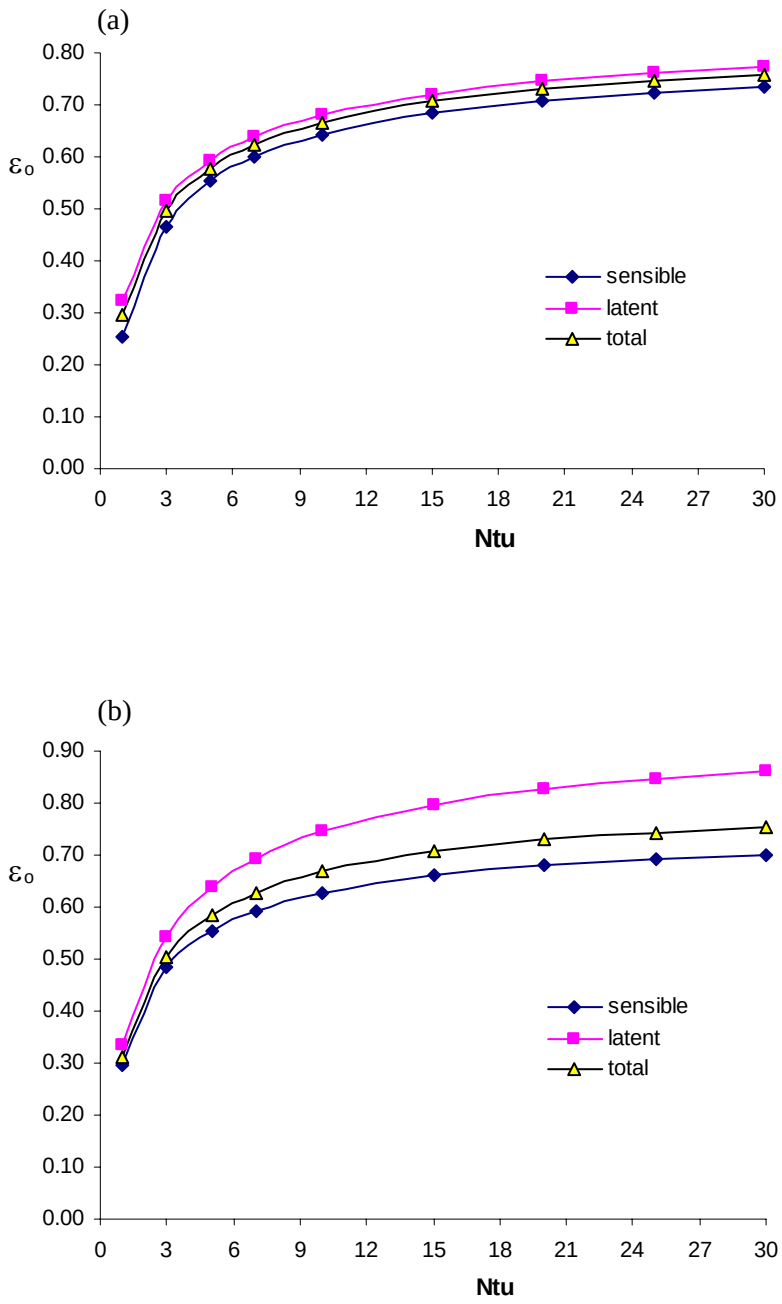

Figure 5.1 Peak effectivenesses of the run-around system versus Ntu with (a) Cr = 0.3 ($C_{sl}/C_g = 3.3$) for ARI summer test conditions, and (b) Cr = 0.5 ($C_{sl}/C_g = 2$) for ARI winter test conditions.

For a specific Ntu, the peak effectiveness values can be found from the Figure 5.1 for summer and winter ARI test conditions respectively. In order to achieve a high

effectiveness, the Ntu should be high. For example, when Ntu = 15, the total effectiveness from Figure 5.1 is about 70% for both summer and winter test conditions. This high value of Ntu can be obtained easily because of the large surface area inside the moving solid particle bed. For the $0.3\,m \times 0.3\,m \times 0.3\,m$ exchanger used in this thesis with a solid (glass fibre + silica gel) volume fraction of 0.6% (Table 4.1), a Ntu of 15 corresponds to a face velocity of about 4m/s (800 fpm), and Ntu increases with the face velocity's decrease.

5.3 Air Velocity and Silica Gel Fraction

5.3.1 Effectiveness

Figure 5.2 shows the effectiveness versus air face velocity, which is the average air velocity before entering the heat exchanger, and the silica gel fraction for summer ARI conditions and Cr = 0.3 ($C_{sl} / C_g = 3.3$). When the air velocity increases from 0.6 m/s (120 fpm) to 2 m/s (400 fpm), Ntu decreases from 35 to 20 approximately. The effectiveness decreases marginally with increasing face velocity for the range investigated.

For a constant air face velocity of u = 1 m/s, Figure 5.2 (b) shows that when the silica gel fraction (ε_{si}) increases from 0.1% to 0.65%, the effectiveness increases. This is

logical because increasing ε_{si} increases the surface area for heat and moisture transfer in the porous bed, which increases Ntu from around 10 to 35 as ε_{si} increases from 0.1% to

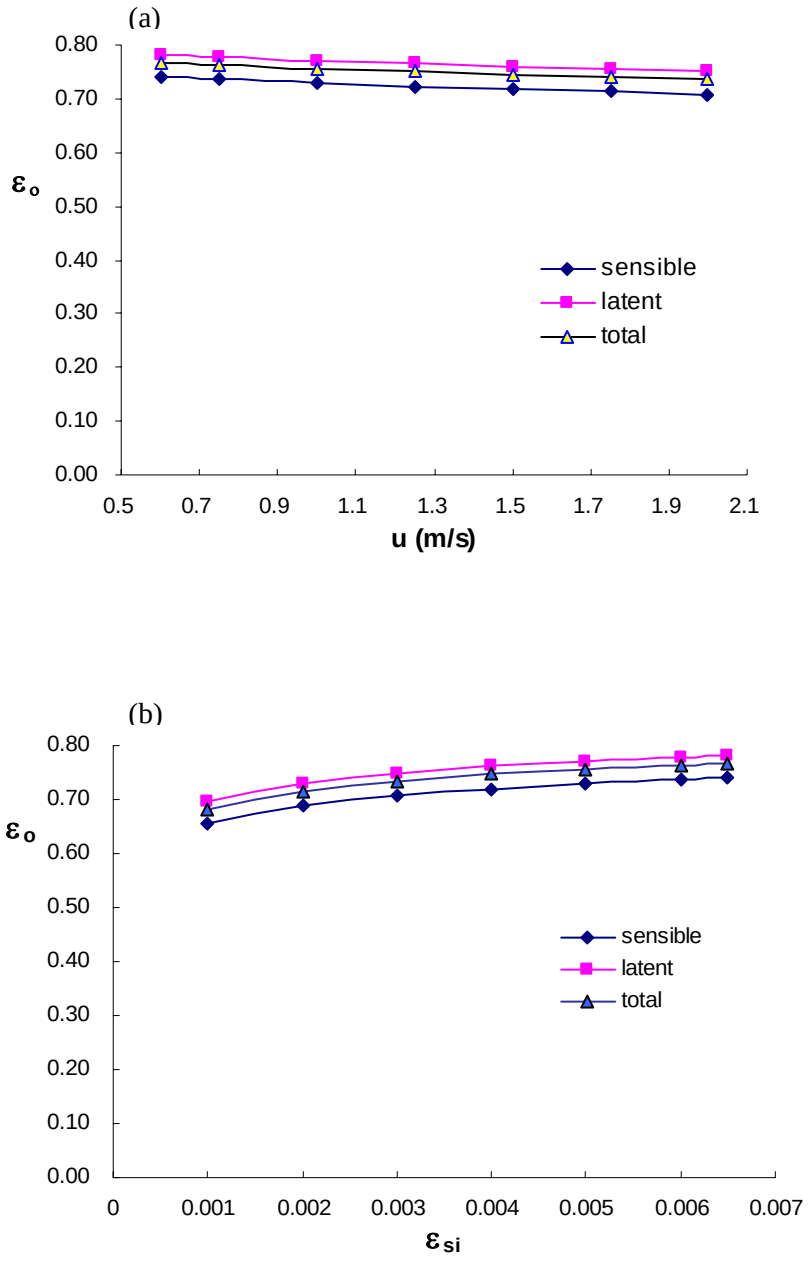

Figure 5.2 Effectiveness for the ARI summer test condition and Cr = 0.3 ($C_{sl}/C_g = 3.3$) when (a) $\varepsilon_f = 0.1\%$ and $\varepsilon_{si} = 0.5\%$ with variable air face velocities, and (b) u = 1 m/s and $\varepsilon_f = 0.1\%$ with variable silica gel fractions.

0.65%. This trend in effectiveness can also be found in Figure 5.1 (a) when Ntu is increased.

5.3.2 Air Pressure Drop

In HVAC systems, the ventilation air usually enters into an air handling unit by using the same fan as the return air, and they have almost the same duct friction resistance, so the pressure drop through the exchanger needs to be controlled to make the pressure drop in the fresh air system equal to that in return air system under the design ventilation air flow rate; otherwise, the fresh air will not be sufficient to satisfy the occupants. In the exhaust exchanger side, the less pressure drop through the exchanger, the less exhaust fan power needed to overcome the friction resistance in the exhaust air system. The air pressure drop through the exchanger should be less than about 250 Pa (1 inch of water column) to be acceptable in most HVAC designs.

The air flow pressure drop through the exchanger porous bed can be calculated by the Ergun correlation (Ergun, 1952):

$$\frac{dp}{dx} = -150 \cdot \mu \cdot \frac{(1-\varepsilon)^2}{\varepsilon^3} \cdot \frac{u}{d^2} - 1.75 \cdot \frac{1-\varepsilon}{\varepsilon^3} \cdot \frac{\rho \cdot u^2}{d} \tag{5.1}$$

Where, ε is the porosity of the porous media or volume fraction of the air outside the desiccant coating (not including the void space inside desiccant), d is the outside diameter of the fibre coating, u is air face velocity, ρ is air density, and μ is air viscosity.

Figure 5.3 shows the pressure drop across a porous bed with a depth of 300 mm (X_0 = 300 mm) at different air face velocities. The volume fractions of fibre and silica gel are the same as for previous simulations, and assume the diameter of the fibre is 10 μm. In

different HVAC systems, the air face velocity should be chosen carefully to optimize the exchanger's size.

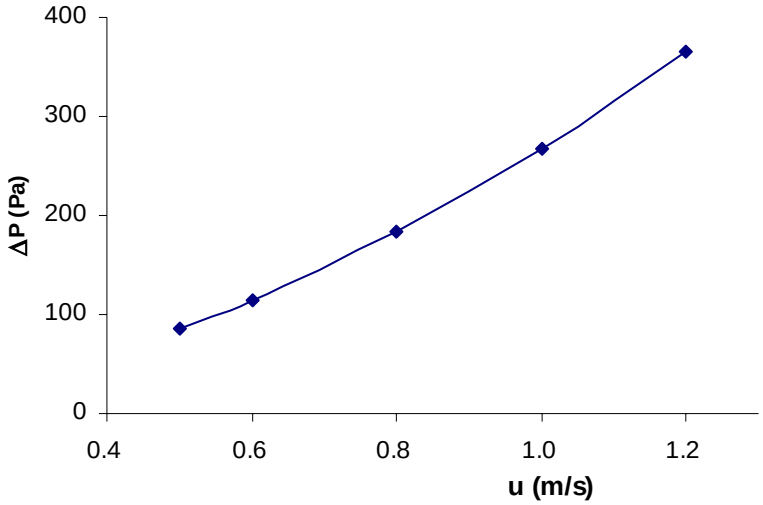

Figure 5.3 The air pressure drop through porous bed (X_0 = 300 mm) versus air face velocity.

In order to keep a reasonable air pressure drop (< 250 Pa) and optimize the exchanger size for this specific solid volume fraction and depth, the air face velocity is about 0.95 m/s (190 fpm) with 250 Pa air pressure drop. Ntu is about 30 when the air face velocity is about 0.95 m/s (190 fpm), which indicates (from Figure 5.1) that the total effectiveness is about 76% for both summer and winter test conditions.

If the depth X_0 = 150 mm, the face velocity is about 1.45 m/s (290 fpm) with 250 Pa pressure drop, and if X_0 = 100mm, it is about 1.8 m/s (360 fpm). The exchanger face area can be calculated based on the air velocity and air flow rate. For different solid volume fraction and depth, the air face velocity will be chosen differently in HVAC systems design.

5.4 Moving Porous Balls

In order to let the porous bed move without mechanical damage to the coating, the fiber and silica gel coating could be transported in highly porous balls or cages. A schematic of each ball is shown in Figure 5.4. For this to work in a practical application, the shell or cage of each ball must have a very low flow resistance compared to that of the internal coated fiber material.

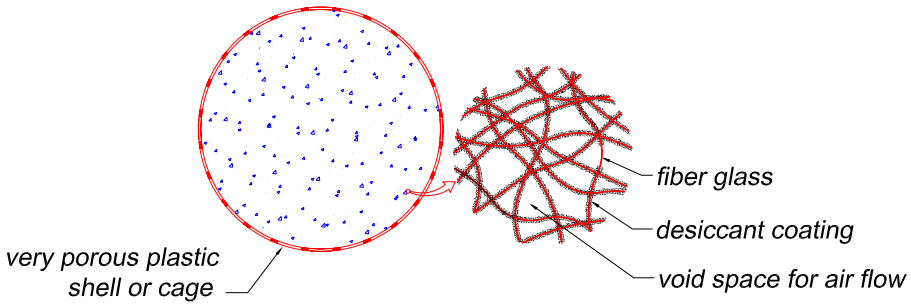

Figure 5.4 The structure of a porous ball with desiccant coated fibre glass.

In general, the air flow through porous balls will be very complicated, with a flow velocity inside each ball that is not uniform. In the moving porous bed, the differential control volume is Δx , Δy , but in the moving porous balls, the differential control volume is a ball with diameter d.

In this design, the balls will enter the exchanger from above and move steadily through each exchanger along tilted guide rods. As the balls move through the exchanger, heat and moisture will be transferred between the air and solid desiccant inside each ball. After passing through the supply side exchanger, the balls will leave the exchanger and

be mechanically conveyed to the exhaust exchanger where the desiccant coated fibers within the balls will be regenerated.

In the model presented in Chapter 2 of this thesis, it is assumed that all of the air that flows through the energy exchanger exchanges heat and moisture with the porous moving bed; however, when the porous material is contained in a spherical shell or ball, some of the air will bypass the porous material. As the fraction of air that bypasses the ball increases, the total heat and moisture transfer rates (and effectiveness values) will decrease because only the air that passes through the ball will exchange heat and moisture with the desiccant coated glass fiber. In order to estimate this effect, it is assumed that the fraction of the air flowing through each ball ($f_{in,ball}$) and the air passing around each ball ($f_{out,ball}$) uniformly mix after each ball (Figure 5.5). In addition, it is assumed that the air temperature and vapour density as well as the solid temperature and moisture content inside each ball are uniform because each ball is small compared to the entire exchanger and the balls rotate as they move through the exchanger.

The temperature and density of the air, after mixing the air that flows through the ball and the air that bypasses the ball, can be calculated from energy and mass balances. Assuming that both air streams have the same density and specific heat capacity, the mixed air temperature can be calculated as follow:

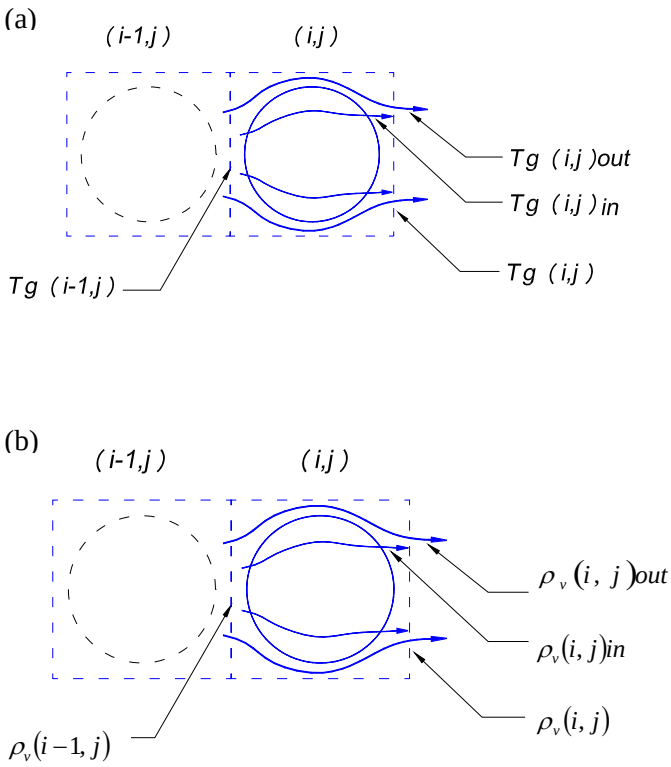

Figure 5.5 Air flow streams through and around the porous ball, (a) temperature and (b) vapour density.

$$f_{in,ball} + f_{out,ball} = 1 \tag{5.1}$$

$$Q_{out} = u_g d^2 f_{out,ball} \tag{5.2}$$

$$Q_{in} = u_g d^2 f_{in,ball} \tag{5.3}$$

$$Q = Q_{out} + Q_{in} \tag{5.4}$$

$$T_g(i,j)_{out} = T_g(i-1,j) \tag{5.5}$$

$$T_g(i,j) = \frac{T_g(i,j)_{out} Q_{out} + T_g(i,j)_{in} Q_{in}}{Q} \tag{5.6}$$

The indices (i, j) represents the position of each ball, for example, (1, 1) represents the ball in first row and the first column, Q_{out} is the air flow rate outside of the ball (or the flow that bypasses the ball) , Q_{in} is the air flow rate through the ball, Q is the total air flow rate, $T_g(i,j)_{out}$ is the air temperature outside of the ball, $T_g(i-1,j)$ is the air temperature before entering the ball (i, j), $T_g(i,j)_{in}$ is the average temperature of the air in the ball, and $T_g(i,j)$ is the air temperature after mixing the air streams that flow inside and outside of the ball. $T_g(i,j)_{in}$ can be calculated using the same method described in Chapter 2 (i.e., assuming that all the air flowing through the exchanger exchanges heat and moisture with the desiccant coated fibre or $f_{in,ball}$ =1). The vapor density of the mixed air streams can be calculated with:

$$\rho_v(i,j)_{out} = \rho_v(i-1,j) \tag{5.7}$$

$$\rho_v(i,j) = \frac{\rho_v(i,j)_{out} Q_{out} + \rho_v(i,j)_{in} Q_{in}}{Q} \tag{5.8}$$

Where, $\rho_v(i,j)_{out}$ is the vapour density of the air that bypasses the ball, $\rho_v(i-1,j)$ is the vapour density before entering the ball (i, j), $\rho_v(i,j)_{in}$ is the vapor density inside the ball, and $\rho_v(i,j)$ is the vapor density after mixing the air streams that flow inside and

outside of the ball. Similarly as with $T_g(i, j)$, $\rho_v(i, j)_{in}$ can be calculated using the same method described in Chapter 2 of this thesis.

It would be very difficult to correctly estimate the fraction of the air that flows through each ball ($f_{in,ball}$) and its pressure drop theoretically. In order to investigate how $f_{in,ball}$ influences the effectiveness, Figure 5.6 shows moving $m \times n$ balls for summer ARI conditions, Cr = 0.3 ($C_{sl} / C_g = 3.3$), and an air face velocity of u = 1 m/s (200fpm) where m is the number of balls in air flow direction (x), and n is the number of balls in the direction of the ball movement (y) inside the exchanger. The size of the exchanger changes as m increases. For example, the exchanger is twice as long in the flow direction when m = 60 than when m = 30. It should be noted that the maximum value of $f_{in,ball}$ in Figure 5.6 is $f_{in,ball} = S_{circle} / S_{square} = \pi / 4 = 0.785$, which is an area averaged maximum and corresponds to the situation where a uniform velocity approaches the ball and the air that flows through the ball and bypasses the ball is unaffected by the permeability of the porous material within the ball. As the permeability of the porous material within the ball decreases, more air will by pass the ball and $f_{in,ball}$ will decrease.

The overall effectiveness does not have significant change with the increase of $f_{in,ball}$ in the range from 0.4 to 0.785 for every specific m number. After flowing through or around the porous ball, the two parts of air mix together, and this can increase the temperature and vapor density difference between the air and solid material in the next

ball, which can increase heat and moisture transfer. As a result, $f_{in,ball}$ has a slightly smaller effect for an exchanger that has longer air flow path (i.e., a larger value of m) than one with a smaller air flow path (i.e., a lower value of m). For a large value of $f_{in,ball}$, the overall effectiveness is not very sensitive to $f_{in,ball}$. In future work, $f_{in,ball}$ should be obtained by experimental testing.

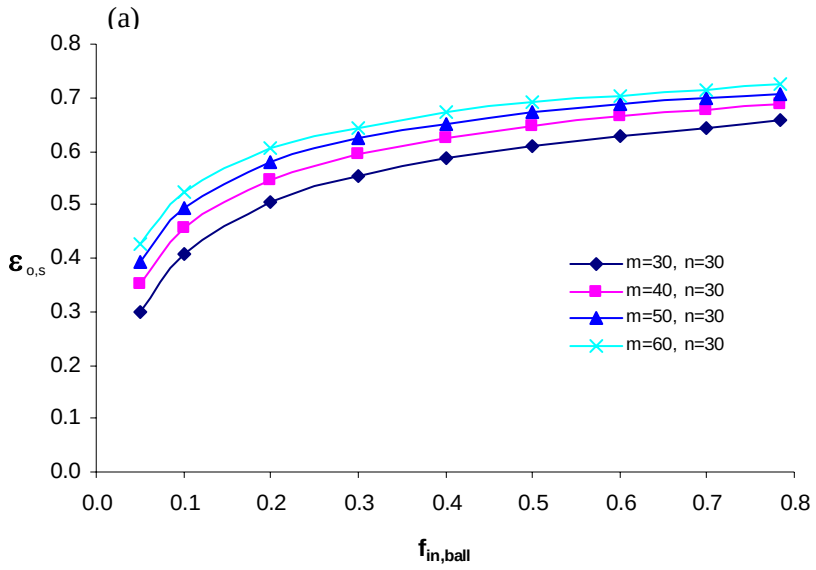

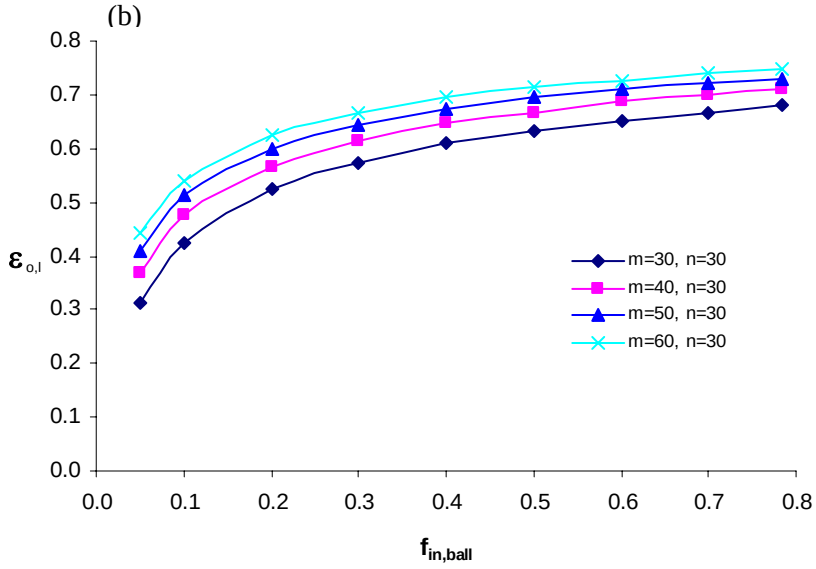

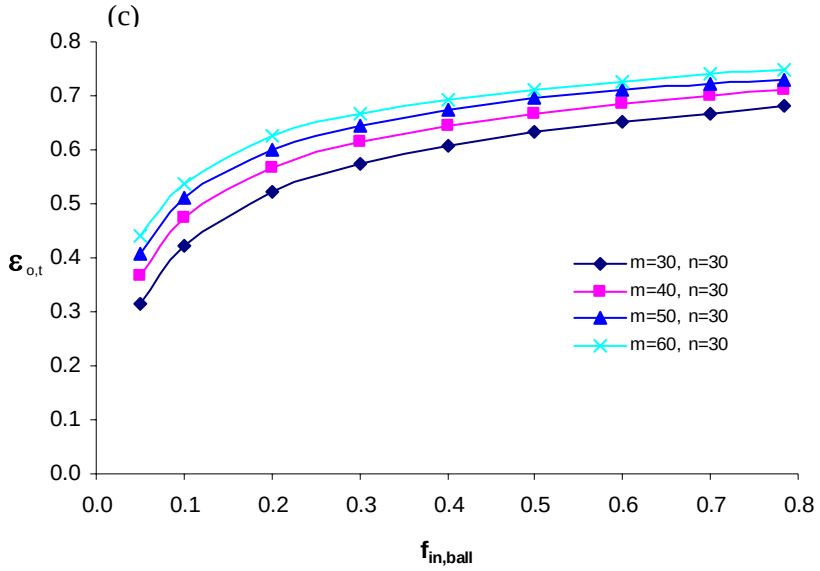

Figure 5.6 The (a) sensible, (b) latent, and (c) total effectivenesses versus the flow fraction of the supply and exhaust air that pass through each ball ($f_{in,ball}$) for summer ARI conditions, Cr = 0.3 ($C_{sl} / C_g = 3.3$), and an air face velocity of 1 m/s.

For a specific $f_{in,ball}$, the larger the m (or the larger the air flow path in each exchanger), the higher the effectivenesses, and the larger the air pressure drop through the moving ball system. In practical applications, an optimized design may be reached by trading off changes in the effectiveness and air pressure drop.

Figure 5.7 shows the effectivenesses with 1800 balls number ($m \times n = 60 \times 30$), Cr = 0.3 ($C_{sl} / C_g = 3.3$), ARI summer test conditions and $f_{in,ball} = 0.6$ for different value of Ntu, and Figure 5.8 shows Cr = 0.5 ($C_{sl} / C_g = 2$) in ARI winter test conditions. The results in both figures are very similar to those in Figure 5.1 (a) and (b), indicating that the effectiveness for the moving porous ball system can be predicted by Figure 5.1 after calculating Ntu.

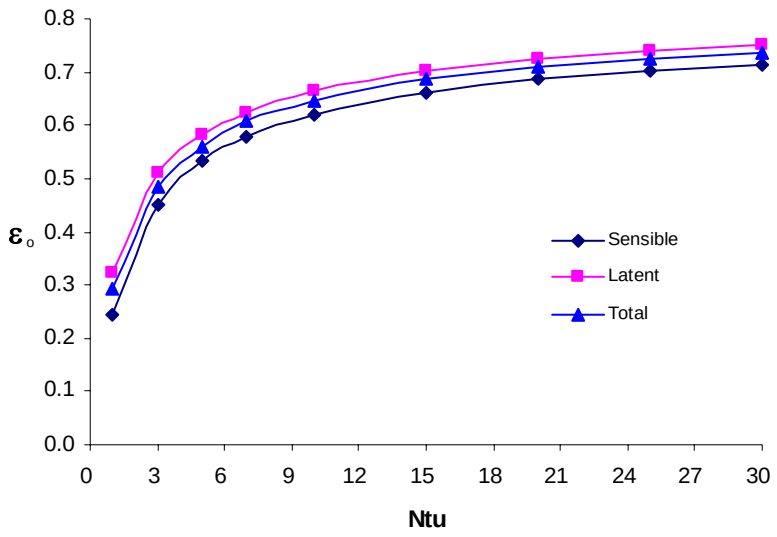

Figure 5.7 Effectiveness versus Ntu for m = 60 and n = 30, Cr = 0.3 ($C_{sl}/C_g = 3.3$), ARI summer test conditions and $f_{in,ball} = 0.6$.

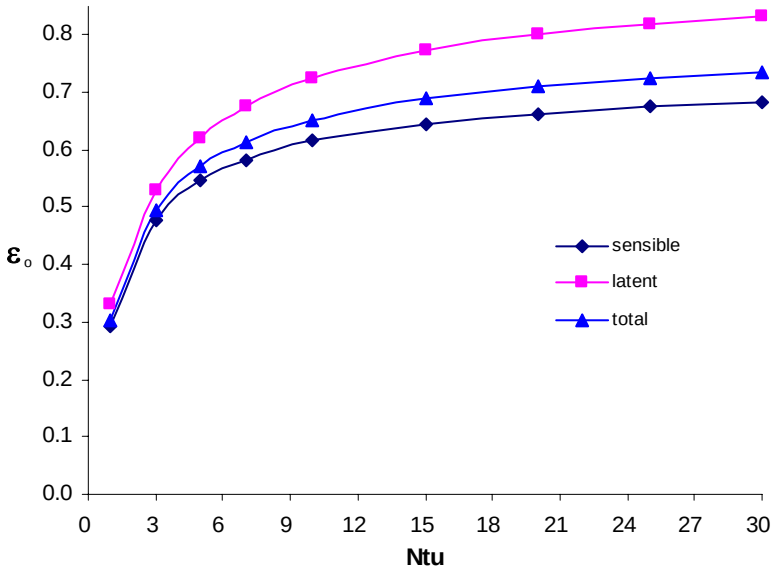

Figure 5.8 Effectiveness versus Ntu for m = 60 and n = 30, Cr = 0.5 ($C_{sl}/C_g = 2$), ARI winter test conditions and $f_{in,ball} = 0.6$.

Chapter 6

SUMMARY, CONCLUSIONS AND FUTURE WORK

6.1 Summary

This thesis presents a heat and moisture transfer model for air-to-solid desiccant energy exchangers and a run-around system. To verify the accuracy of the model, numerical results for heat and moisture transfer are compared with available correlations in the literature.

By using the model, the peak effectiveness was investigated in the run-around system under ARI summer and winter test conditions, and the temperature and moisture distribution inside each exchanger were illustrated. The thickness of the desiccant coating was studied by assuming that the outside diameter of the desiccant coated fibre is constant, while the thickness of the desiccant and the diameter of the glass fibre change.

In the sensitivity study, the sensitivity of Ntu, air velocity, silica gel fraction, and porous moving balls were studied in order to obtain information for practical applications.

6.2 Conclusions

1. Although the main heat transfer is caused by convection between air flow and the internal surface area of the bed, rather than heat conduction through the plates as in traditional cross-flow flat-plate exchangers, the numerical results are in good agreement with the well-known analytical results for sensible cross-flow heat exchangers. The temperature and moisture content for any specific position inside a single exchanger or the run-around system can be simulated with the model developed in this thesis. The $\varepsilon - Ntu$ graphs were developed under different operating conditions.

2. This thesis presents numerical heat and moisture transfer predictions of a single exchanger and a run-around system that employ solid-desiccant moving beds. The temperature and humidity ratio distribution inside a single exchanger can be complex. For example in a single exchanger, when the air inlet relative humidity is high and the solid desiccant is relatively dry, the temperature of the air stream leaving the exchanger may be higher than that of the air entering the exchanger, even though the solid desiccant temperature is lower than the inlet air temperature.

3. For the same air flow rate in the supply and exhaust side exchangers, the sensible, latent, and total effectiveness of the run-around system depends on the number of transfer units (Ntu), the heat capacity ratio (Cr or C_{sl} / C_g), and the operating conditions. For the ARI summer test conditions, the maximum effectivenesses of the run-around system occur at a heat capacity ratio of approximately 0.3 ($C_{sl} / C_g \approx 3.3$). For the ARI

winter test conditions, the maximum effectivenesses of the run-around system occur at Cr $\approx$ 0.5 ($C_{sl}/C_g \approx 2$). This result differs from that for dry air with only sensible energy changes, where the maximum effectiveness of the run-around system occurs at Cr $\approx$ 1.

4. In order to get a high overall effectiveness, Ntu should be large and Cr should be chosen for each operating condition, and the volume fraction of the solid material should be selected carefully to get reasonable air and porous bed velocities and pressure drops.

5. For the same Ntu, Cr, and operating conditions, with constant outside diameter of the silica gel coating, the sensible, latent, and total effectivenesses remain nearly constant and independent of the desiccant thickness until the silica gel coating is thinner than 1 or 2 μm.

6. This run-around system can reach a high Ntu very easily because of the high specific surface area compared with flat-plate exchangers. This research was based on run-around system using a moving porous solid bed. The real application is using moving porous solid desiccant balls, and the effectiveness for a system of porous moving balls depends on Ntu, Cr (or C_{sl}/C_g), and operating conditions. The effectiveness was found following the same $\varepsilon - Ntu$ graph with moving porous bed system.

7. The numerical method developed in this thesis is convenient to investigate the effectiveness of the run-around energy recovery system with a wide range of operating conditions and porous bed properties.

6.3 Future Work

1. In this research, a conservative convection coefficient was selected from the literature on porous media. More accurate data could be obtained from experiments.

2. The air pressure drop through the porous ball system and the air fraction flowing through each ball need to be investigated further.

3. The real run-around system with moving porous balls could be constructed based on this research, and then tested in the laboratory. The test results could be compared with the numerical results in this thesis.

REFERENCES

Achenbach, E., 1995. Heat and flow characteristics in packed beds. *Exp. Therm. Fluid Sci.* 10, 17-21.

ARI Standard 1060, 2005. *Rating air-to-air energy recovery equipment*, ARI, Chicago.

ASHRAE, 2004. *HVAC Systems and Equipment Handbook*, ASHRAE, Atlanta.

Bennett, I.J.D., Besant, R.W. and Schoenau, G.J., 1994a. *Validation of a run-around heat recovery system model, ASHRAE* Transactions, 100(1), 230-237.

Bennett, I.J.D., Besant, R.W., Schoenau, G.J. and Johnson, A.B., 1994b. *Procedure for optimizing coils in a run-around heat exchanger system*, ASHRAE Transactions, 100(1), 442-451.

Dullien, F.A.L., 1992. *Porous Media: Fluid Transport and Pore Structure*, Second Edition, Academic Press, New York, NY

Ergun, S., 1952. *Fluid flow through packed columns*, Chemical Engineering Process, 48(2), 89-94.

Fan, H., 2005. *Modeling a run-around heat and moisture recovery system*, MSc. thesis in Mechanical Engineering, University of Saskatchewan.

Fan, H., Simonson, C.J., Besant, R.W. and Shang, W., 2005. *Run-around heat recovery system using cross-flow flat-plate heat exchangers with aqueous ethylene glycol as the coupling fluid*, ASHRAE, Atlanta.

Fan, H., Simonson, C.J., Besant, R.W. and Shang, W., 2006. *Performance of a run-around system for HVAC heat and moisture transfer applications using cross-flow plate exchangers coupled with aqueous lithium bromide*, HVAC&R Research, 12(2), 313-336.

Forsyth, B.I. and Besant, R.W., 1988a. *The design of a run-around heat recovery system*, ASHRAE Transaction, 94(2), 511-531.

Forsyth, B.I. and Besant, R.W., 1988b. *The performance of a run-around heat recovery system using aqueous glycol as a coupling liquid*, ASHRAE Transactions, 94 (2), p532-545.

Gortyshov, Yu, F., Muravev, G.B., and Nadyrov, I.N., 1987. Experimental study of flow and heat exchange in highly porous structures. *Eng.-Phys. J.* 53, 357-361 (in Russian).

Incropera, F.P. and Dewitt, D.P., 1996. *Fundamentals of Heat and Mass Transfer*, 4th ed, John Wiley and Sons, New York, NY

Johnson, A.B., Besant, R.W. and Schoenau, G.J., 1995. *Design of multi-coil run-around heat exchanger systems for ventilation air heating and cooling*, ASHRAE Transaction, 101(2), 967-978.

Kaviany, M., 1991. *Principles of Heat Transfer in Porous Media*, Springer-Verlag, New York, NY

Kays, W.M. and London, A.L., 1984. *Compact Heat Exchanger*, Toronto, ON: McGraw-Hill.

Kokorev, V.I., Subbotin, V.I., Fedoseev, V.N., Kharitonov, V.V., and Voskoboinikov, V.V., 1987. Relationship between hydraulic resistance and heat transfer in porous media. *High Temp.* 25, 82-87.

London, A.L. and Kays, W.M., 1951, *The liquid-coupled indirect-transfer regenerator for gas-turbine plants*, ASME Transactions, 73.

Mason, J.L., 1955. *Proc. Second U.S. Congr. Applied Mechanics*, ASME, 801.

Niu, J.L. and Zhang, L.Z., 2001. *Membrane-based Enthalpy Exchanger: Material considerations and clarification of moisture resistance,* Journal of Membrane Science, 189(2), p 179-191.

Patankar, 1980. *Numerical Heat Transfer and Fluid Flow,* Hemisphere publishing corporation, McGraw-Hill Book Company.

Simonson, C.J., and Besant, R.W., 1997. *Heat and Moisture Transfer in Desiccant Coated Rotary Energy Exchangers: Part I – Numerical Model,* HVAC&R Research, 3(4), 325-350.

Simonson, C.J. and Besant, R.W., 1999a. Energy wheel effectiveness. Part I - Development of dimensionless groups, Int. J. *Heat Mass Transfer,* 42(12), 2161-2170.

Simonson, C.J. and Besant, R.W., 1999b. Energy wheel effectiveness. Part II - Correlations, Int. J. *Heat Mass Transfer,* 42(12), 2171-2185.

Sun, J., 2003. *An investigation of temperature and humidity variations during silica gel moisture interactions,* MSc. thesis in Mechanical Engineering, University of Saskatchewan.

Sun, J., and Besant, R.W., 2005. *Heat and Mass Transfer during Silica gel-Moisture Interactions*, Int. J Heat Mass, 48, 4953-4962.

Travkin, V.S. and Catton, I., 2001. Advances in Heat Transfer, Volume 34.

Zeng, Y.Y., 1990. *A study of the performance of run-around heat recovery system using aqueous glycol/air as the coupling fluid,* M.Sc thesis, University of Saskatchewan, Saskatoon, Canada.

Zeng, Y.Y., Besant, R.W., and Rezkallah, K.S., 1992. *The effect of Temperature Dependent Properties on the Performance of Run-Around Heat Recovery Systems Using Aqueous-Glycol Coupling Fluids,* ASHRAE Trans., 98(1), 551-562.

Appendix A Discretization of the Governing Equations

The two-dimensional control volume method (Patankar, 1980) is used to discretize the four governing equations. Figure A.1 shows the control volume in interior nodes and in the boundary nodes including four corners and four sides. In the interior, the control volume is $\Delta x \Delta y$; in the corner, it is $\frac{1}{4}\Delta x \Delta y$; and in four sides, it is $\frac{1}{2}\Delta x \Delta y$. In this appendix, the discretizations of interior nodes, top-left corner node, and top side nodes are illustrated. The rest of the nodes in corners and sides can be solved by the same method.

The node W is upstream of the node P in the air flow, and node E is downstream in the air flow. The node N is upstream of node P in the solid flow, and the node S is downstream in the solid flow. The properties in node P can be obtained by solving the partial differential equations.

The properties with the superscript "o" represent the average properties inside the control volume at current time t. There is no superscript "o" for the properties in new time step $t + \Delta t$.

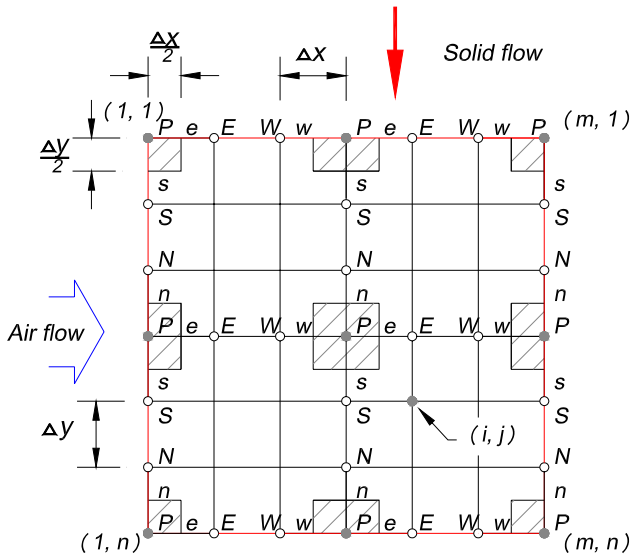

Figure A.1 Schematic of nodes inside interior and at the boundary of porous bed.

A.1 Governing Equations

Liquid phase continuity equation for adsorbed water on the desiccant coating:

$$\rho_l \frac{\partial \varepsilon_l}{\partial t} + \rho_l u_{sl} \frac{\partial \varepsilon_l}{\partial y} + \dot{m} = 0 \tag{2.7}$$

Gas energy equation:

$$\frac{\partial}{\partial t}\left(\varepsilon_g \rho_g Cp_g T_g\right) + \frac{\partial}{\partial x}\left(\rho_g u_g Cp_g T_g\right) = \frac{\partial}{\partial x}\left(\varepsilon_g K_g \frac{\partial T_g}{\partial x}\right) + \frac{\partial}{\partial y}\left(\varepsilon_g K_g \frac{\partial T_g}{\partial y}\right) - h_{gsl} S_v \left(T_g - T_{sl}\right) \tag{2.3}$$

Solid and liquid energy equation:

$$\frac{\partial}{\partial t}\left(\left(1-\varepsilon_g\right)\rho_{sl}Cp_{sl}T_{sl}\right)+\frac{\partial}{\partial y}\left(\left(1-\varepsilon_g\right)\rho_{sl}u_{sl}Cp_{sl}T_{sl}\right)=$$
$$\frac{\partial}{\partial x}\left(\left(1-\varepsilon_g\right)K_{sl,eff}\frac{\partial T_{sl}}{\partial x}\right)+\frac{\partial}{\partial y}\left(\left(1-\varepsilon_g\right)K_{sl,eff}\frac{\partial T_{sl}}{\partial y}\right) \quad (2.4)$$
$$+h_{gsl}S_v\left(T_g-T_{sl}\right)-\dot{m}h_{fg}-\dot{m}Cp_v\left(T_g-T_{sl}\right)$$

Mass transfer equation for the water vapour flow:

$$\frac{\partial\left(\varepsilon_g\rho_v\right)}{\partial t}+\frac{\partial}{\partial x}\left(\rho_v u_g\right)=\frac{\partial}{\partial x}\left(D_{v,eff}\frac{\partial\rho_v}{\partial x}\right)+\frac{\partial}{\partial y}\left(D_{v,eff}\frac{\partial\rho_v}{\partial y}\right)+\dot{m} \quad (2.5)$$

A.2 Interior Nodes

Interior node (i, j) is the node where $1<i<m$, and $1<j<n$. Integrate the governing equation over the differential control volume (w to e, and n to s) and over the time period (t to $t+\Delta t$):

1.) Discretization of aqueous phase continuity equation

$$\rho_l\frac{\partial\varepsilon_l}{\partial t}+\rho_l u_{sl}\frac{\partial\varepsilon_l}{\partial y}+\dot{m}=0 \quad (2.7)$$

$$\int_n^s \int_w^e \int_t^{t+\Delta t} \rho_l \frac{\partial \varepsilon_l}{\partial t} dt dx dy + \int_t^{t+\Delta t} \int_w^e \int_n^s \rho_l u_{sl} \frac{\partial \varepsilon_l}{\partial y} dy dx dt + \int_t^{t+\Delta t} \int_n^s \int_w^e \dot{m} dx dy dt = 0 \tag{A.1}$$

$$\left(\varepsilon_l - \varepsilon_l^o\right)_P \Delta x \Delta y + u_{sl}\left(\left(\varepsilon_l\right)_P - \left(\varepsilon_l\right)_N\right)\Delta x \Delta t + \frac{\dot{m}}{\rho_l} \Delta x \Delta y \Delta t = 0 \tag{A.2}$$

After rearrangement, the discretized phase continuity equation becomes:

$$a_P \left(\varepsilon_l\right)_P = a_N \left(\varepsilon_l\right)_N + b \tag{A.3}$$

Where,

$$a_P = \Delta y + u_{sl} \Delta t \tag{A.4}$$

$$a_N = u_{sl} \Delta t \tag{A.5}$$

$$b = \left(\varepsilon_l^o\right)_P \Delta y - \left(\frac{\dot{m}}{\rho_l}\right)_P \Delta y \Delta t \tag{A.6}$$

2.) Discretization of gas energy equation

$$\begin{aligned} &\frac{\partial}{\partial t}\left(\varepsilon_g \rho_g Cp_g T_g\right) + \frac{\partial}{\partial x}\left(\rho_g u_g Cp_g T_g\right) = \frac{\partial}{\partial x}\left(\varepsilon_g K_g \frac{\partial T_g}{\partial x}\right) \\ &+ \frac{\partial}{\partial y}\left(\varepsilon_g K_g \frac{\partial T_g}{\partial y}\right) - h_{gsl} S_v \left(T_g - T_{sl}\right) \end{aligned} \tag{2.3}$$

$$\int_n^s \int_w^e \int_t^{t+\Delta t} \frac{\partial}{\partial t}\left(\varepsilon_g \rho_g Cp_g T_g\right) dt dx dy + \int_t^{t+\Delta t} \int_n^s \int_w^e \frac{\partial}{\partial x}\left(\rho_g u_g Cp_g T_g\right) dx dy dt$$
$$= \int_t^{t+\Delta t} \int_n^s \int_w^e \frac{\partial}{\partial x}\left(\varepsilon_g K_g \frac{\partial T_g}{\partial x}\right) dx dy dt + \int_t^{t+\Delta t} \int_w^e \int_n^s \frac{\partial}{\partial y}\left(\varepsilon_g K_g \frac{\partial T_g}{\partial y}\right) dy dx dt \qquad \text{(A.7)}$$
$$- \int_t^{t+\Delta t} \int_n^s \int_w^e h_{gsl} S_v \left(T_g - T_{sl}\right) dx dy dt$$

$$\left(\varepsilon_g \rho_g Cp_g T_g - \varepsilon_g^o \rho_g^o Cp_g^o T_g^o\right)_P \Delta x \Delta y + \left(\rho_g u_g Cp_g\right)_e \left(T_g\right)_P \Delta y \Delta t - \left(\rho_g u_g Cp_g\right)_w \left(T_g\right)_W \Delta y \Delta t$$
$$= \left(\varepsilon_g K_g\right)_e \frac{\Delta y \Delta t}{\Delta x}\left(\left(T_g\right)_E - \left(T_g\right)_P\right) - \left(\varepsilon_g K_g\right)_w \frac{\Delta y \Delta t}{\Delta x}\left(\left(T_g\right)_P - \left(T_g\right)_W\right) + \left(\varepsilon_g K_g\right)_s \frac{\Delta x \Delta t}{\Delta y}\left(\left(T_g\right)_S - \left(T_g\right)_P\right)$$
$$- \left(\varepsilon_g K_g\right)_n \frac{\Delta x \Delta t}{\Delta y}\left(\left(T_g\right)_P - \left(T_g\right)_N\right) - h_{gsl} S_v \left(\left(T_g\right)_P - \left(T_{sl}\right)_P\right) \Delta x \Delta y \Delta t \qquad \text{(A.8)}$$

After rearrangement, the discretized gas energy equation becomes:

$$a_P \left(T_g\right)_P = a_E \left(T_g\right)_E + a_W \left(T_g\right)_W + a_S \left(T_g\right)_S + a_N \left(T_g\right)_N + b \qquad \text{(A.9)}$$

Where,

$$a_P = \left(\varepsilon_g \rho_g Cp_g\right)_P \Delta x \Delta y + \left(\rho_g u_g Cp_g\right)_e \Delta y \Delta t + \left(\varepsilon_g K_g\right)_e \frac{\Delta y \Delta t}{\Delta x} + \left(\varepsilon_g K_g\right)_w \frac{\Delta y \Delta t}{\Delta x}$$
$$+ \left(\varepsilon_g K_g\right)_s \frac{\Delta x \Delta t}{\Delta y} + \left(\varepsilon_g K_g\right)_n \frac{\Delta x \Delta t}{\Delta y} + h_{gsl} S_v \Delta x \Delta y \Delta t \qquad \text{(A.10)}$$

$$a_E = \left(\varepsilon_g K_g\right)_e \frac{\Delta y \Delta t}{\Delta x} \qquad \text{(A.11)}$$

$$a_W = \left(\rho_g u_g Cp_g\right)_w \Delta y \Delta t + \left(\varepsilon_g K_g\right)_w \frac{\Delta y \Delta t}{\Delta x} \qquad \text{(A.12)}$$

$$a_S = \left(\varepsilon_g K_g\right)_s \frac{\Delta x \Delta t}{\Delta y} \tag{A.13}$$

$$a_N = \left(\varepsilon_g K_g\right)_n \frac{\Delta x \Delta t}{\Delta y} \tag{A.14}$$

$$b = \left(\varepsilon_g^o \rho_g^o C p_g^o T_g^o\right)_P \Delta x \Delta y + h_{gsl} S_v \Delta x \Delta y \Delta t \left(T_{sl}\right)_P \tag{A.15}$$

The thermal conductivity of gas at the interface of two control volumes is determined by the spatial average:

$$\left(\varepsilon_g K_g\right)_e = \frac{2\left(\varepsilon_g K_g\right)_P \left(\varepsilon_g K_g\right)_E}{\left(\varepsilon_g K_g\right)_P + \left(\varepsilon_g K_g\right)_E} \tag{A.16}$$

$$\left(\varepsilon_g K_g\right)_w = \frac{2\left(\varepsilon_g K_g\right)_P \left(\varepsilon_g K_g\right)_W}{\left(\varepsilon_g K_g\right)_P + \left(\varepsilon_g K_g\right)_W} \tag{A.17}$$

$$\left(\varepsilon_g K_g\right)_s = \frac{2\left(\varepsilon_g K_g\right)_P \left(\varepsilon_g K_g\right)_S}{\left(\varepsilon_g K_g\right)_P + \left(\varepsilon_g K_g\right)_S} \tag{A.18}$$

$$\left(\varepsilon_g K_g\right)_n = \frac{2\left(\varepsilon_g K_g\right)_P \left(\varepsilon_g K_g\right)_N}{\left(\varepsilon_g K_g\right)_P + \left(\varepsilon_g K_g\right)_N} \tag{A.19}$$

Where,

$$\left(K_g\right)_x = \frac{\left(\rho_v K_v\right)_x + \left(\rho_a K_a\right)_x}{\left(\rho_v\right)_x + \left(\rho_a\right)_x}, \text{ x = P, E, W, S, N} \tag{A.20}$$

3.) Discretization of solid and liquid energy equation

$$\begin{aligned}
&\frac{\partial}{\partial t}\left(\left(1-\varepsilon_g\right)\rho_{sl} Cp_{sl} T_{sl}\right) + \frac{\partial}{\partial y}\left(\left(1-\varepsilon_g\right)\rho_{sl} u_{sl} Cp_{sl} T_{sl}\right) = \\
&\frac{\partial}{\partial x}\left(\left(1-\varepsilon_g\right)K_{sl,eff}\frac{\partial T_{sl}}{\partial x}\right) + \frac{\partial}{\partial y}\left(\left(1-\varepsilon_g\right)K_{sl,eff}\frac{\partial T_{sl}}{\partial y}\right) \\
&+ h_{gsl} S_v \left(T_g - T_{sl}\right) - \dot{m} h_{fg} - \dot{m} Cp_v \left(T_g - T_{sl}\right)
\end{aligned} \tag{2.4}$$

$$\begin{aligned}
&\int_n^s \int_w^e \int_t^{t+\Delta t} \frac{\partial}{\partial t}\left(\left(1-\varepsilon_g\right)\rho_{sl} Cp_{sl} T_{sl}\right) dt dx dy + \int_t^{t+\Delta t} \int_w^e \int_n^s \frac{\partial}{\partial y}\left(\left(1-\varepsilon_g\right)\rho_{sl} u_{sl} Cp_{sl} T_{sl}\right) dy dx dt \\
&= \int_t^{t+\Delta t} \int_n^s \int_w^e \frac{\partial}{\partial x}\left(\left(1-\varepsilon_g\right)K_{sl,eff}\frac{\partial T_{sl}}{\partial x}\right) dx dy dt + \int_t^{t+\Delta t} \int_w^e \int_n^s \frac{\partial}{\partial y}\left(\left(1-\varepsilon_g\right)K_{sl,eff}\frac{\partial T_{sl}}{\partial y}\right) dy dx dt \\
&+ \int_t^{t+\Delta t} \int_n^s \int_w^e h_{gsl} S_v \left(T_g - T_{sl}\right) dx dy dt - \int_t^{t+\Delta t} \int_n^s \int_w^e \dot{m} h_{fg} \, dx dy dt \\
&- \int_t^{t+\Delta t} \int_n^s \int_w^e \dot{m} Cp_v \left(T_g - T_{sl}\right) dx dy dt
\end{aligned} \tag{A.21}$$

$$\begin{aligned}
&\left(\left(1-\varepsilon_g\right)\rho_{sl} Cp_{sl} T_{sl} - \left(1-\varepsilon_g^o\right)\rho_{sl}^o Cp_{sl}^o T_{sl}^o\right)_P \Delta x \Delta y + \left(\left(1-\varepsilon_g\right)\rho_{sl} u_{sl} Cp_{sl}\right)_n \Delta x \Delta t \left(T_{sl}\right)_P \\
&- \left(\left(1-\varepsilon_g\right)\rho_{sl} u_{sl} Cp_{sl}\right)_n \Delta x \Delta t \left(T_{sl}\right)_N = \left(\left(1-\varepsilon_g\right)K_{sl,eff}\right)_e \frac{\Delta y \Delta t}{\Delta x}\left(\left(T_{sl}\right)_E - \left(T_{sl}\right)_P\right) \\
&- \left(\left(1-\varepsilon_g\right)K_{sl,eff}\right)_w \frac{\Delta y \Delta t}{\Delta x}\left(\left(T_{sl}\right)_P - \left(T_{sl}\right)_W\right) + \left(\left(1-\varepsilon_g\right)K_{sl,eff}\right)_s \frac{\Delta x \Delta t}{\Delta y}\left(\left(T_{sl}\right)_S - \left(T_{sl}\right)_P\right) \\
&- \left(\left(1-\varepsilon_g\right)K_{sl,eff}\right)_n \frac{\Delta x \Delta t}{\Delta y}\left(\left(T_{sl}\right)_P - \left(T_{sl}\right)_N\right) + h_{gsl} S_v \left(\left(T_g\right)_P - \left(T_{sl}\right)_P\right)\Delta x \Delta y \Delta t \\
&- \dot{m} h_{fg} \Delta x \Delta y \Delta t - \dot{m} Cp_v \left(\left(T_g\right)_P - \left(T_{sl}\right)_P\right)\Delta x \Delta y \Delta t
\end{aligned} \tag{A.22}$$

After rearrangement, the discretized solid and liquid energy equation becomes:

$$a_P\left(T_{sl}\right)_P = a_E\left(T_{sl}\right)_E + a_W\left(T_{sl}\right)_W + a_S\left(T_{sl}\right)_S + a_N\left(T_{sl}\right)_N + b \tag{A.23}$$

Where,

$$\begin{aligned} a_P &= \left(\left(1-\varepsilon_g\right)\rho_{sl}Cp_{sl}\right)_P \Delta x\Delta y + \left(\left(1-\varepsilon_g\right)\rho_{sl}u_{sl}Cp_{sl}\right)_n \Delta x\Delta t + \left(\left(1-\varepsilon_g\right)K_{sl,eff}\right)_e \frac{\Delta y\Delta t}{\Delta x} \\ &+ \left(\left(1-\varepsilon_g\right)K_{sl,eff}\right)_w \frac{\Delta y\Delta t}{\Delta x} + \left(\left(1-\varepsilon_g\right)K_{sl,eff}\right)_s \frac{\Delta x\Delta t}{\Delta y} + \left(\left(1-\varepsilon_g\right)K_{sl,eff}\right)_n \frac{\Delta x\Delta t}{\Delta y} \\ &+ \left(h_{gsl}S_v - \dot{m}Cp_v\right)\Delta x\Delta y\Delta t \end{aligned} \tag{A.24}$$

$$a_E = \left(\left(1-\varepsilon_g\right)K_{sl,eff}\right)_e \frac{\Delta y\Delta t}{\Delta x} \tag{A.25}$$

$$a_W = \left(\left(1-\varepsilon_g\right)K_{sl,eff}\right)_w \frac{\Delta y\Delta t}{\Delta x} \tag{A.26}$$

$$a_S = \left(\left(1-\varepsilon_g\right)K_{sl,eff}\right)_s \frac{\Delta x\Delta t}{\Delta y} \tag{A.27}$$

$$a_N = \left(\left(1-\varepsilon_g\right)K_{sl,eff}\right)_n \frac{\Delta x\Delta t}{\Delta y} + \left(\left(1-\varepsilon_g\right)\rho_{sl}u_{sl}Cp_{sl}\right)_n \Delta x\Delta t \tag{A.28}$$

$$b = \left(\left(1-\varepsilon_g^o\right)\rho_{sl}^o Cp_{sl}^o T_{sl}^o\right)_P \Delta x\Delta y + \left(h_{gsl}S_v - \dot{m}Cp_v\right)\left(T_g\right)_P \Delta x\Delta y\Delta t - \dot{m}h_{fg}\Delta x\Delta y\Delta t \tag{A.29}$$

The thermal conductivity of solid and liquid at the interface of two control volumes is determined by the spatial average:

$$\left(\left(1-\varepsilon_g\right)K_{sl,eff}\right)_e = \frac{2\left(\left(1-\varepsilon_g\right)K_{sl,eff}\right)_P\left(\left(1-\varepsilon_g\right)K_{sl,eff}\right)_E}{\left(\left(1-\varepsilon_g\right)K_{sl,eff}\right)_P + \left(\left(1-\varepsilon_g\right)K_{sl,eff}\right)_E} \tag{A.30}$$

$$\left(\left(1-\varepsilon_g\right)K_{sl,eff}\right)_w = \frac{2\left(\left(1-\varepsilon_g\right)K_{sl,eff}\right)_P\left(\left(1-\varepsilon_g\right)K_{sl,eff}\right)_W}{\left(\left(1-\varepsilon_g\right)K_{sl,eff}\right)_P + \left(\left(1-\varepsilon_g\right)K_{sl,eff}\right)_W} \tag{A.31}$$

$$\left(\left(1-\varepsilon_g\right)K_{sl,eff}\right)_s = \frac{2\left(\left(1-\varepsilon_g\right)K_{sl,eff}\right)_P\left(\left(1-\varepsilon_g\right)K_{sl,eff}\right)_S}{\left(\left(1-\varepsilon_g\right)K_{sl,eff}\right)_P + \left(\left(1-\varepsilon_g\right)K_{sl,eff}\right)_S} \tag{A.32}$$

$$\left(\left(1-\varepsilon_g\right)K_{sl,eff}\right)_n = \frac{2\left(\left(1-\varepsilon_g\right)K_{sl,eff}\right)_P\left(\left(1-\varepsilon_g\right)K_{sl,eff}\right)_N}{\left(\left(1-\varepsilon_g\right)K_{sl,eff}\right)_P + \left(\left(1-\varepsilon_g\right)K_{sl,eff}\right)_N} \tag{A.33}$$

Where,

$$\left(K_{sl,eff}\right)_x = \frac{\varepsilon_s K_s + \left(\varepsilon_l\right)_x K_l}{\varepsilon_s + \left(\varepsilon_l\right)_x}, \text{ x = P, E, W, S, N} \tag{A.34}$$

4.) Discretization of water vapour transfer equation

$$\frac{\partial\left(\varepsilon_g\rho_v\right)}{\partial t} + \frac{\partial}{\partial x}\left(\rho_v u_g\right) = \frac{\partial}{\partial x}\left(D_{v,eff}\frac{\partial\rho_v}{\partial x}\right) + \frac{\partial}{\partial y}\left(D_{v,eff}\frac{\partial\rho_v}{\partial y}\right) + \dot{m} \tag{2.5}$$

$$\int_n^s\int_w^e\int_t^{t+\Delta t}\frac{\partial\left(\varepsilon_g\rho_v\right)}{\partial t}dtdxdy+\int_t^{t+\Delta t}\int_n^s\int_w^e\frac{\partial}{\partial x}\left(\rho_v u_g\right)dxdydt$$
$$=\int_t^{t+\Delta t}\int_n^s\int_w^e\frac{\partial}{\partial x}\left(D_{v,eff}\frac{\partial\rho_v}{\partial x}\right)dxdydt+\int_t^{t+\Delta t}\int_w^e\int_n^s\frac{\partial}{\partial y}\left(D_{v,eff}\frac{\partial\rho_v}{\partial y}\right)dydxdt+\int_t^{t+\Delta t}\int_n^s\int_w^e\dot{m}dxdydt \quad (A.35)$$

$$\begin{aligned}&\left(\varepsilon_g\rho_v-\varepsilon_g^o\rho_v^o\right)_P\Delta x\Delta y+\left(\left(u_g\rho_v\right)_P-\left(u_g\rho_v\right)_W\right)\Delta y\Delta t\\&=\left(D_{v,eff}\right)_e\frac{\Delta y\Delta t}{\Delta x}\left(\left(\rho_v\right)_E-\left(\rho_v\right)_P\right)-\left(D_{v,eff}\right)_w\frac{\Delta y\Delta t}{\Delta x}\left(\left(\rho_v\right)_P-\left(\rho_v\right)_W\right)\\&+\left(D_{v,eff}\right)_s\frac{\Delta x\Delta t}{\Delta y}\left(\left(\rho_v\right)_S-\left(\rho_v\right)_P\right)-\left(D_{v,eff}\right)_n\frac{\Delta x\Delta t}{\Delta y}\left(\left(\rho_v\right)_P-\left(\rho_v\right)_N\right)+\dot{m}\Delta x\Delta y\Delta t\end{aligned} \quad (A.36)$$

After rearrangement, the discretized water vapour transfer equation becomes:

$$a_P\left(\rho_v\right)_P=a_E\left(\rho_v\right)_E+a_W\left(\rho_v\right)_W+a_S\left(\rho_v\right)_S+a_N\left(\rho_v\right)_N+b \quad (A.37)$$

Where,

$$\begin{aligned}a_P&=\left(\varepsilon_g\right)_P\Delta x\Delta y+\left(u_g\right)_P\Delta y\Delta t+\left(D_{v,eff}\right)_e\frac{\Delta y\Delta t}{\Delta x}+\left(D_{v,eff}\right)_w\frac{\Delta y\Delta t}{\Delta x}+\left(D_{v,eff}\right)_s\frac{\Delta x\Delta t}{\Delta y}\\&+\left(D_{v,eff}\right)_n\frac{\Delta x\Delta t}{\Delta y}\end{aligned} \quad (A.38)$$

$$a_E=\left(D_{v,eff}\right)_e\frac{\Delta y\Delta t}{\Delta x} \quad (A.39)$$

$$a_W=\left(D_{v,eff}\right)_w\frac{\Delta y\Delta t}{\Delta x}+\left(u_g\right)_W\Delta y\Delta t \quad (A.40)$$

$$a_S = \left(D_{v,eff}\right)_s \frac{\Delta x \Delta t}{\Delta y} \tag{A.41}$$

$$a_N = \left(D_{v,eff}\right)_n \frac{\Delta x \Delta t}{\Delta y} \tag{A.42}$$

$$b = \left(\varepsilon_g^o \rho_v^o\right)_P \Delta x \Delta y + \dot{m} \Delta x \Delta y \Delta t \tag{A.43}$$

The diffusion coefficient at the interface of two control volumes is determined by the spatial average:

$$\left(D_{v,eff}\right)_e = \frac{2\left(D_{v,eff}\right)_P \left(D_{v,eff}\right)_E}{\left(D_{v,eff}\right)_P + \left(D_{v,eff}\right)_E} \tag{A.44}$$

$$\left(D_{v,eff}\right)_w = \frac{2\left(D_{v,eff}\right)_P \left(D_{v,eff}\right)_W}{\left(D_{v,eff}\right)_P + \left(D_{v,eff}\right)_W} \tag{A.45}$$

$$\left(D_{v,eff}\right)_s = \frac{2\left(D_{v,eff}\right)_P \left(D_{v,eff}\right)_S}{\left(D_{v,eff}\right)_P + \left(D_{v,eff}\right)_S} \tag{A.46}$$

$$\left(D_{v,eff}\right)_n = \frac{2\left(D_{v,eff}\right)_P \left(D_{v,eff}\right)_N}{\left(D_{v,eff}\right)_P + \left(D_{v,eff}\right)_N} \tag{A.47}$$

Where,

$$\left(D_{v,eff}\right)_x = \frac{\left(\varepsilon_g\right)_x D_v}{\tau}, \text{ x = P, E, W, S, N} \tag{A.48}$$

A.3 Top Side Boundary

Top side node (i, j) is the node where $1 < i < m$, and $j = 1$. Integrate the governing equation over the differential control volume (w to e, and P to s) and over the time period (t to $t + \Delta t$):

1.) Discretization of aqueous phase continuity equation

$$\rho_l \frac{\partial \varepsilon_l}{\partial t} + \rho_l u_{sl} \frac{\partial \varepsilon_l}{\partial y} + \dot{m} = 0 \tag{2.7}$$

$$\int_P^s \int_w^e \int_t^{t+\Delta t} \rho_l \frac{\partial \varepsilon_l}{\partial t} dt dx dy + \int_t^{t+\Delta t} \int_w^e \int_P^s \rho_l u_{sl} \frac{\partial \varepsilon_l}{\partial y} dy dx dt + \int_t^{t+\Delta t} \int_P^s \int_w^e \dot{m}\, dx dy dt = 0 \tag{A.49}$$

$$\left(\varepsilon_l - \varepsilon_l^o\right)_P \Delta x \frac{\Delta y}{2} + u_{sl}\left(\left(\varepsilon_l\right)_P - \left(\varepsilon_l\right)_{in}\right)\Delta x \Delta t + \frac{\dot{m}}{\rho_l} \Delta x \frac{\Delta y}{2} \Delta t = 0 \tag{A.50}$$

After rearrangement, the discretized phase continuity equation becomes:

$$a_P \left(\varepsilon_l\right)_P = b \tag{A.51}$$

Where,

$$a_P = \frac{1}{2}\Delta y + u_{sl}\Delta t \tag{A.52}$$

$$b = \frac{1}{2}\left(\varepsilon_l^o\right)_P \Delta y - \frac{1}{2}\left(\frac{\dot{m}}{\rho_l}\right)_P \Delta y \Delta t + u_{sl}\Delta t\left(\varepsilon_l\right)_{in} \tag{A.53}$$

2.) Discretization of gas energy equation

$$\begin{aligned}&\frac{\partial}{\partial t}\left(\varepsilon_g \rho_g Cp_g T_g\right) + \frac{\partial}{\partial x}\left(\rho_g u_g Cp_g T_g\right) = \frac{\partial}{\partial x}\left(\varepsilon_g K_g \frac{\partial T_g}{\partial x}\right) \\ &+ \frac{\partial}{\partial y}\left(\varepsilon_g K_g \frac{\partial T_g}{\partial y}\right) - h_{gsl} S_v \left(T_g - T_{sl}\right)\end{aligned} \tag{2.3}$$

$$\begin{aligned}&\int_P^s \int_w^e \int_t^{t+\Delta t} \frac{\partial}{\partial t}\left(\varepsilon_g \rho_g Cp_g T_g\right) dt dx dy + \int_t^{t+\Delta t} \int_P^s \int_w^e \frac{\partial}{\partial x}\left(\rho_g u_g Cp_g T_g\right) dx dy dt \\ &= \int_t^{t+\Delta t} \int_P^s \int_w^e \frac{\partial}{\partial x}\left(\varepsilon_g K_g \frac{\partial T_g}{\partial x}\right) dx dy dt + \int_t^{t+\Delta t} \int_w^e \int_P^s \frac{\partial}{\partial y}\left(\varepsilon_g K_g \frac{\partial T_g}{\partial y}\right) dy dx dt \\ &- \int_t^{t+\Delta t} \int_P^s \int_w^e h_{gsl} S_v \left(T_g - T_{sl}\right) dx dy dt\end{aligned} \tag{A.54}$$

$$\begin{aligned}&\left(\varepsilon_g \rho_g Cp_g T_g - \varepsilon_g^o \rho_g^o Cp_g^o T_g^o\right)_P \Delta x \frac{\Delta y}{2} + \left(\rho_g u_g Cp_g\right)_e \left(T_g\right)_P \frac{\Delta y}{2}\Delta t - \left(\rho_g u_g Cp_g\right)_w \left(T_g\right)_W \frac{\Delta y}{2}\Delta t \\ &= \frac{1}{2}\left(\varepsilon_g K_g\right)_e \frac{\Delta y \Delta t}{\Delta x}\left(\left(T_g\right)_E - \left(T_g\right)_P\right) - \frac{1}{2}\left(\varepsilon_g K_g\right)_w \frac{\Delta y \Delta t}{\Delta x}\left(\left(T_g\right)_P - \left(T_g\right)_W\right) \\ &+ \left(\varepsilon_g K_g\right)_s \frac{\Delta x \Delta t}{\Delta y}\left(\left(T_g\right)_S - \left(T_g\right)_P\right) - h_{gsl} S_v \left(\left(T_g\right)_P - \left(T_{sl}\right)_P\right)\Delta x \frac{\Delta y}{2}\Delta t\end{aligned} \tag{A.55}$$

After rearrangement, the discretized gas energy equation becomes:

$$a_P\left(T_g\right)_P = a_E\left(T_g\right)_E + a_W\left(T_g\right)_W + a_S\left(T_g\right)_S + b \tag{A.56}$$

Where,

$$a_P = \frac{1}{2}\left(\varepsilon_g \rho_g Cp_g\right)_P \Delta x\Delta y + \frac{1}{2}\left(\rho_g u_g Cp_g\right)_e \Delta y\Delta t + \frac{1}{2}\left(\varepsilon_g K_g\right)_e \frac{\Delta y\Delta t}{\Delta x} + \frac{1}{2}\left(\varepsilon_g K_g\right)_w \frac{\Delta y\Delta t}{\Delta x} + \left(\varepsilon_g K_g\right)_s \frac{\Delta x\Delta t}{\Delta y} + \frac{1}{2} h_{gsl} S_v \Delta x\Delta y\Delta t \tag{A.57}$$

$$a_E = \frac{1}{2}\left(\varepsilon_g K_g\right)_e \frac{\Delta y\Delta t}{\Delta x} \tag{A.58}$$

$$a_W = \frac{1}{2}\left(\varepsilon_g K_g\right)_w \frac{\Delta y\Delta t}{\Delta x} + \left(\rho_g u_g Cp_g\right)_w \frac{\Delta y}{2}\Delta t \tag{A.59}$$

$$a_S = \left(\varepsilon_g K_g\right)_s \frac{\Delta x\Delta t}{\Delta y} \tag{A.60}$$

$$b = \frac{1}{2}\left(\varepsilon_g^o \rho_g^o Cp_g^o T_g^o\right)_P \Delta x\Delta y + \frac{1}{2} h_{gsl} S_v \Delta x\Delta y\Delta t\left(T_{sl}\right)_P \tag{A.61}$$

3.) Discretization of solid and liquid energy equation

$$\frac{\partial}{\partial t}\left(\left(1-\varepsilon_g\right)\rho_{sl}Cp_{sl}T_{sl}\right)+\frac{\partial}{\partial y}\left(\left(1-\varepsilon_g\right)\rho_{sl}u_{sl}Cp_{sl}T_{sl}\right)=$$
$$\frac{\partial}{\partial x}\left(\left(1-\varepsilon_g\right)K_{sl,eff}\frac{\partial T_{sl}}{\partial x}\right)+\frac{\partial}{\partial y}\left(\left(1-\varepsilon_g\right)K_{sl,eff}\frac{\partial T_{sl}}{\partial y}\right) \qquad (2.4)$$
$$+h_{gsl}S_v\left(T_g-T_{sl}\right)-\dot{m}h_{fg}-\dot{m}Cp_v\left(T_g-T_{sl}\right)$$

$$\int_P^s\int_w^e\int_t^{t+\Delta t}\frac{\partial}{\partial t}\left(\left(1-\varepsilon_g\right)\rho_{sl}Cp_{sl}T_{sl}\right)dtdxdy+\int_t^{t+\Delta t}\int_w^e\int_P^s\frac{\partial}{\partial y}\left(\left(1-\varepsilon_g\right)\rho_{sl}u_{sl}Cp_{sl}T_{sl}\right)dydxdt$$
$$=\int_t^{t+\Delta t}\int_P^s\int_w^e\frac{\partial}{\partial x}\left(\left(1-\varepsilon_g\right)K_{sl,eff}\frac{\partial T_{sl}}{\partial x}\right)dxdydt+\int_t^{t+\Delta t}\int_w^e\int_P^s\frac{\partial}{\partial y}\left(\left(1-\varepsilon_g\right)K_{sl,eff}\frac{\partial T_{sl}}{\partial y}\right)dydxdt$$
$$+\int_t^{t+\Delta t}\int_P^s\int_w^e h_{gsl}S_v\left(T_g-T_{sl}\right)dxdydt-\int_t^{t+\Delta t}\int_P^s\int_w^e\dot{m}h_{fg}\,dxdydt$$
$$-\int_t^{t+\Delta t}\int_P^s\int_w^e\dot{m}Cp_v\left(T_g-T_{sl}\right)dxdydt$$

(A.62)

$$\left(\left(1-\varepsilon_g\right)\rho_{sl}Cp_{sl}T_{sl}-\left(1-\varepsilon_g^o\right)\rho_{sl}^oCp_{sl}^oT_{sl}^o\right)_P\Delta x\frac{\Delta y}{2}+\left(\left(1-\varepsilon_g\right)\rho_{sl}u_{sl}Cp_{sl}\right)_P\Delta x\Delta t\left(T_{sl}\right)_P$$
$$-\left(\left(1-\varepsilon_g\right)\rho_{sl}u_{sl}Cp_{sl}\right)_P\Delta x\Delta t\left(T_{sl}\right)_{in}=\frac{1}{2}\left(\left(1-\varepsilon_g\right)K_{sl,eff}\right)_e\frac{\Delta y\Delta t}{\Delta x}\left(\left(T_{sl}\right)_E-\left(T_{sl}\right)_P\right) \qquad (A.63)$$
$$-\frac{1}{2}\left(\left(1-\varepsilon_g\right)K_{sl,eff}\right)_w\frac{\Delta y\Delta t}{\Delta x}\left(\left(T_{sl}\right)_P-\left(T_{sl}\right)_W\right)+\left(\left(1-\varepsilon_g\right)K_{sl,eff}\right)_s\frac{\Delta x\Delta t}{\Delta y}\left(\left(T_{sl}\right)_S-\left(T_{sl}\right)_P\right)$$
$$+h_{gsl}S_v\left(\left(T_g\right)_P-\left(T_{sl}\right)_P\right)\Delta x\frac{\Delta y}{2}\Delta t-\dot{m}h_{fg}\Delta x\frac{\Delta y}{2}\Delta t-\dot{m}Cp_v\left(\left(T_g\right)_P-\left(T_{sl}\right)_P\right)\Delta x\frac{\Delta y}{2}\Delta t$$

After rearrangement, the discretized solid and liquid energy equation becomes:

$$a_P\left(T_{sl}\right)_P=a_E\left(T_{sl}\right)_E+a_W\left(T_{sl}\right)_W+a_S\left(T_{sl}\right)_S+b \qquad (A.64)$$

Where,

$$a_P = \frac{1}{2}\left(\left(1-\varepsilon_g\right)\rho_{sl}Cp_{sl}\right)_P \Delta x\Delta y + \left(\left(1-\varepsilon_g\right)\rho_{sl}u_{sl}Cp_{sl}\right)_P \Delta x\Delta t + \frac{1}{2}\left(\left(1-\varepsilon_g\right)K_{sl,eff}\right)_e \frac{\Delta y\Delta t}{\Delta x} + \frac{1}{2}\left(\left(1-\varepsilon_g\right)K_{sl,eff}\right)_w \frac{\Delta y\Delta t}{\Delta x} + \left(\left(1-\varepsilon_g\right)K_{sl,eff}\right)_s \frac{\Delta x\Delta t}{\Delta y} + \frac{1}{2}(h_{gsl}S_v - \dot{m}Cp_v)\Delta x\Delta y\Delta t \quad \text{(A.65)}$$

$$a_E = \frac{1}{2}\left(\left(1-\varepsilon_g\right)K_{sl,eff}\right)_e \frac{\Delta y\Delta t}{\Delta x} \quad \text{(A.66)}$$

$$a_W = \frac{1}{2}\left(\left(1-\varepsilon_g\right)K_{sl,eff}\right)_w \frac{\Delta y\Delta t}{\Delta x} \quad \text{(A.67)}$$

$$a_S = \left(\left(1-\varepsilon_g\right)K_{sl,eff}\right)_s \frac{\Delta x\Delta t}{\Delta y} \quad \text{(A.68)}$$

$$b = \frac{1}{2}\left(\left(1-\varepsilon_g^o\right)\rho_{sl}^o Cp_{sl}^o T_{sl}^o\right)_P \Delta x\Delta y + \frac{1}{2}(h_{gsl}S_v - \dot{m}Cp_v)\left(T_g\right)_P \Delta x\Delta y\Delta t - \frac{1}{2}\dot{m}h_{fg}\Delta x\Delta y\Delta t + \left(\left(1-\varepsilon_g\right)\rho_{sl}u_{sl}Cp_{sl}\right)_P \Delta x\Delta t\left(T_{sl}\right)_{in} \quad \text{(A.69)}$$

4.) Discretization of water vapour transfer equation

$$\frac{\partial\left(\varepsilon_g\rho_v\right)}{\partial t} + \frac{\partial}{\partial x}\left(\rho_v u_g\right) = \frac{\partial}{\partial x}\left(D_{v,eff}\frac{\partial\rho_v}{\partial x}\right) + \frac{\partial}{\partial y}\left(D_{v,eff}\frac{\partial\rho_v}{\partial y}\right) + \dot{m} \quad \text{(2.5)}$$

$$\int_P^s \int_w^e \int_t^{t+\Delta t} \frac{\partial \left(\varepsilon_g \rho_v\right)}{\partial t} dt dx dy \quad + \int_t^{t+\Delta t} \int_P^s \int_w^e \frac{\partial}{\partial x}\left(\rho_v u_g\right) dx dy dt$$
$$= \int_t^{t+\Delta t} \int_P^s \int_w^e \frac{\partial}{\partial x}\left(D_{v,eff} \ \frac{\partial \rho_v}{\partial x}\right) dx dy dt \quad + \int_t^{t+\Delta t} \int_w^e \int_P^s \frac{\partial}{\partial y}\left(D_{v,eff} \ \frac{\partial \rho_v}{\partial y}\right) dy dx dt$$
$$+ \int_t^{t+\Delta t} \int_P^s \int_w^e \dot{m} \, dx dy dt \tag{A.70}$$

$$\left(\varepsilon_g \rho_v - \varepsilon_g^o \rho_v^o\right)_P \Delta x \frac{\Delta y}{2} + \left(\left(u_g \rho_v\right)_P - \left(u_g \rho_v\right)_W\right)\frac{\Delta y}{2}\Delta t = \left(D_{v,eff}\right)_e \frac{\Delta y \Delta t}{2\Delta x}\left(\left(\rho_v\right)_E - \left(\rho_v\right)_P\right)$$
$$- \left(D_{v,eff}\right)_w \frac{\Delta y \Delta t}{2\Delta x}\left(\left(\rho_v\right)_P - \left(\rho_v\right)_W\right) + \left(D_{v,eff}\right)_s \frac{\Delta x \Delta t}{\Delta y}\left(\left(\rho_v\right)_S - \left(\rho_v\right)_P\right) + \dot{m}\Delta x \frac{\Delta y}{2}\Delta t \tag{A.71}$$

After rearrangement, the discretized water vapour transfer equation becomes:

$$a_P\left(\rho_v\right)_P = a_E\left(\rho_v\right)_E + a_W\left(\rho_v\right)_W + a_S\left(\rho_v\right)_S + b \tag{A.72}$$

Where,

$$a_P = \frac{1}{2}\left(\varepsilon_g\right)_P \Delta x \Delta y + \frac{1}{2}\left(u_g\right)_P \Delta y \Delta t + \frac{1}{2}\left(D_{v,eff}\right)_e \frac{\Delta y \Delta t}{\Delta x} + \frac{1}{2}\left(D_{v,eff}\right)_w \frac{\Delta y \Delta t}{\Delta x} + \left(D_{v,eff}\right)_s \frac{\Delta x \Delta t}{\Delta y}$$

(A.73)

$$a_E = \frac{1}{2}\left(D_{v,eff}\right)_e \frac{\Delta y \Delta t}{\Delta x} \tag{A.74}$$

$$a_W = \left(D_{v,eff}\right)_w \frac{\Delta y \Delta t}{2\Delta x} + \left(u_g\right)_W \frac{\Delta y}{2}\Delta t \tag{A.75}$$

$$a_S = \left(D_{v,eff}\right)_s \frac{\Delta x \Delta t}{\Delta y} \tag{A.76}$$

$$b = \frac{1}{2}\left(\varepsilon_g^o \rho_v^o\right)_P \Delta x \Delta y + \frac{1}{2}\dot{m}\Delta x \Delta y \Delta t \tag{A.77}$$

A.4 Top Left Corner Boundary

Top left corner node (i, j) is the node where $i = 1$, and $j = 1$. Integrate the governing equation over the differential control volume (P to e, and P to s) and over the time period (t to $t + \Delta t$):

2.) Discretization of aqueous phase continuity equation

$$\rho_l \frac{\partial \varepsilon_l}{\partial t} + \rho_l u_{sl} \frac{\partial \varepsilon_l}{\partial y} + \dot{m} = 0 \tag{2.7}$$

$$\int_P^s \int_P^e \int_t^{t+\Delta t} \rho_l \frac{\partial \varepsilon_l}{\partial t} dt dx dy + \int_t^{t+\Delta t} \int_P^e \int_P^s \rho_l u_{sl} \frac{\partial \varepsilon_l}{\partial y} dy dx dt + \int_t^{t+\Delta t} \int_P^s \int_P^e \dot{m}\, dx dy dt = 0 \tag{A.78}$$

$$\left(\varepsilon_l - \varepsilon_l^o\right)_P \frac{\Delta x}{2}\frac{\Delta y}{2} + u_{sl}\left(\left(\varepsilon_l\right)_P - \left(\varepsilon_l\right)_{in}\right)\frac{\Delta x}{2}\Delta t + \frac{\dot{m}}{\rho_l}\frac{\Delta x}{2}\frac{\Delta y}{2}\Delta t = 0 \tag{A.79}$$

After rearrangement, the discretized phase continuity equation becomes:

$$a_P(\varepsilon_l)_P = b \tag{A.80}$$

Where,

$$a_P = \frac{1}{4}\Delta y + \frac{1}{2}u_{sl}\Delta t \tag{A.81}$$

$$b = \frac{1}{4}(\varepsilon_l^o)_P \Delta y - \frac{1}{4}\left(\frac{\dot{m}}{\rho_l}\right)_P \Delta y \Delta t + \frac{1}{2}u_{sl}(\varepsilon_l)_{in}\Delta t \tag{A.82}$$

2.) Discretization of gas energy equation

$$\begin{aligned}&\frac{\partial}{\partial t}(\varepsilon_g \rho_g Cp_g T_g) + \frac{\partial}{\partial x}(\rho_g u_g Cp_g T_g) = \frac{\partial}{\partial x}\left(\varepsilon_g K_g \frac{\partial T_g}{\partial x}\right)\\ &+ \frac{\partial}{\partial y}\left(\varepsilon_g K_g \frac{\partial T_g}{\partial y}\right) - h_{gsl} S_v (T_g - T_{sl})\end{aligned} \tag{2.3}$$

$$\begin{aligned}&\int_P^s \int_P^e \int_t^{t+\Delta t} \frac{\partial}{\partial t}(\varepsilon_g \rho_g Cp_g T_g)\,dt\,dx\,dy + \int_t^{t+\Delta t} \int_P^s \int_P^e \frac{\partial}{\partial x}(\rho_g u_g Cp_g T_g)\,dx\,dy\,dt\\ &= \int_t^{t+\Delta t} \int_P^s \int_P^e \frac{\partial}{\partial x}\left(\varepsilon_g K_g \frac{\partial T_g}{\partial x}\right)dx\,dy\,dt + \int_t^{t+\Delta t} \int_P^e \int_P^s \frac{\partial}{\partial y}\left(\varepsilon_g K_g \frac{\partial T_g}{\partial y}\right)dy\,dx\,dt\\ &- \int_t^{t+\Delta t} \int_P^s \int_P^e h_{gsl} S_v (T_g - T_{sl})\,dx\,dy\,dt\end{aligned} \tag{A.83}$$

$$\left(\varepsilon_g \rho_g Cp_g T_g - \varepsilon_g^o \rho_g^o Cp_g^o T_g^o\right)_P \frac{\Delta x}{2}\frac{\Delta y}{2} + \left(\rho_g u_g Cp_g\right)_e \left(T_g\right)_P \frac{\Delta y}{2}\Delta t - \left(\rho_g u_g Cp_g\right)_P T_{g,in} \frac{\Delta y}{2}\Delta t$$
$$= \left(\varepsilon_g K_g\right)_e \frac{\Delta y \Delta t}{2\Delta x}\left(\left(T_g\right)_E - \left(T_g\right)_P\right) + \left(\varepsilon_g K_g\right)_s \frac{\Delta x \Delta t}{2\Delta y}\left(\left(T_g\right)_S - \left(T_g\right)_P\right) - h_{gsl} S_v \left(\left(T_g\right)_P - \left(T_{sl}\right)_P\right)\frac{\Delta x}{2}\frac{\Delta y}{2}\Delta t \quad \text{(A.84)}$$

After rearrangement, the discretized gas energy equation becomes:

$$a_P \left(T_g\right)_P = a_E \left(T_g\right)_E + a_S \left(T_g\right)_S + b \quad \text{(A.85)}$$

Where,

$$a_P = \frac{1}{4}\left(\varepsilon_g \rho_g Cp_g\right)_P \Delta x \Delta y + \frac{1}{2}\left(\rho_g u_g Cp_g\right)_e \Delta y \Delta t + \frac{1}{2}\left(\varepsilon_g K_g\right)_e \frac{\Delta y \Delta t}{\Delta x} +$$
$$\frac{1}{2}\left(\varepsilon_g K_g\right)_s \frac{\Delta x \Delta t}{\Delta y} + \frac{1}{4} h_{gsl} S_v \Delta x \Delta y \Delta t \quad \text{(A.86)}$$

$$a_E = \frac{1}{2}\left(\varepsilon_g K_g\right)_e \frac{\Delta y \Delta t}{\Delta x} \quad \text{(A.87)}$$

$$a_S = \frac{1}{2}\left(\varepsilon_g K_g\right)_s \frac{\Delta x \Delta t}{\Delta y} \quad \text{(A.88)}$$

$$b = \frac{1}{4}\left(\varepsilon_g^o \rho_g^o Cp_g^o T_g^o\right)_P \Delta x \Delta y + \frac{1}{4} h_{gsl} S_v \Delta x \Delta y \Delta t \left(T_{sl}\right)_P + \frac{1}{2}\left(\rho_g u_g Cp_g\right)_P T_{g,in} \Delta y \Delta t \quad \text{(A.89)}$$

3.) Discretization of solid and liquid energy equation

$$\frac{\partial}{\partial t}\left(\left(1-\varepsilon_g\right)\rho_{sl}Cp_{sl}T_{sl}\right)+\frac{\partial}{\partial y}\left(\left(1-\varepsilon_g\right)\rho_{sl}u_{sl}Cp_{sl}T_{sl}\right)=$$
$$\frac{\partial}{\partial x}\left(\left(1-\varepsilon_g\right)K_{sl,eff}\frac{\partial T_{sl}}{\partial x}\right)+\frac{\partial}{\partial y}\left(\left(1-\varepsilon_g\right)K_{sl,eff}\frac{\partial T_{sl}}{\partial y}\right) \qquad (2.4)$$
$$+h_{gsl}S_v\left(T_g-T_{sl}\right)-\dot{m}h_{fg}-\dot{m}Cp_v\left(T_g-T_{sl}\right)$$

$$\int_P^s\int_P^e\int_t^{t+\Delta t}\frac{\partial}{\partial t}\left(\left(1-\varepsilon_g\right)\rho_{sl}Cp_{sl}T_{sl}\right)dtdxdy+\int_t^{t+\Delta t}\int_P^e\int_P^s\frac{\partial}{\partial y}\left(\left(1-\varepsilon_g\right)\rho_{sl}u_{sl}Cp_{sl}T_{sl}\right)dydxdt$$
$$=\int_t^{t+\Delta t}\int_P^s\int_P^e\frac{\partial}{\partial x}\left(\left(1-\varepsilon_g\right)K_{sl,eff}\frac{\partial T_{sl}}{\partial x}\right)dxdydt+\int_t^{t+\Delta t}\int_P^e\int_P^s\frac{\partial}{\partial y}\left(\left(1-\varepsilon_g\right)K_{sl,eff}\frac{\partial T_{sl}}{\partial y}\right)dydxdt$$
$$+\int_t^{t+\Delta t}\int_P^s\int_P^e h_{gsl}S_v\left(T_g-T_{sl}\right)dxdydt-\int_t^{t+\Delta t}\int_P^s\int_P^e\dot{m}h_{fg}\,dxdydt$$
$$-\int_t^{t+\Delta t}\int_P^s\int_P^e\dot{m}Cp_v\left(T_g-T_{sl}\right)dxdydt \qquad (A.90)$$

$$\left(\left(1-\varepsilon_g\right)\rho_{sl}Cp_{sl}T_{sl}-\left(1-\varepsilon_g^o\right)\rho_{sl}^oCp_{sl}^oT_{sl}^o\right)_P\frac{\Delta x}{2}\frac{\Delta y}{2}+\left(\left(1-\varepsilon_g\right)\rho_{sl}u_{sl}Cp_{sl}\right)_P\frac{\Delta x}{2}\Delta t\left(T_{sl}\right)_P$$
$$-\left(\left(1-\varepsilon_g\right)\rho_{sl}u_{sl}Cp_{sl}\right)_P\frac{\Delta x}{2}\Delta t\left(T_{sl}\right)_{in}=\left(\left(1-\varepsilon_g\right)K_{sl,eff}\right)_e\frac{\Delta y\Delta t}{2\Delta x}\left(\left(T_{sl}\right)_E-\left(T_{sl}\right)_P\right)$$
$$+\left(\left(1-\varepsilon_g\right)K_{sl,eff}\right)_s\frac{\Delta x\Delta t}{2\Delta y}\left(\left(T_{sl}\right)_S-\left(T_{sl}\right)_P\right)+h_{gsl}S_v\left(\left(T_g\right)_P-\left(T_{sl}\right)_P\right)\frac{\Delta x}{2}\frac{\Delta y}{2}\Delta t \qquad (A.91)$$
$$-\dot{m}h_{fg}\frac{\Delta x}{2}\frac{\Delta y}{2}\Delta t-\dot{m}Cp_v\left(\left(T_g\right)_P-\left(T_{sl}\right)_P\right)\frac{\Delta x}{2}\frac{\Delta y}{2}\Delta t$$

After rearrangement, the discretized solid and liquid energy equation becomes:

$$a_P\left(T_{sl}\right)_P=a_E\left(T_{sl}\right)_E+a_S\left(T_{sl}\right)_S+b \qquad (A.92)$$

Where,

$$a_P = \frac{1}{4}\left(\left(1-\varepsilon_g\right)\rho_{sl}Cp_{sl}\right)_P \Delta x\Delta y + \frac{1}{2}\left(\left(1-\varepsilon_g\right)\rho_{sl}u_{sl}Cp_{sl}\right)_P \Delta x\Delta t + \frac{1}{2}\left(\left(1-\varepsilon_g\right)K_{sl,eff}\right)_e \frac{\Delta y\Delta t}{\Delta x}$$
$$+ \left(\left(1-\varepsilon_g\right)K_{sl,eff}\right)_s \frac{\Delta x\Delta t}{2\Delta y} + \frac{1}{4}(h_{gsl}S_v - \dot{m}Cp_v)\Delta x\Delta y\Delta t \qquad \text{(A.93)}$$

$$a_E = \left(\left(1-\varepsilon_g\right)K_{sl,eff}\right)_e \frac{\Delta y\Delta t}{2\Delta x} \qquad \text{(A.94)}$$

$$a_S = \left(\left(1-\varepsilon_g\right)K_{sl,eff}\right)_s \frac{\Delta x\Delta t}{2\Delta y} \qquad \text{(A.95)}$$

$$b = \frac{1}{4}\left(\left(1-\varepsilon_g^o\right)\rho_{sl}^o Cp_{sl}^o T_{sl}^o\right)_P \Delta x\Delta y + \frac{1}{4}(h_{gsl}S_v - \dot{m}Cp_v)\left(T_g\right)_P \Delta x\Delta y\Delta t$$
$$- \frac{1}{4}\dot{m}h_{fg}\Delta x\Delta y\Delta t + \left(\left(1-\varepsilon_g\right)\rho_{sl}u_{sl}Cp_{sl}\right)_P \frac{\Delta x}{2}\Delta t\left(T_{sl}\right)_{in} \qquad \text{(A.96)}$$

4.) Discretization of water vapour transfer equation

$$\frac{\partial\left(\varepsilon_g\rho_v\right)}{\partial t} + \frac{\partial}{\partial x}\left(\rho_v u_g\right) = \frac{\partial}{\partial x}\left(D_{v,eff}\frac{\partial\rho_v}{\partial x}\right) + \frac{\partial}{\partial y}\left(D_{v,eff}\frac{\partial\rho_v}{\partial y}\right) + \dot{m} \qquad \text{(2.5)}$$

$$\int_P^s \int_P^e \int_t^{t+\Delta t} \frac{\partial \left(\varepsilon_g \rho_v\right)}{\partial t} dt dx dy \quad + \int_t^{t+\Delta t} \int_P^s \int_P^e \frac{\partial}{\partial x}\left(\rho_v u_g\right) dx dy dt$$
$$= \int_t^{t+\Delta t} \int_P^s \int_P^e \frac{\partial}{\partial x}\left(D_{v,eff} \ \frac{\partial \rho_v}{\partial x}\right) dx dy dt \quad + \int_t^{t+\Delta t} \int_P^e \int_P^s \frac{\partial}{\partial y}\left(D_{v,eff} \ \frac{\partial \rho_v}{\partial y}\right) dy dx dt$$
$$+ \int_t^{t+\Delta t} \int_P^s \int_P^e \dot{m} \, dx dy dt \tag{A.97}$$

$$\begin{aligned}&\left(\varepsilon_g \rho_v - \varepsilon_g^o \rho_v^o\right)_P \frac{\Delta x}{2}\frac{\Delta y}{2} + \left(\left(u_g \rho_v\right)_P - u_g \rho_{v,in}\right)\frac{\Delta y}{2}\Delta t \\ &= \left(D_{v,eff}\right)_e \frac{\Delta y \Delta t}{2\Delta x}\left(\left(\rho_v\right)_E - \left(\rho_v\right)_P\right) + \left(D_{v,eff}\right)_s \frac{\Delta x \Delta t}{2\Delta y}\left(\left(\rho_v\right)_S - \left(\rho_v\right)_P\right) + \dot{m}\frac{\Delta x}{2}\frac{\Delta y}{2}\Delta t\end{aligned} \tag{A.98}$$

After rearrangement, the discretized water vapour transfer equation becomes:

$$a_P \left(\rho_v\right)_P = a_E \left(\rho_v\right)_E + a_S \left(\rho_v\right)_S + b \tag{A.99}$$

Where,

$$a_P = \frac{1}{4}\left(\varepsilon_g\right)_P \Delta x \Delta y + \frac{1}{2}\left(u_g\right)_P \Delta y \Delta t + \left(D_{v,eff}\right)_e \frac{\Delta y \Delta t}{2\Delta x} + \left(D_{v,eff}\right)_s \frac{\Delta x \Delta t}{2\Delta y} \tag{A.100}$$

$$a_E = \left(D_{v,eff}\right)_e \frac{\Delta y \Delta t}{2\Delta x} \tag{A.101}$$

$$a_S = \left(D_{v,eff}\right)_s \frac{\Delta x \Delta t}{2\Delta y} \tag{A.102}$$

$$b = \frac{1}{4}\left(\varepsilon_g^o \rho_v^o\right)_P \Delta x \Delta y + \frac{1}{4}\dot{m} \Delta x \Delta y \Delta t + \frac{1}{2} u_g \rho_{v,in} \Delta y \Delta t \tag{A.103}$$